

AFRL-VS-HA-TR-98-0086

Validation of Ionospheric Models

**Dwight T. Decker
Patricia H. Doherty**

**Boston College
Institute for Scientific Research
Chestnut Hill, MA 02467**

30 April 1997

Scientific Report No. 1

APPROVED FOR PUBLIC RELEASE; DISTRIBUTION IS UNLIMITED.



**AIR FORCE RESEARCH LABORATORY
Space Vehicles Directorate
29 Randolph Rd
AIR FORCE MATERIEL COMMAND
Hanscom AFB, MA 01731-3010**

20030902 060

This technical report has been reviewed and is approved for publication.



Contract Manager



Branch Chief

* (This report has been reviewed by the ESC Public Affairs Office (ESC/PAM) and is releasable to the National Technical Information Service (NTIS).)

Qualified requestors may obtain additional copies from the Defense Technical Information Center (DTIC). * (All others should apply to the NTIS.)

If your address has changed, or if you wish to be removed from the mailing list, or if the addressee is no longer employed by you, please notify AFRL/VSIM, 29 Randolph Road, Hanscom AFB, MA 01731-3010. This will help us to maintain a current mailing list.

DO NOT RETURN COPIES OF THIS REPORT unless contractual obligations or notices on a specific document require that it be returned.

REPORT DOCUMENTATION PAGE

Form Approved
OMB No. 0704-0188

Public reporting burden for this collection of information is estimated to average 1 hour per response, including the time for reviewing instructions, searching existing data sources, gathering and maintaining the data needed, and completing and reviewing the collection of information. Send comments regarding this burden estimate or any other aspect of this collection of information, including suggestions for reducing this burden, to Washington Headquarters Services, Directorate for Information Operations and Reports, 1215 Jefferson Davis Highway, Suite 1204, Arlington, VA 22202-4302, and to the Office of Management and Budget, Paperwork Reduction Project (0704-0188), Washington, DC 20503.

1. AGENCY USE ONLY (Leave blank)			2. REPORT DATE 30 April 1997		3. REPORT TYPE AND DATES COVERED Scientific Report No. 1	
4. TITLE AND SUBTITLE VALIDATION OF IONOSPHERIC MODELS			5. FUNDING NUMBERS Contract: F19628-96-C-0039 PE 61102F PR 1010 TA IM WU AC			
6. AUTHOR(S) Dwight T. Decker Patricia H. Doherty			8. PERFORMING ORGANIZATION REPORT NUMBER			
7. PERFORMING ORGANIZATION NAME(S) AND ADDRESS(ES) Boston College Institute for Scientific Research 140 Commonwealth Avenue Chestnut Hill, MA 02167-3862			10. SPONSORING / MONITORING AGENCY REPORT NUMBER AFRL-VS-HA-TR-98-0086			
9. SPONSORING / MONITORING AGENCY NAME(S) AND ADDRESS(ES) Air Force Research Laboratory 29 Randolph Road Hanscom AFB, MA 01731-3010 Contract Manager: John Retterer/VSBP			11. SUPPLEMENTARY NOTES			
12a. DISTRIBUTION / AVAILABILITY STATEMENT Approved for public release; distribution unlimited			12b. DISTRIBUTION CODE			
13. ABSTRACT (Maximum 200 words) <p>In the last year, we have studied several issues involving the validation of ionospheric models and the use of observational databases. Modeling work has included a mid-latitude intercomparison of five first principal physical models for the earth's ionosphere. Work at low latitudes has involved using the Parameterized Ionospheric Model (PIM) to improve the International Reference Ionosphere (IRI90) low latitude ionospheric specification. At high latitudes, the work has involved attempts to produce blobs at the times and locations of actual observations. The usefulness of GPS occultations have been studied using a series of simulations of such occultations and examining inversions of the simulations. Other studies have been made on various aspects of using GPS measurements for ionospheric research. These include the solar cycle dependence of the Total Electron Content (TEC), the effects of anti-spoofing, the TEC of the protonosphere, the effects of instrumental bias, and spatial and temporal variations in the TEC.</p>						
14. SUBJECT TERMS Ionospheric weather, Global F-region modeling, Total electron content (TEC), GPS, GPS/MET, Occultations, Plasma structure, Blobs					15. NUMBER OF PAGES	
					16. PRICE CODE	
17. SECURITY CLASSIFICATION OF REPORT UNCLASSIFIED		18. SECURITY CLASSIFICATION OF THIS PAGE UNCLASSIFIED		19. SECURITY CLASSIFICATION OF ABSTRACT UNCLASSIFIED		
				20. LIMITATION OF ABSTRACT SAR		

TABLE OF CONTENTS

	Page
1. INTRODUCTION	1
2. MODELING STUDIES	1
2.1 PRIMO	1
2.2 Boundary and Subauroral Blobs	2
2.3 Simulations of GPS/MET Ionospheric Observations	2
2.4 Improving IRI90 Low-Latitude Ionospheric Specification	19
2.5 Ionospheric Modeling Using Systems of Plasma Kinetic Equations	37
3. OBSERVATIONAL DATABASES	38
3.1 Solar Cycle Dependence of Absolute Ionospheric Total Electron Content	38
3.2 Absolute Real-Time Ionospheric Measurements from GPS Satellites in the Presence of Anti-Spoofing	39
3.3 Total Electron Content of the Earth's Protonosphere	39
3.4 Instrumental Bias in GPS Measurements	41
3.5 Statistics of the Spatial and Temporal Variations in Ionospheric Range Delay	48
3.6 Airglow Data	49
3.7 Signature of Equatorial Scintillation Onset in Near-Sunset DMSP Satellite Data	49
4. REFERENCES	51
5. PRESENTATIONS AND PROCEEDINGS	54
6. JOURNAL ARTICLES	64
Modeling the Formation of Polar Cap Patches Using Large Plasma Flows	65

Collisional Degradation of the Proton-H Atom Fluxes in the Atmosphere: A Comparison of Theoretical Techniques	86
Total Electron Content Over the Pan-American Longitudes: March-April 1994	100

1. INTRODUCTION

The objective of this research is to obtain various ionospheric measurements from a wide range of geographic locations and to utilize the resulting databases to validate the theoretical ionospheric models that are the basis of the Parameterized Real-time Ionospheric Specification Model (PRISM) and the Ionospheric Forecast Model (IFM). Thus our various efforts can be generally categorized as either modeling studies or work concerning observational databases.

2. MODELING STUDIES

2.1. PARAMETERIZED REAL-TIME IONOSPHERIC MODELS AND OBSERVATIONS WORKSHOP (PRIMO)

Over the last several years, we have participated in the PRIMO workshop at the annual CEDAR meeting. This PRIMO working group has focused on the intercomparison of five first principles physical ionospheric models and a manuscript has been written describing the results. While overall the various models compared well, there were some remaining differences that were disturbing. In particular, there were differences between the Global Theoretical Ionospheric Model (GTIM) and the Field Line Interhemispheric Plasma (FLIP) model that appeared inconsistent.

As a result, we repeated the four runs that were originally done for the PRIMO paper. For all four runs, we used the HWM90 wind model rather than the HWM87 model to be consistent with what was used by FLIP and Time Dependent Ionospheric Model (TDIM). We further discovered that the original two solar maximum runs had not been done for precisely the same days as stated in the paper. This had little effect on the December case; however, for the June case, it made a difference in the magnetic conditions that led to changes as significant as those caused by changing wind models. We also decided to reduce our nocturnal source of ionization to its "physical value". In previous runs, we had used an enhanced nocturnal source to ensure that the nighttime densities during winter solstice were maintained at a realistic level. However, for the purposes of model comparisons this simply confused the issue and obscured under what conditions GTIM has problems maintaining the nighttime ionosphere.

These various changes have produced a more consistent comparison between GTIM and FLIP. For the winter cases, GTIM's n_{mf_2} goes from being a bit below FLIP at night to a bit above in the daytime; while GTIM's h_{mf_2} is generally 10 -15 km above FLIP. The summer cases have GTIM h_{mf_2} going from around 5 km below FLIP at night to 5-10 km above during the daytime. GTIM's n_{mf_2} generally runs a bit above FLIP for the summer runs.

We also performed some runs with the neutral wind reduced by 50 percent as was done in the TDIM runs. This improved some of the comparisons between GTIM and TDIM; however, in some cases it made the comparisons worse. Discussions with Jan Sjoka indicated that they also noted something odd about some of the TDIM runs. Accordingly, we have planned no more efforts on this issue until they understand the details of what is going on with these particular TDIM runs.

2.2. Boundary and Subauroral Blobs

In previous work, we have shown that GTIM can simulate F-region electron density enhancements known as boundary blobs. In that work we did not compare to any particular data, rather we produced structures that simply had many of the features associated with boundary blobs. The next step was to modify the simulation to see if blobs could be produced at the times that they have been observed. It was not obvious that this could be done because our first simulations would not produce blobs at the time appropriate for viewing by the Chatanika radar. We chose to simulate the conditions of an experiment carried out on 29 January 1979 during which the Chatanika radar observed blobs for over six hours in the evening sector. Our previous simulation was modified in two ways. First, our variation of the convection pattern was shifted in UT so as to have the potential of producing blobs at the appropriate time. Second we shifted from December solstice to 29 January. Both of these changes were crucial. The shift away from solstice was crucial for allowing high density plasma to be transported from the daytime across the polar cap into the auroral regions at the appropriate time. The shift in time of when the convection pattern was varied ensured that this plasma was directed at the appropriate time into the evening sector. The resultant blobs appeared at the appropriate time and were comparable in magnitude to what was actually seen in the experiment. The next step will be to change the size of the convection pattern to see if we can produce the blobs both at the correct time and correct latitude.

2.3. Simulations of GPS/MET Ionospheric Observations

GPS/MET is a program using a low-earth-orbiting (LEO) satellite instrumented with a GPS receiver to perform limb soundings of the atmosphere using radio occultation of GPS satellites. The primary purpose of the program is to perform remote sensing of the troposphere and stratosphere. However, the limb-viewing geometry does provide a unique opportunity for ionospheric research. The useful measured quantity in this case is the Total Electron Content (TEC) between the low-earth-orbiting satellite and a particular GPS satellite. In contrast to ground-based GPS measurements, the limb viewing geometry can provide the type of vertical information that is poorly measured by ground-based GPS measurements.

The issue of interest is that of how well we can invert such measurements of integrated electron density into the electron density itself as a function of 1, 2, or 3 dimensions. Previous workers have shown that for the case of two dimensions a single occultation does not uniquely define the electron density. Rather, one has to deal with an underdetermined system of equations. One approach to this problem has been to apply a two dimensional tomographic formalism to inverting a single occultation to produce a single electron density profile (EDP) by assuming a particular horizontal ionospheric behavior. This idea has been applied to cases assuming spherical symmetry and cases with a horizontal gradient that is the same at all altitudes [Hajj *et al.*, 1994].

We are working on assessing how useful such an approach can be. Our first goal is to quantify how well an inversion can work under various ionospheric conditions when we assume spherical symmetry. We have begun by writing an implementation of the Abel inversion. In Figure 1, we show the geometry of an ideal occultation. A low-earth-orbiting satellite receives a GPS signal which can be occulted by the earth. The occultation is assumed to occur in a plane and the

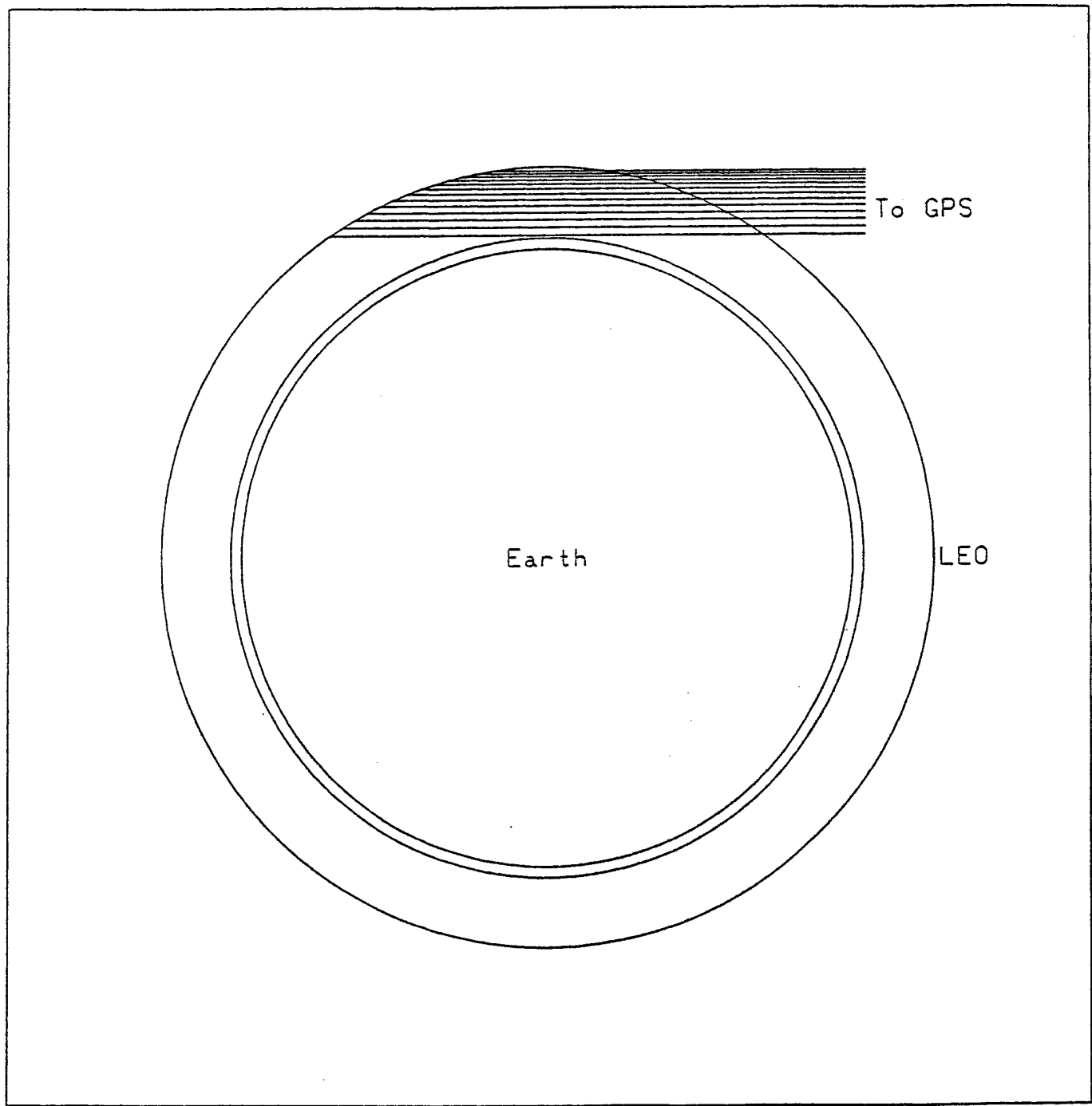


FIGURE 1. GPSMET Ionospheric Occultation

motion of the GPS satellite is neglected. By subtracting the signals taken along the same ray path, the TEC below the altitude of the LEO satellite can be determined. In order to test the usefulness of the Abel inversion, we have used an ionospheric model to simulate the TEC that would be measured in such a geometry, inverted the simulated observation, and then compared to the profile given by the ionospheric model. The model used has been the Parameterized Ionospheric Model (PIM). In Figure 2, we give an example for a solar maximum equinox of a simulated GPS/MET TEC observation using a spherically symmetric ionosphere based on the PIM during magnetically quiet conditions. The center of the occultation region is at 0° geographic latitude and longitude and is for a local time of midnight. Figure 3 shows the profile derived from the Abel inversion (short dashes) and the original profile from the PIM (long dashes). This simply shows how well the inversion can work when you have a spherically symmetric ionosphere.

The next step has been to perform a series of simulations using the full PIM ionosphere, that is, an ionosphere that has not been constructed to be symmetric. In Figure 4, we show a daytime case with the center of the occultation at -40° North and 0° longitude. Again, the short dashes are the Abel inversion and the long dashes are the PIM profile. We see that in the daytime mid-latitudes the Abel can work very well. Plotted on the right is the fractional difference of the two profiles. The .1 and .3 levels are marked by vertical lines about zero. We see that the agreement is better than 10 percent above 200 km. Figure 5 shows the same comparisons except for 10° N latitude. Again, in the F-region, the two profiles agree to within 10 percent. However, the E region shows large differences with the Abel inversion producing negative densities. The case for 40° North is shown in Figure 6, where we see good agreement in the E region but the F region agreement is much poorer. We summarize our daytime results in Figure 7 where we show contours of fractional differences versus altitude and latitude. In general, the F regions agree to better than 20 percent. The one exception is around 40° North where there is a strong F region gradient in the PIM ionosphere that causes the disagreement. The E region is clearly a problem with the greatest difficulties occurring around the geomagnetic equator (10° North geographic).

Turning to the nighttime, we show in Figure 8 results for 2000 local time at -30° North. We see fair agreement in the F-region (30 percent) and very poor agreement in the E region. Figure 9 gives the 10° North results and shows poor agreement at all altitudes. In Figure 10 we again summarize by showing contours of fractional differences versus latitude and altitude. We see that at night the Abel inversion does a much poorer job than in the daytime.

To this point all the simulated occultations have been done assuming a north-south viewing direction. We have also tried some east-west viewing simulations for the daytime ionosphere. Figures 11-13 show three cases for -60° , 0° , and 20° North respectively. Figure 14 shows contours of fractional differences versus latitude and altitude. We see that in this case the Abel does an excellent job throughout the F region (above 200 km). Future work on this topic will consist of performing these simulations for a variety of geophysical conditions.

The Abel inversion described above is an example of using what is known as continuous inverse theory. The main limitation of the Abel is that it assumes a very particular behavior for the horizontal behavior of the ionosphere. We have developed an alternative approach that uses discrete inverse theory for performing the inversion. In this approach, the integral equation that defines the relationship between electron density and the TEC measurements is converted into a

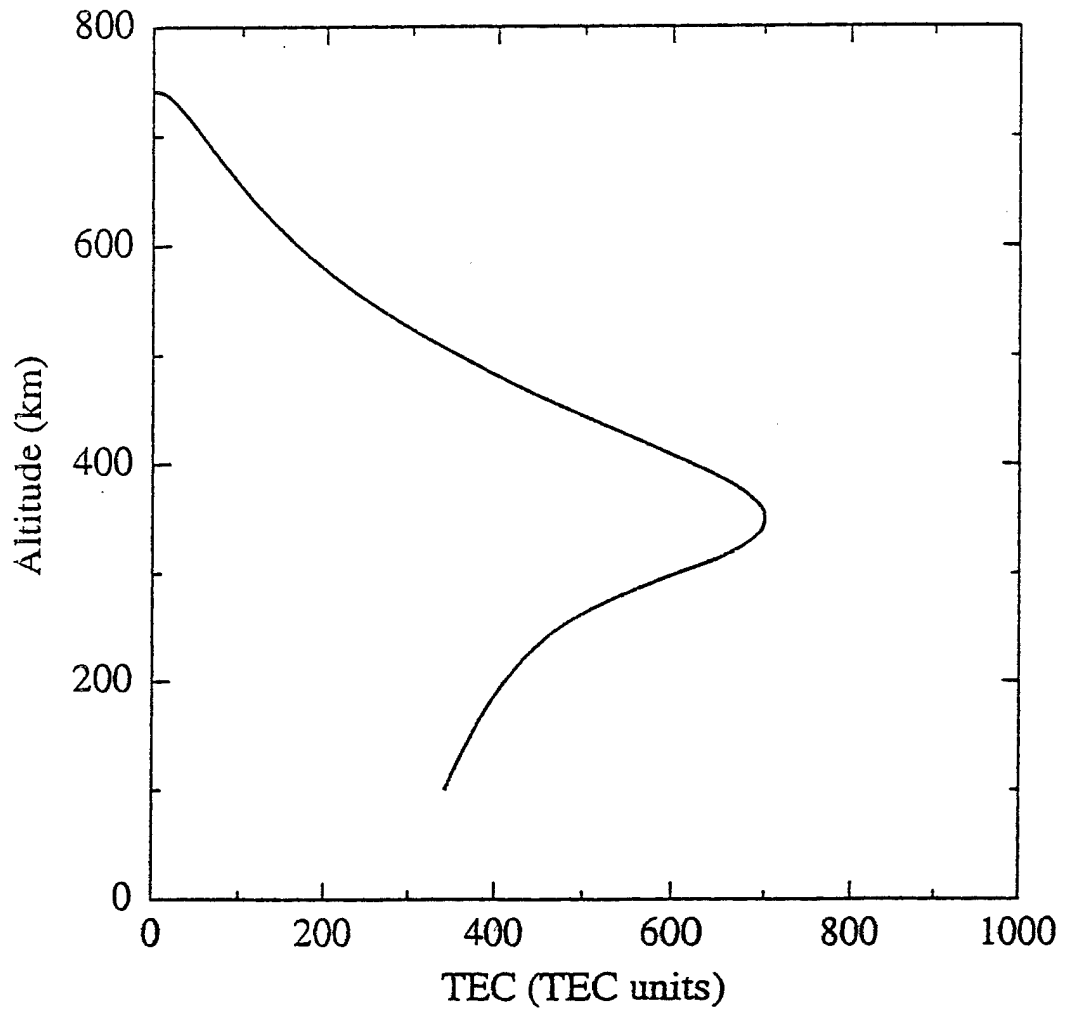


FIGURE 2. GPSMET Simulated TEC Sph. Sym. PIM

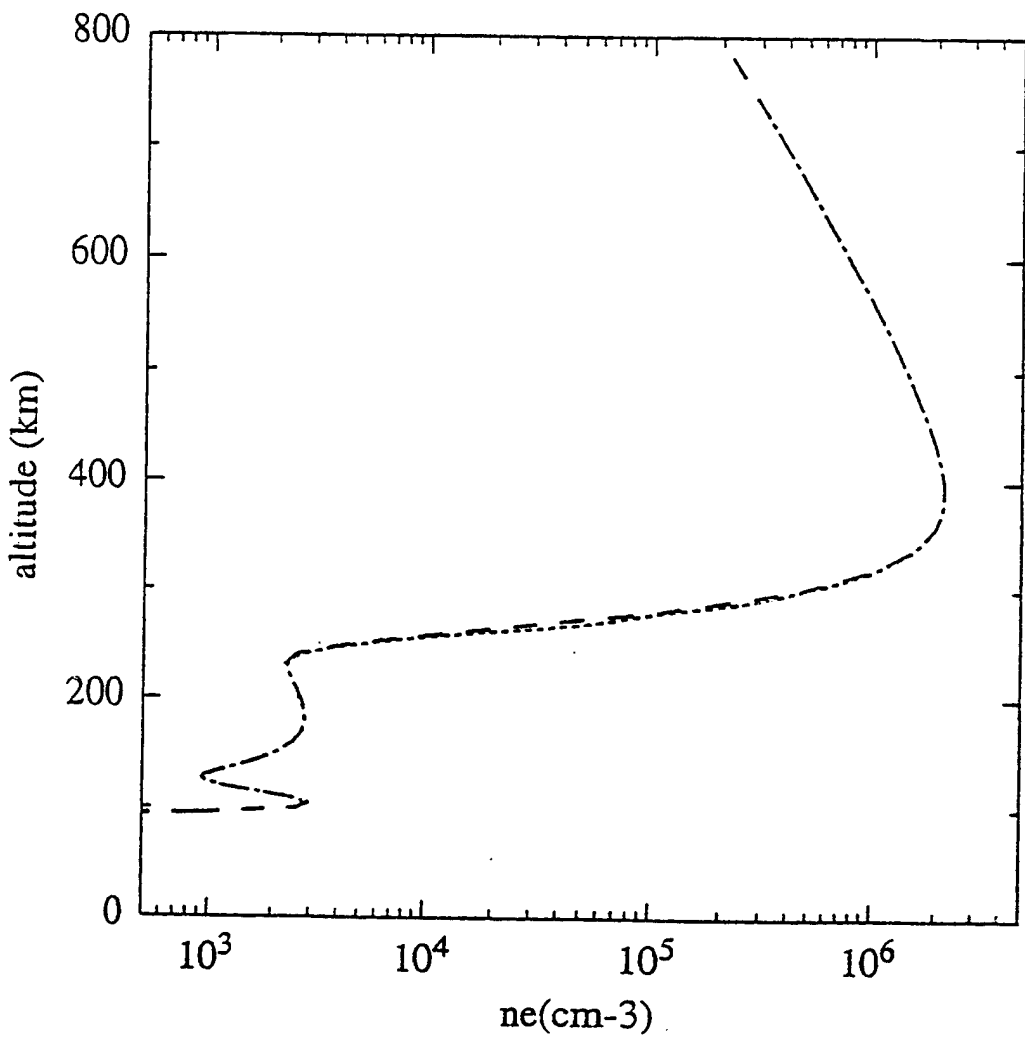
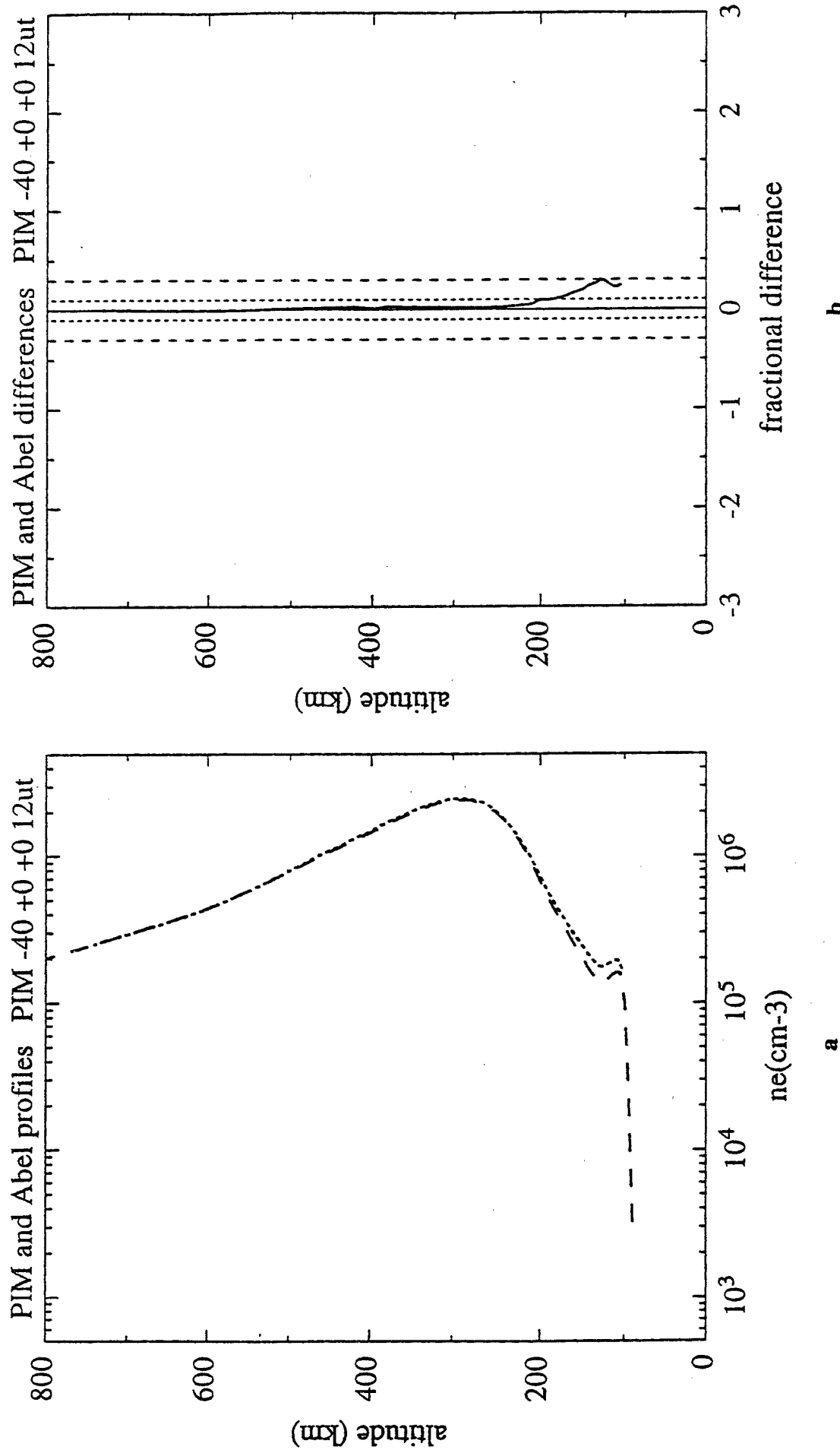
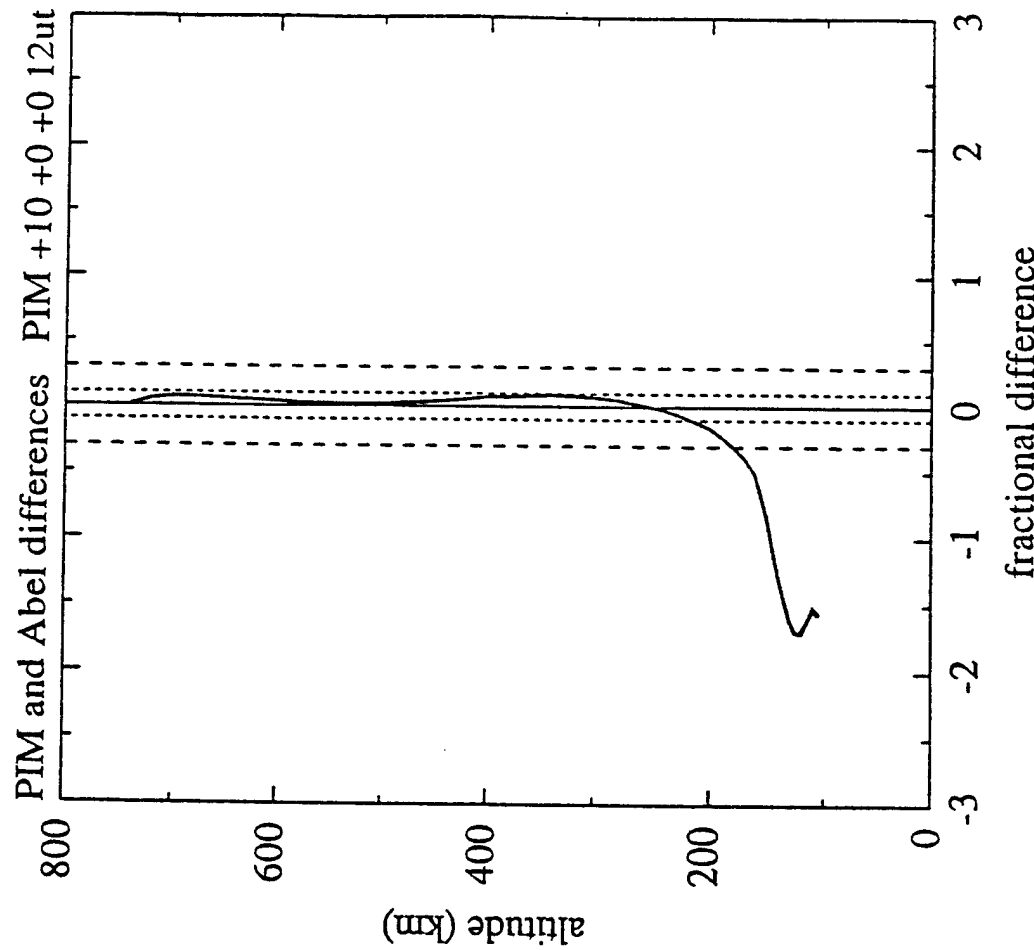
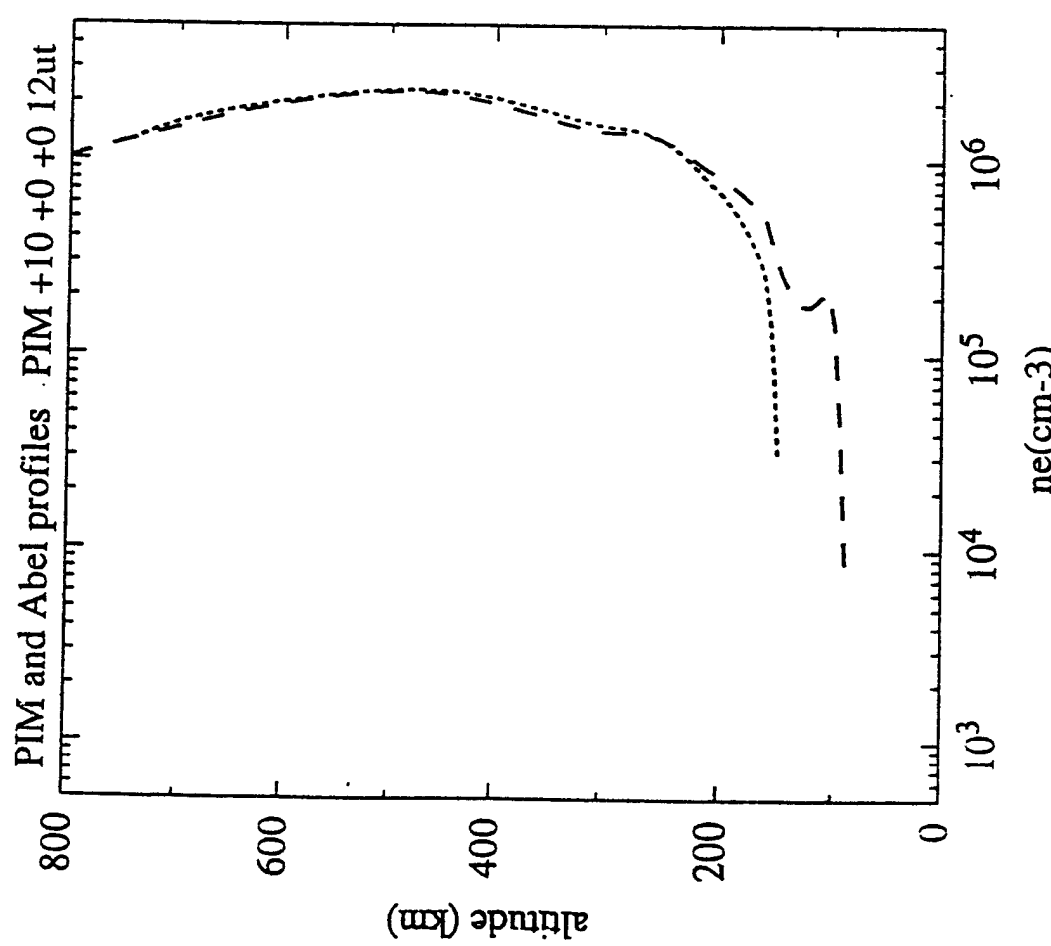


FIGURE 3. PIM and Abel Inverted Profile Sph. Sym. PIM

FIGURE 4. (a) PIM and Abel Profiles PIM -40 +0 +0 12 UT
 (b) PIM and Abel Differences PIM -40 +0 +0 12 UT





a

b

FIGURE 5. (a) PIM and Abel Profiles PIM +10 _0_0 12 UT
 (b) PIM and Abel Differences PIM +10 +0 +0 12 UT

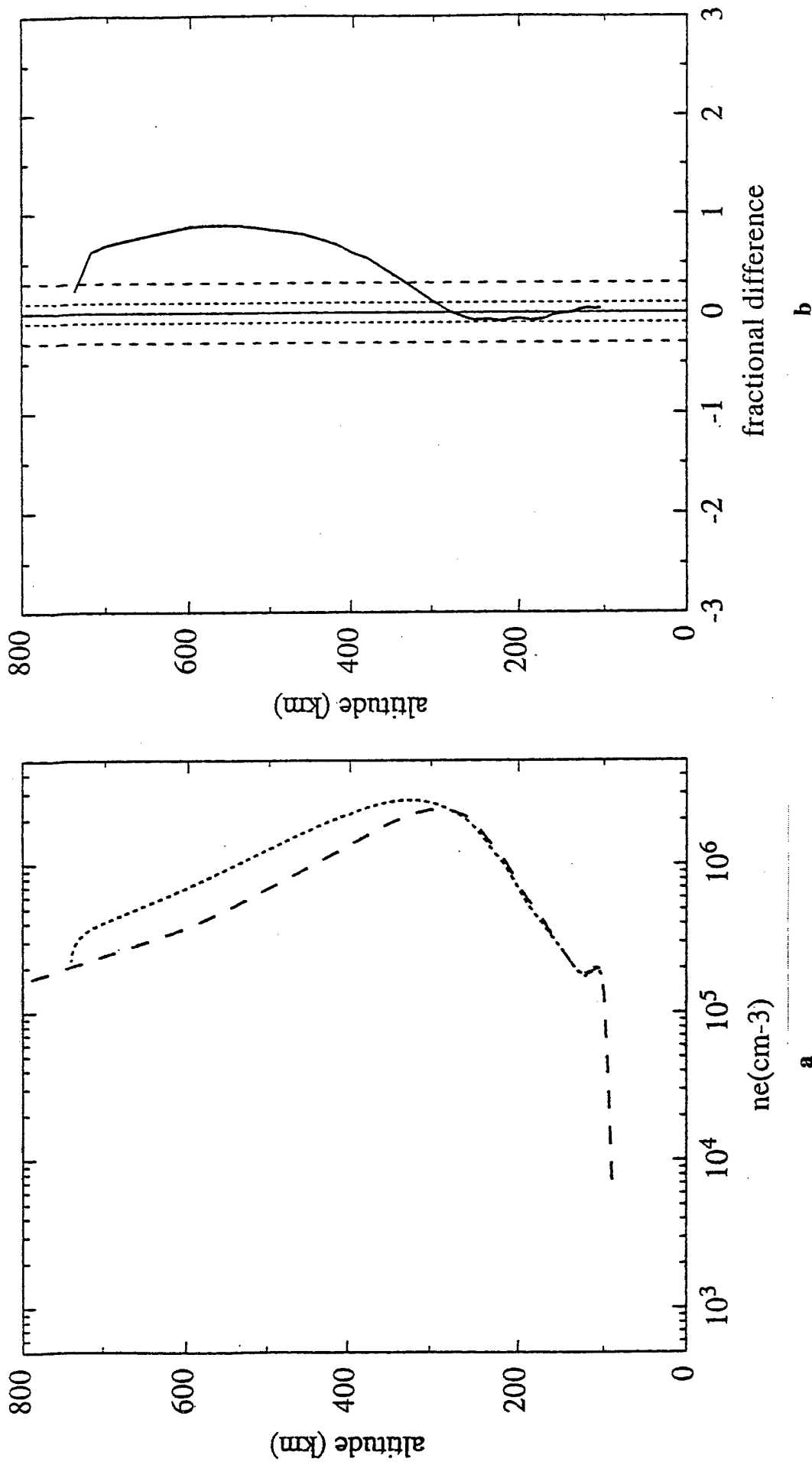


FIGURE 6. (a) PIM and Abel Profiles PIM +40 +0 +0 12 UT
 (b) PIM and Abel Differences PIM +40 +0 +0 12 UT

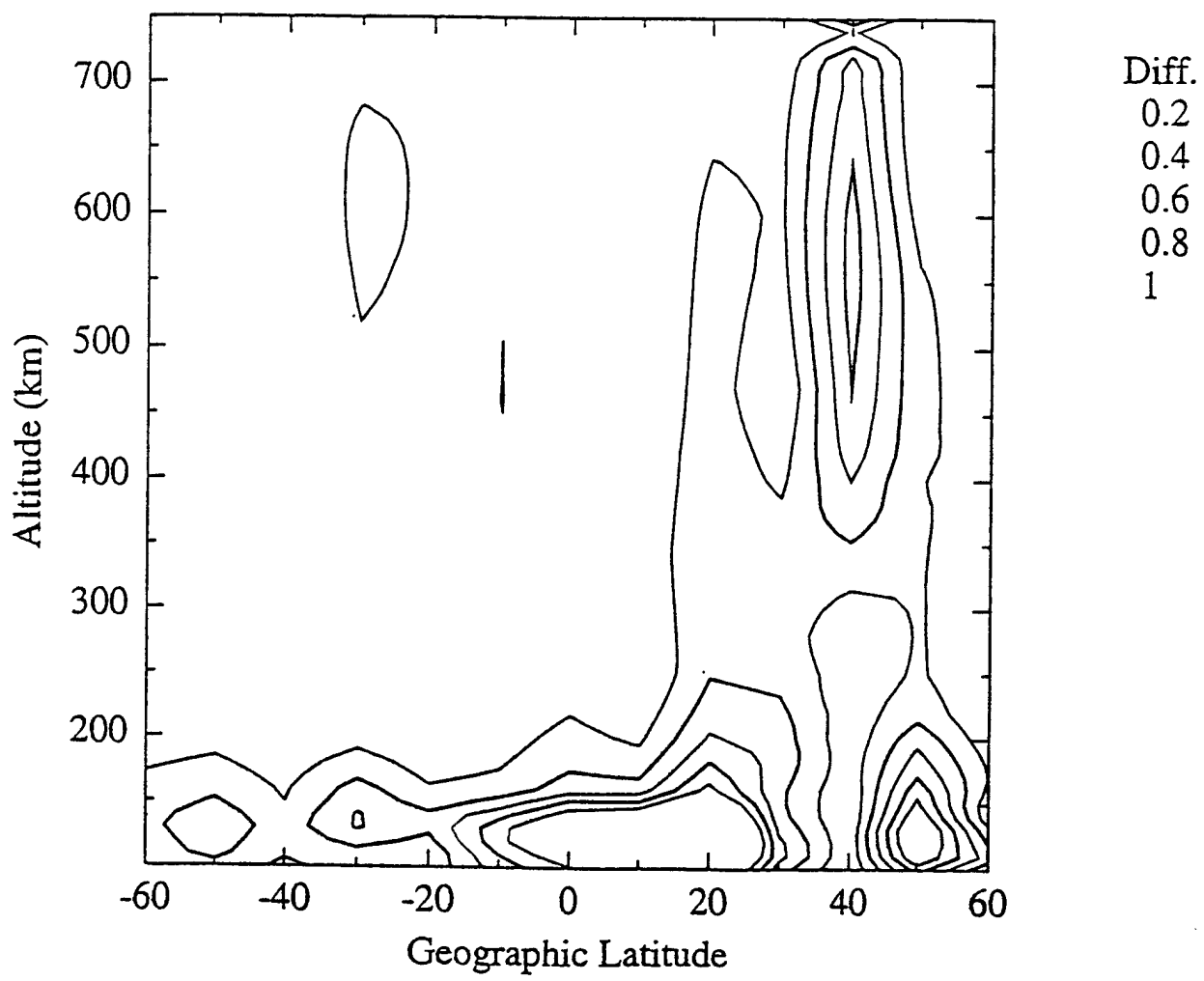


FIGURE 7. Fractional Difference 0 Long 0 Azimuth 12 UT

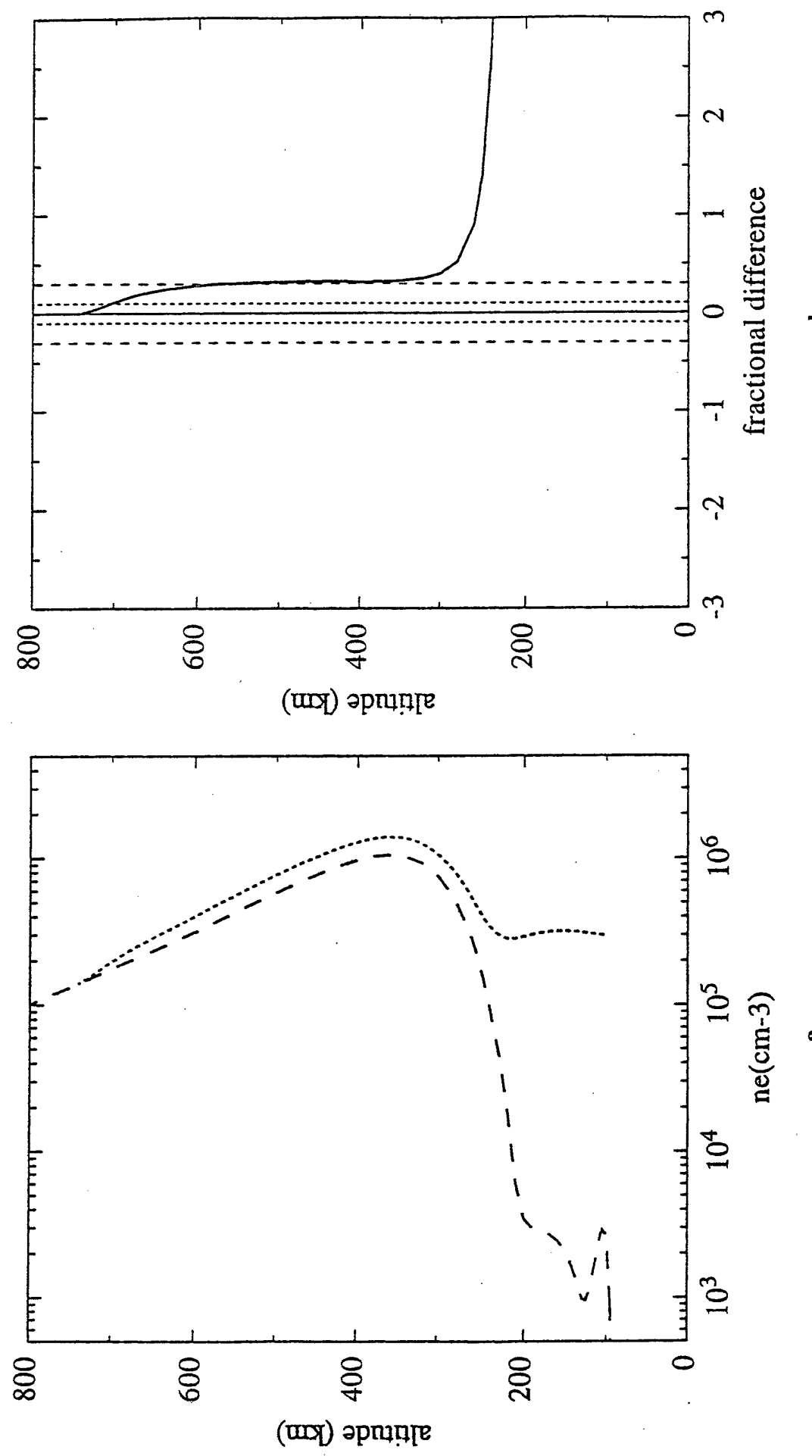
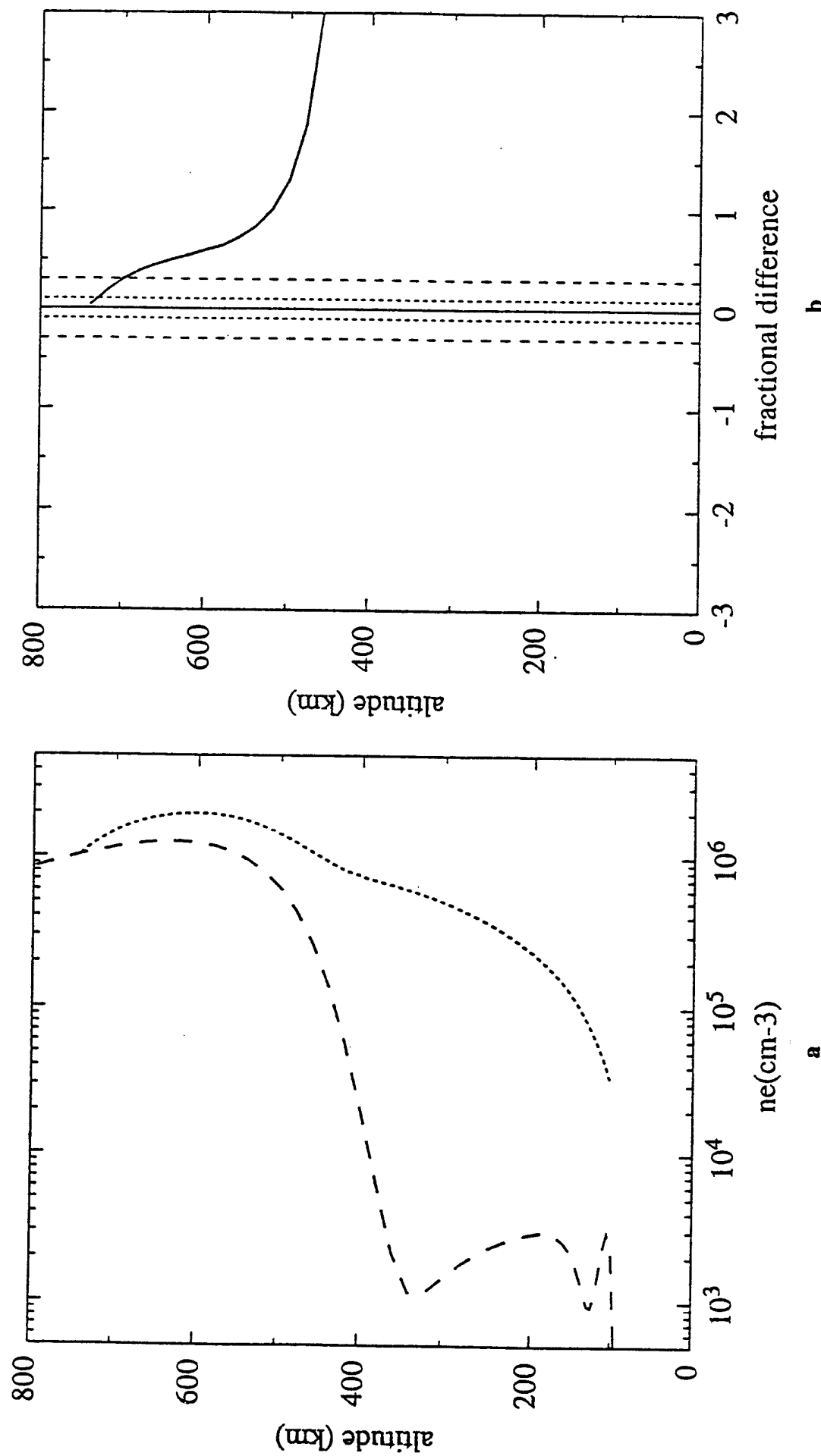


FIGURE 8. (a) PIM and Abel Profiles PIM -30 +0 +0 20 UT
 (b) PIM and Abel Differences PIM -30 +0 +0 20 UT

FIGURE 9. (a) PIM and Abel Profiles PIM +10 +0 +0 20 UT
 (b) PIM and Abel Differences PIM +10 +0 +0 20 UT



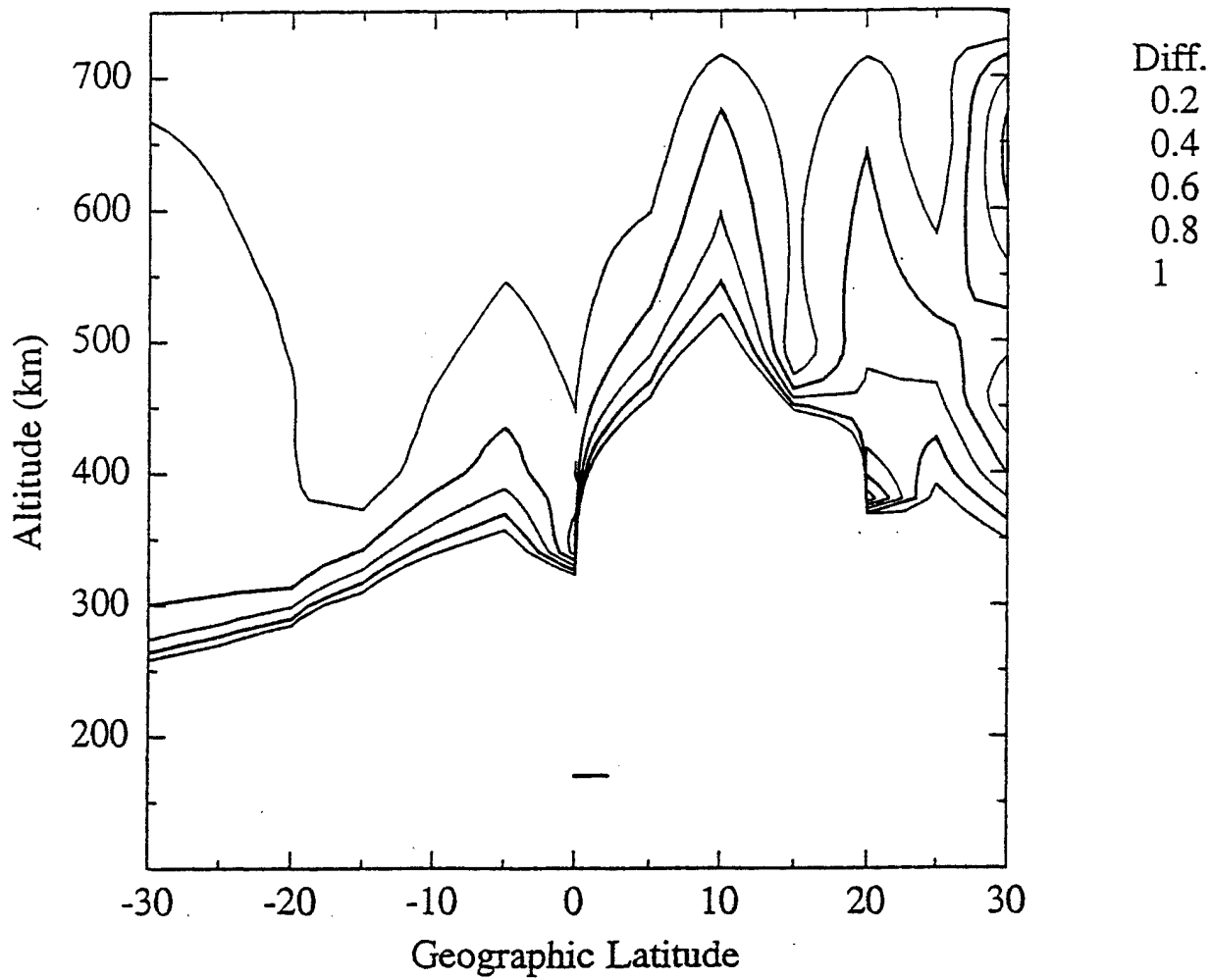
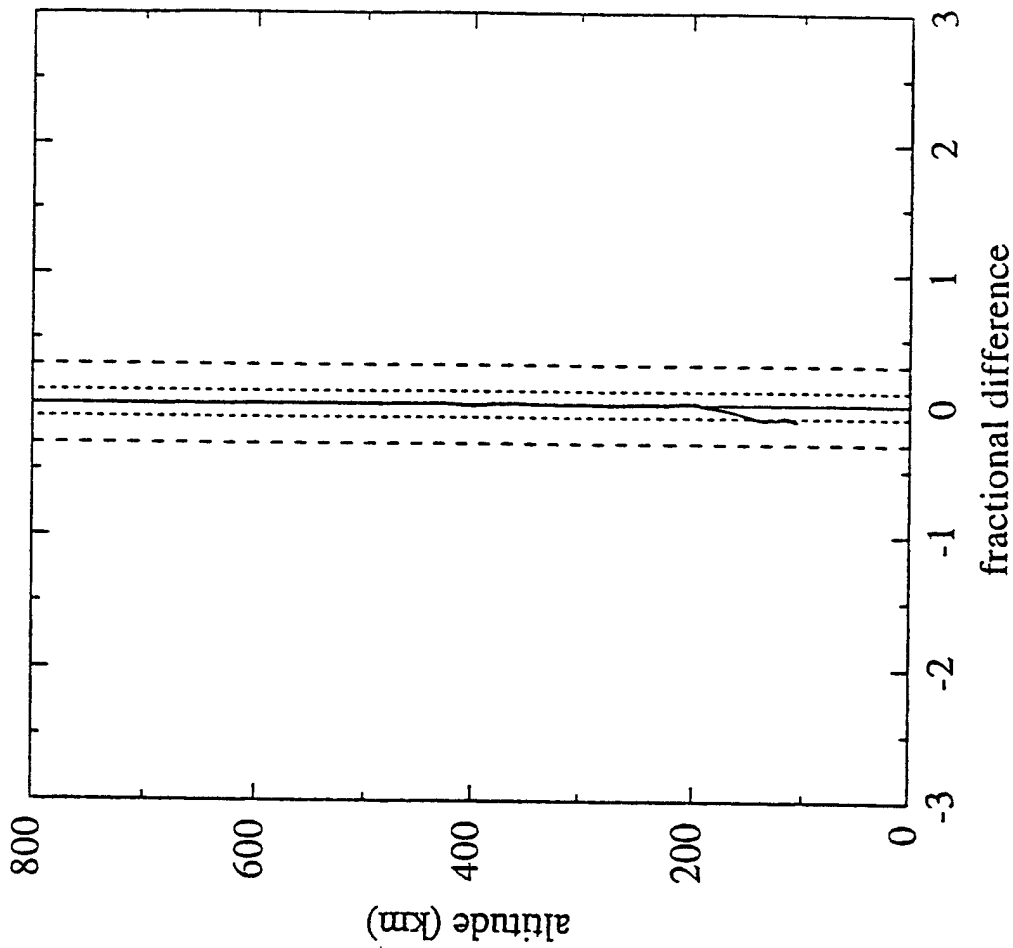


FIGURE 10. Fractional Difference 0 Long 0 Azimuth 20 UT

b



a

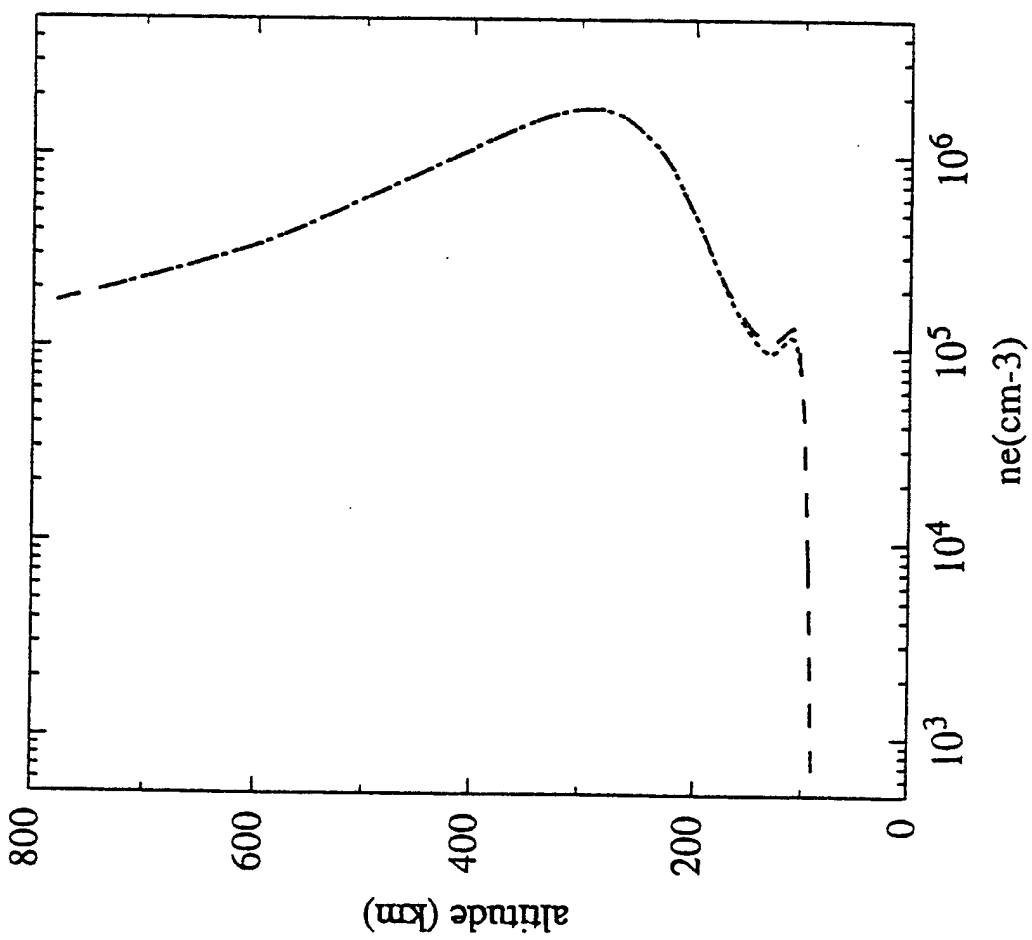


FIGURE 11. (a) PIM and Abel Profiles PIM -60 +0 +90 14 UT
 (b) PIM and Abel Differences PIM -60 +0 +90 14 UT

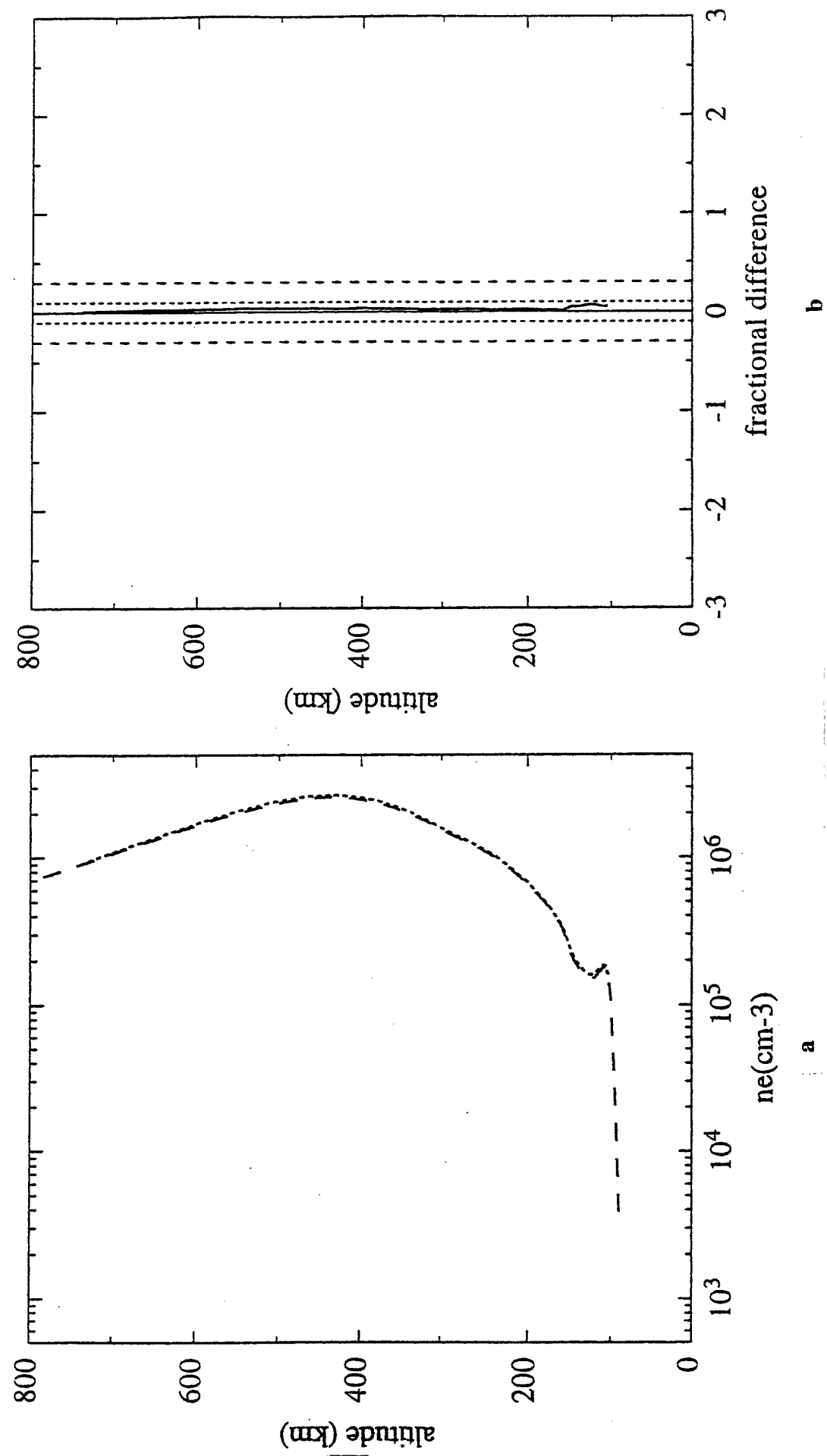


FIGURE 12. (a) PIM and Abel Profiles PIM +0 +0 +90 14 UT
 (b) PIM and Abel Differences PIM +0 +0 +90 14 UT

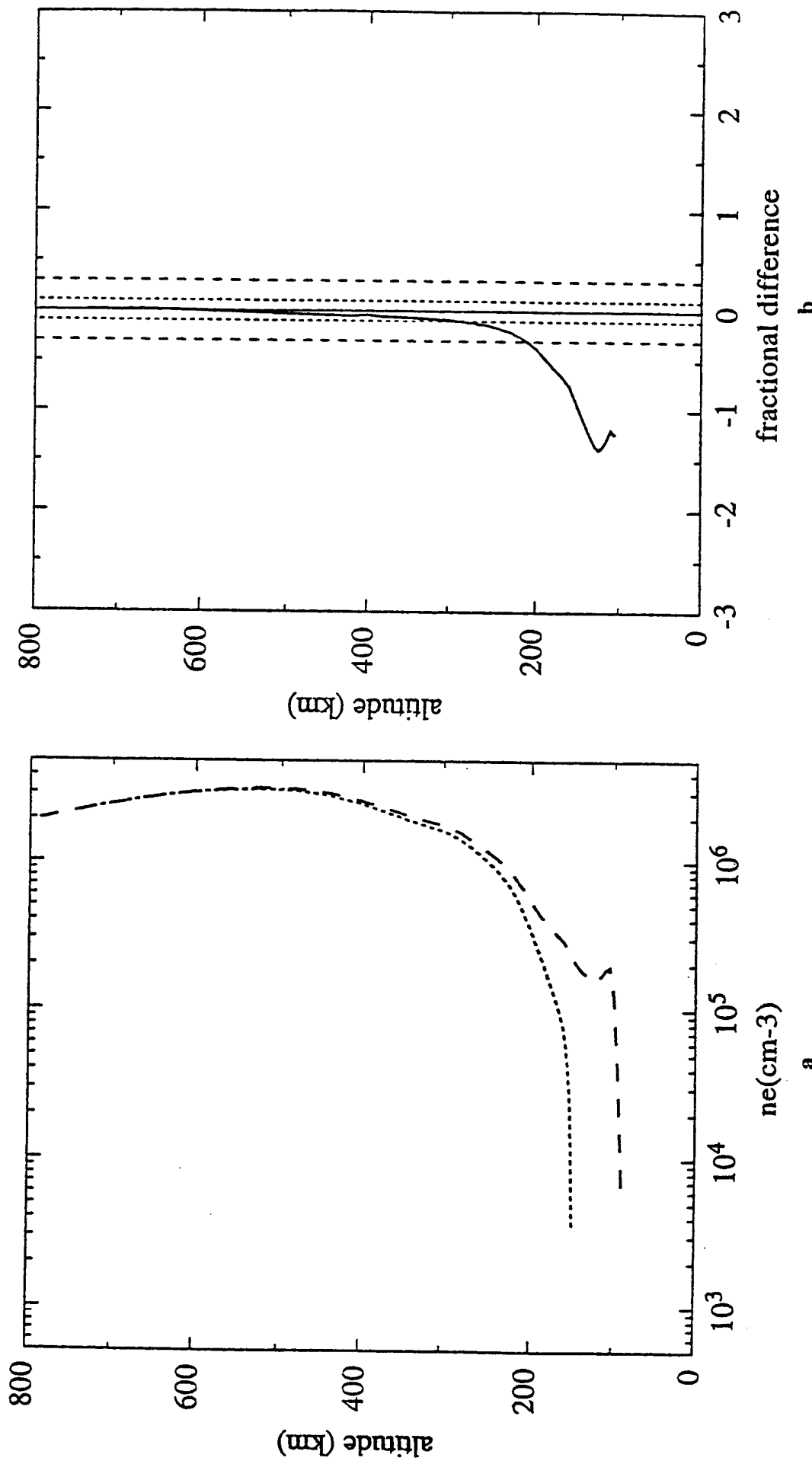


FIGURE 13. (a) PIM and Abel Profiles PIM +20 +0 +90 14 UT
 (b) PIM and Abel Differences PIM +20 +0 +90 14 UT

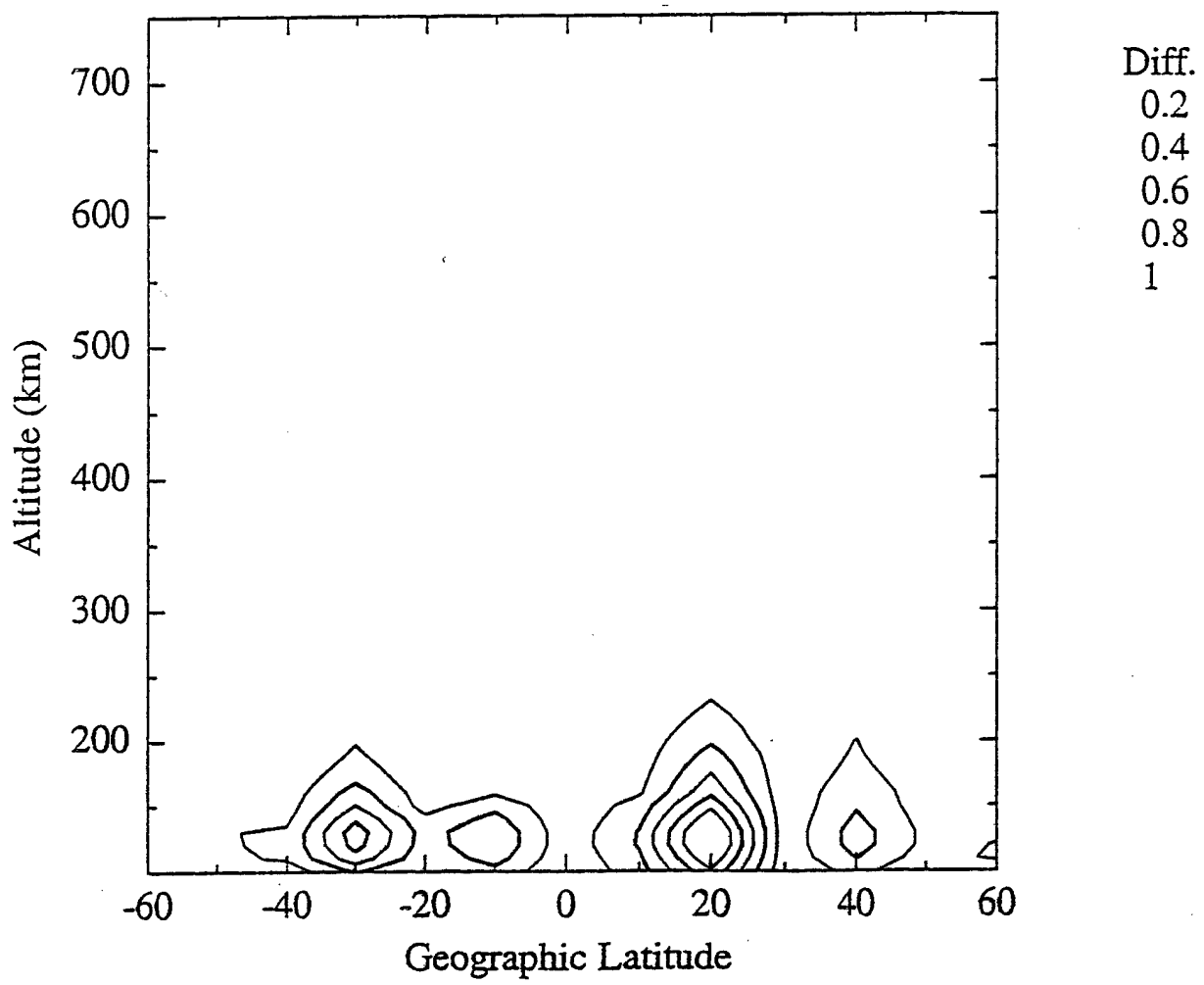


FIGURE 14. Fractional Difference 0 Long 0 Azimuth 14 UT

matrix equation, which is then solved using various techniques of linear algebra [Hajj *et al.*, 1994]. The main advantage of this matrix equation solution (MES) approach is that while we may not know the horizontal behavior of the ionosphere it does give a method that can treat whatever horizontal dependence we may choose. It is also the approach that has the flexibility to handle *a priori* constraints that are used in tomography to reduce the effects of what are often ill-posed problems.

In developing a MES method, some time was spent assessing whether any horizontal information could be inferred from the TEC measurements by accepting a poorer description of the altitude dependence of the EDP. However, the underdetermined nature of the problem produced unstable and incorrect solutions. We did find that the MES method can give similar results to the Abel when it is assumed that the horizontal dependence is a constant. Further, if the actual horizontal dependence of the ionosphere is assumed then the actual EDP at the center of the occultation region can be recovered. Our implementation of the method is not yet as robust as desired because in the case of nighttime profiles, where the E region can be three orders of magnitude smaller than the F_2 peak density, the method has trouble reproducing the E region even when the actual horizontal behavior is provided. We believe this arises from discretization errors and that improvements to the numerics of our algorithm may be able to cure this problem.

We have used the MES approach to explore the possibility of using other measurements to help constrain the inversion process. In Figure 15, we show two examples of using an in-situ electron density measurement to help constrain the inversion. In the left panel, we show a PIM profile (long dashes), an Abel inversion of simulated GPS/MET observations (short dashes), and a MES inversion (dots) that has applied to all altitudes the horizontal dependence of the ionosphere that would be observed by an in-situ satellite measurement. In the right panel, we show the same PIM and Abel profiles but the third profile is a MES inversion using the in-situ observed horizontal dependence down to the Abel determined h_{mf2} and a constant horizontal behavior at lower altitudes. The main effect of having the in-situ measurement was to improve the quality of agreement in the topside of the EDPs.

Work has continued on the Abel transform approach, we have started with to assess the impact of measurement errors on the transform. In Figure 16, we show in the left panel two EDPs and in the right panel the fractional differences between the two profiles. The curve of long dashes in the left panel is a PIM profile from a symmetric ionosphere. The curve of short dashes is the Abel inverted profile when a 3 TEC unit error is added to the simulated GPS/MET observations. We see that the F-region profile that is recovered is fairly insensitive to such errors whereas the small E-region densities are quite sensitive to them. This suggests that the inversion technique may be quite robust for producing good F region and topside measurements but as a technique for nighttime E-region it may be quite problematic.

We have also made our first two attempts at inverting actual GPS/MET observations. We chose two occultations that occurred on Day 298, 1995. The first case involved GPS #16 at around 13:49 UT/10:15 LT and the occultation region was near Sao Paulo, Brazil. In Figure 17, we compare the actual TEC profile (solid curve) and the PIM simulation (dotted curve) for this case. Given that we are comparing a particular day's measurement to the climatology in the PIM, the differences are not unreasonable. In Figure 18, we show in the left panel the Abel inversion of the data (solid curve) and the PIM EDP (dashed curve) for these conditions. In the right panel,

we again show the Abel inversion but compared to a Bent Model EDP. The differences seen between the Abel derived F_2 peak and the PIM or Bent F_2 peaks is not unreasonable considering the day-to-day variability of the $\mathbf{E} \times \mathbf{B}$ vertical drift that is observed at low latitudes. The second case involved GPS #6 at around 21:23 UT/ 22:44 LT and the occultation region was around San Vito, Italy. Figure 19 shows the observed TEC profile (solid curve) and the PIM (dotted curve) simulation for this case. Again the simulated TEC is reasonable compared to the observed. In Figure 20, we show in the left panel the Abel inversion of the data (solid curve) and the PIM EDP (dashed curve). The right panel contrasts the Abel inversion (solid curve) and the Bent Model EDP (dashed curve). The F_2 peaks again are in reasonable agreement; however, the PIM EDP topside is very different from the Abel inferred profile. Our first thought was that this might be an indication of some horizontal structure that is ignored in the Abel inversion. On the other hand, the PIM topside consists only of O^+ and DMSP observations indicate that at this time and location H^+ may very well be the dominant species at around 800 km. The Bent Model on the other hand is an empirical model that should reflect any observable solar minimum H^+ morphology. In the right panel, we see that the Bent profile does show signs of H^+ dominance above 600 km and this suggests that the shape of the Abel inferred profile is reflecting a transition of O^+ to H^+ dominance at around 500 km. This raises the possibility that the GPS/MET database could become an excellent source of data for studying the O^+ to H^+ transition height during solar minimum conditions.

2.4. Improving IRI90 Low-Latitude Ionospheric Specification

In the middle of the year, we submitted a paper to *Radio Science* on this topic. Two referee reports were sent to us and considerable work was done to respond to those reports. We began by performing a more extensive review of the literature led to provide a more extensive discussion of IRI, its successes, and its failures. This review leads to our writing the following extended introduction to the paper.

Introduction

The International Reference Ionosphere (IRI) is a global empirical model that specifies the monthly average of the electron density, electron temperature, ion temperature, and ion composition from 80 km to 1000 km. It has been developed as a joint URSI/COSPAR project and first appeared as tables of profiles presented at the XVII General Assembly of URSI in 1972. However, the general philosophy was to develop a computer model based on critically evaluated observations and so IRI quickly evolved from a set of tables to a computer program (IRI-78) available to the research community. Over the years, testing and modification of IRI has continued with extensive participation by the international research community. The result is that IRI has evolved and improved through several versions (IRI-80, IRI-86, IRI-90, IRI-95) and has become a valuable research tool [Bilitza *et al.*, 1993; Szuszczewicz *et al.*, 1996].

As a data-based model, the IRI is naturally only as good as the available observations. In the case of electron density, the data sources are ionosonde measurements, incoherent scatter measurements, rocket measurements, and a selection of satellite measurements [Bilitza, 1990]. Because the F_2 -peak parameters (peak density and height) are based on ground based ionosonde measurements, which are for the most part located in the mid-latitudes, there is a lack of observations from the low latitude regions, the high latitudes/polar cap and the ocean areas.

b

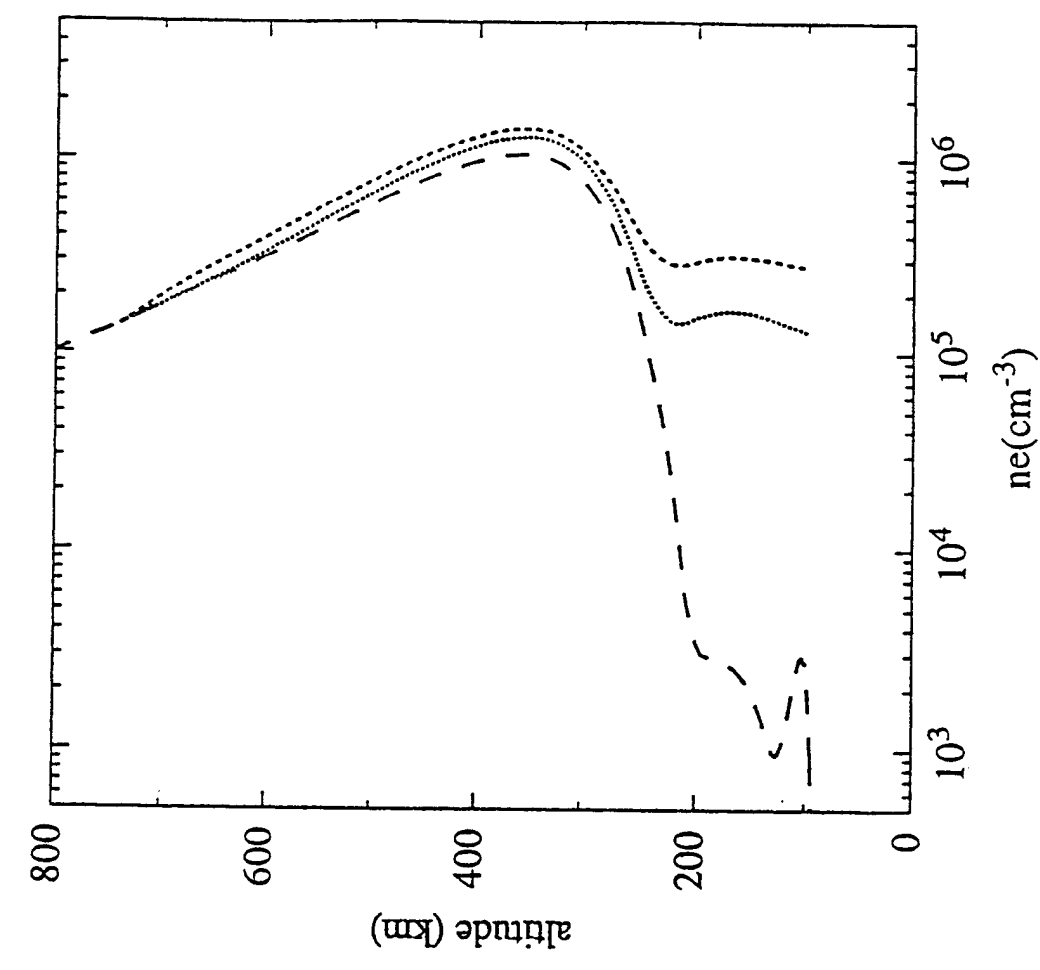
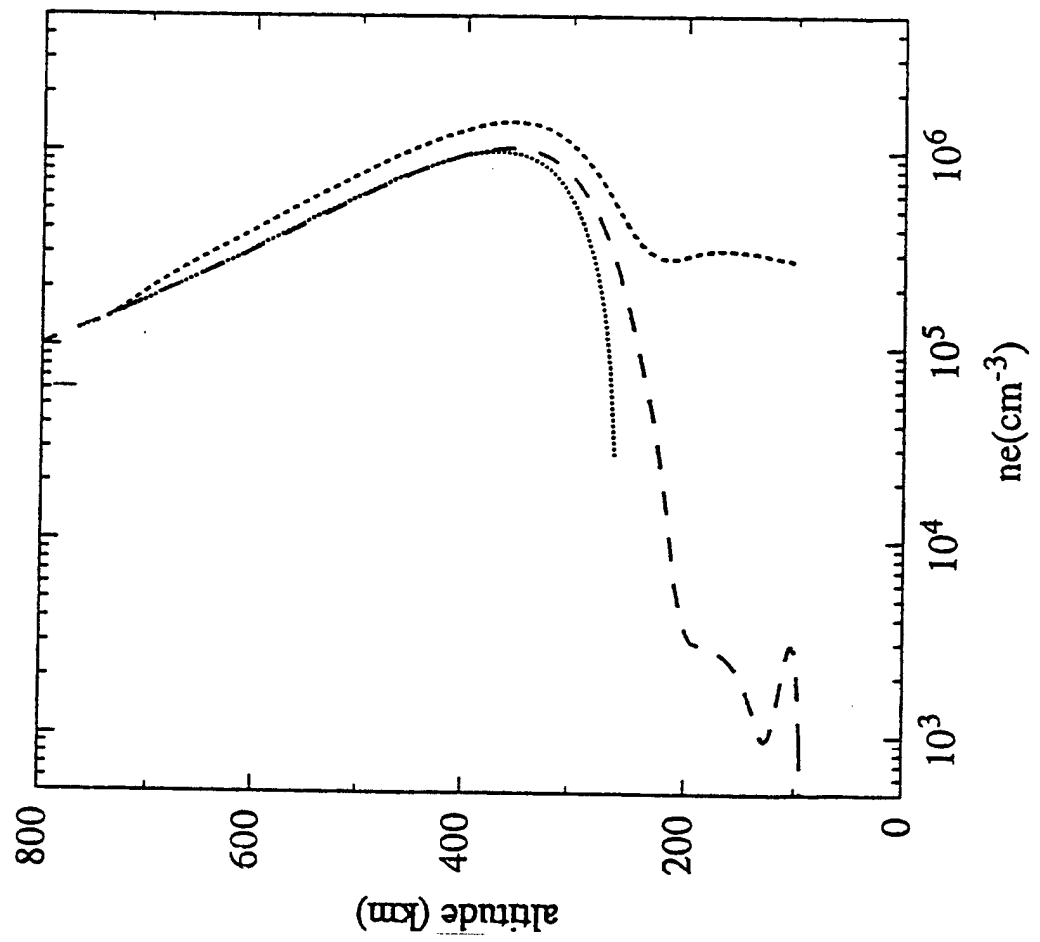


FIGURE 15. (a)

(b) PIM, Abel, and 1-di PIM -30 +0 20 UT
PIM, Abel, and 1-dia PIM -30 +0 +0 20 UT

a



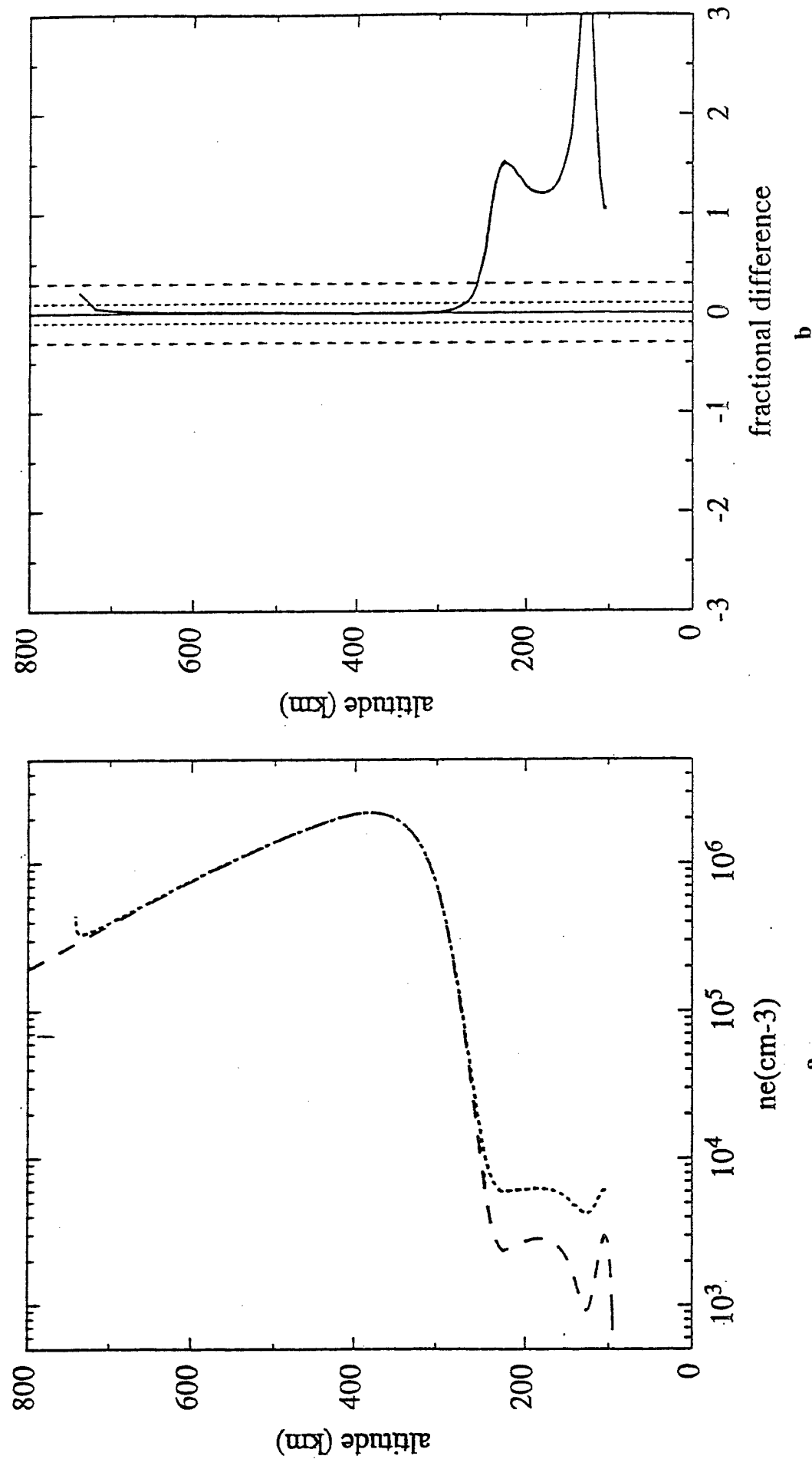


FIGURE 16. (a) PIM and Abel Sym PIM +3 TEC 0 0 0 0 UT
(b) PIM and Abel Differences Sym PIM +3 TEC 0 0 0 0 UT

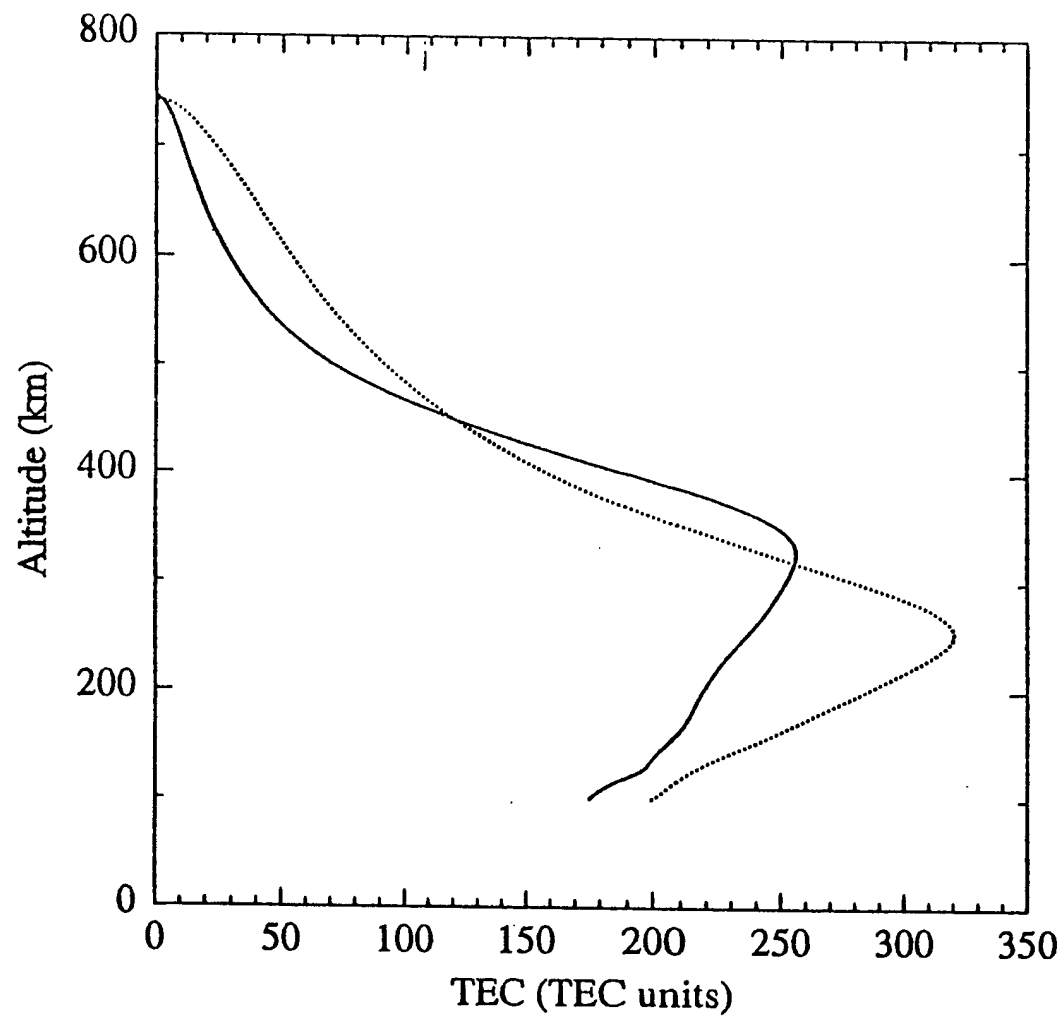


FIGURE 17. TEC PRN 16 and PIM Day 298 1350 UT

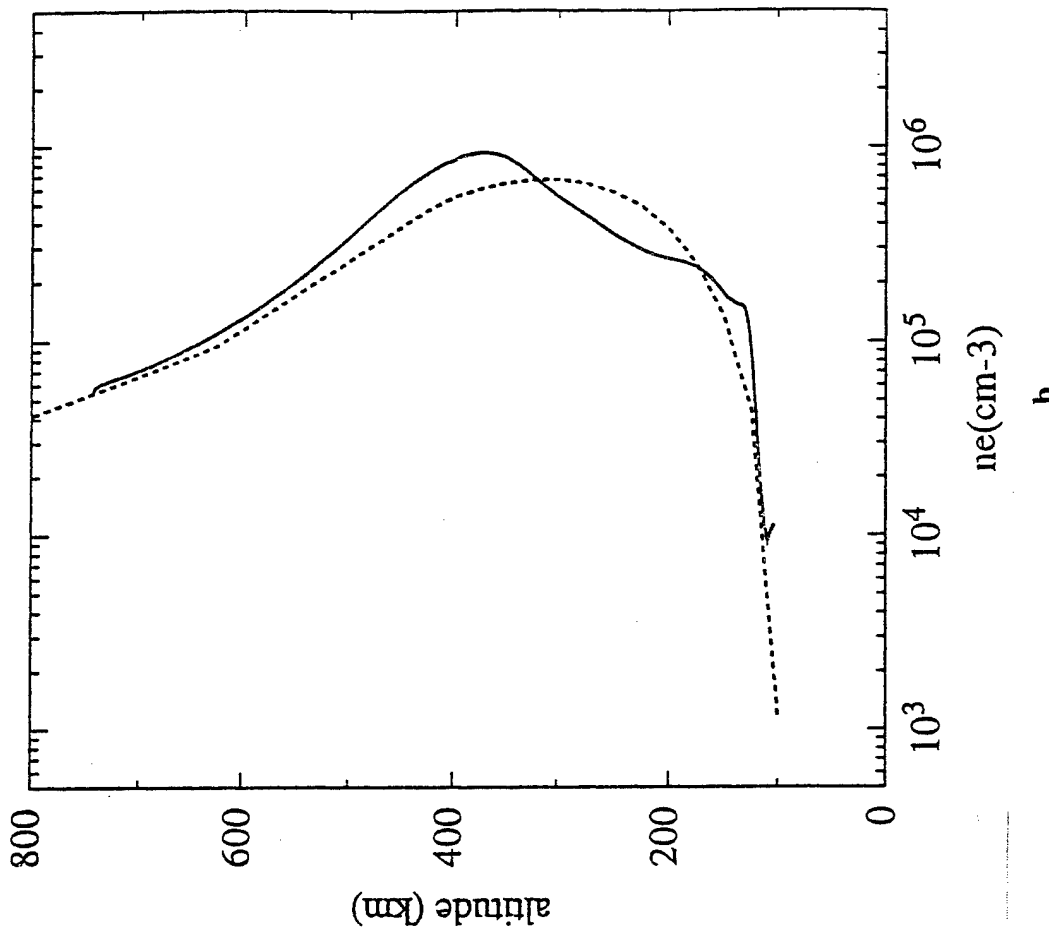
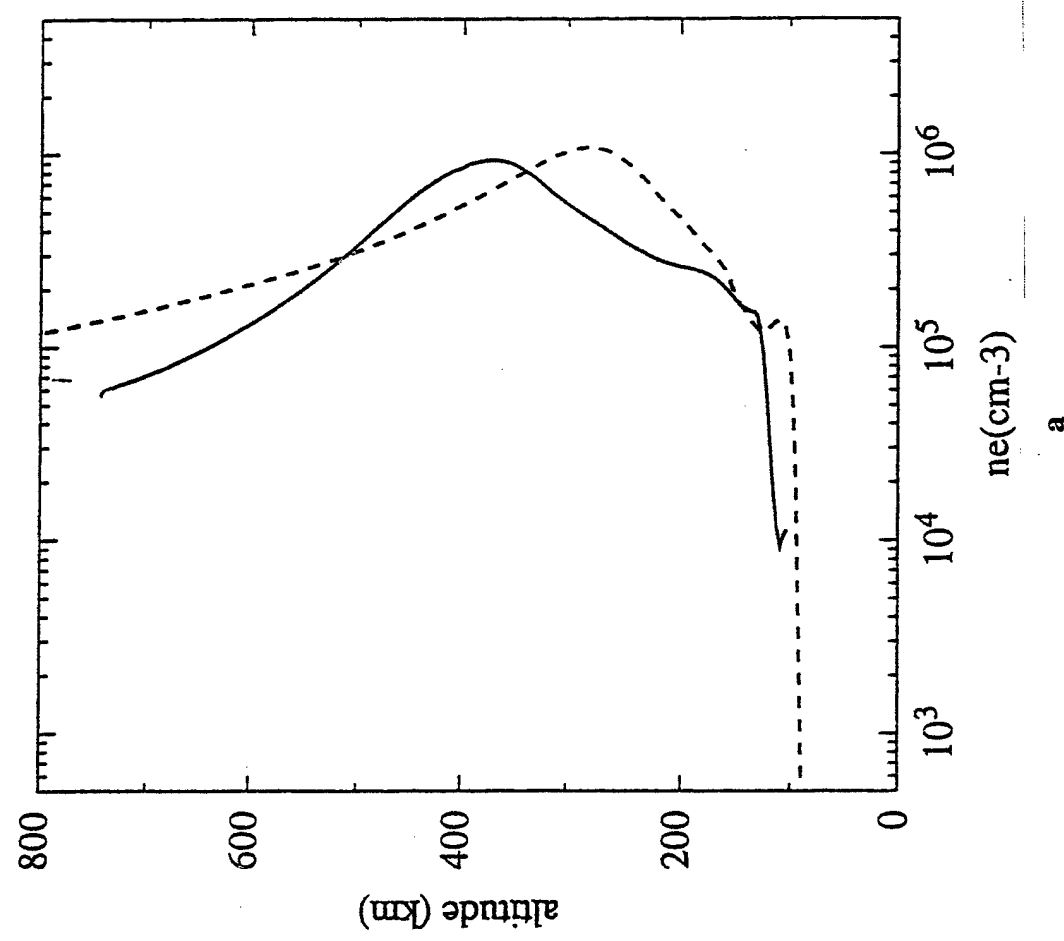


FIGURE 18. (a) Abel and PIM PRN 16 Test
(b) Abel and Bent PRN 16 Test

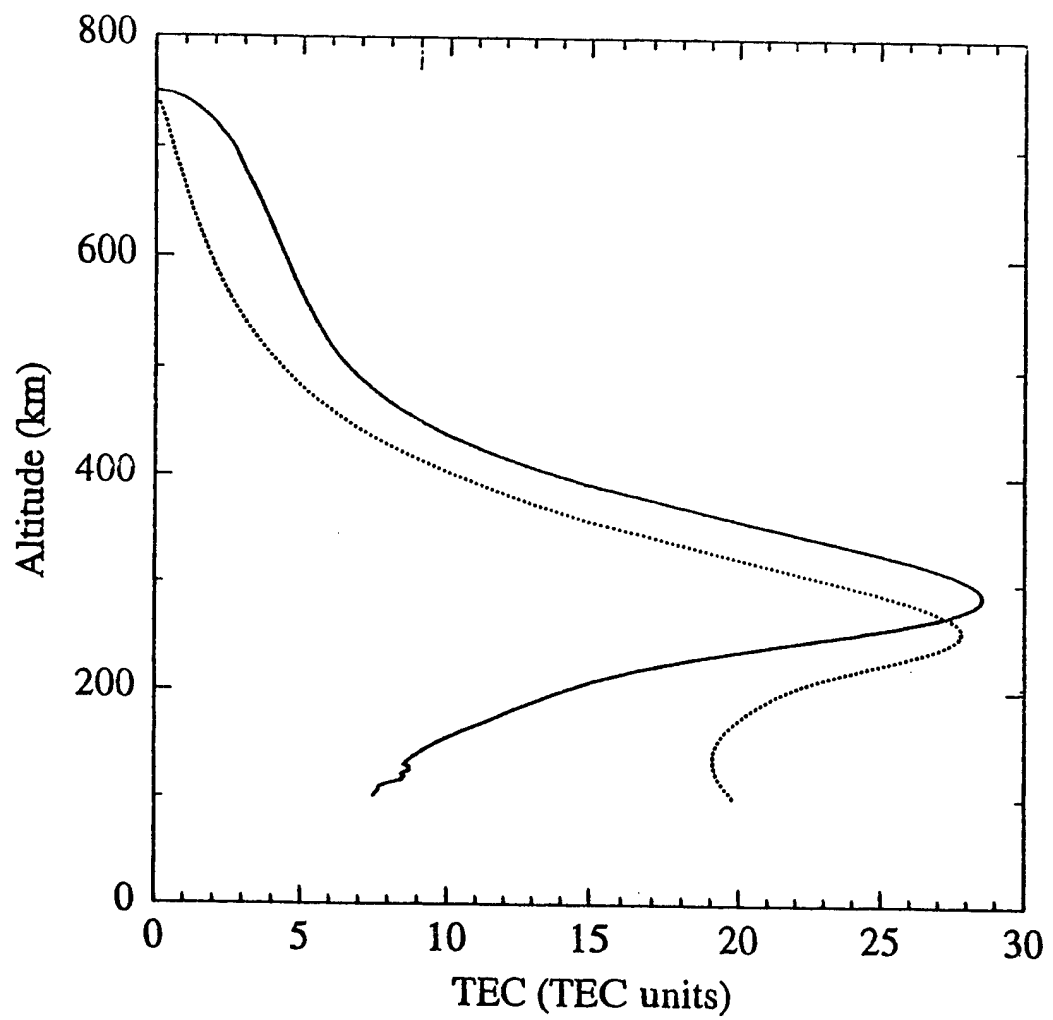


FIGURE 19. TEC PRN 6 and PIM Day 298 2123 UT

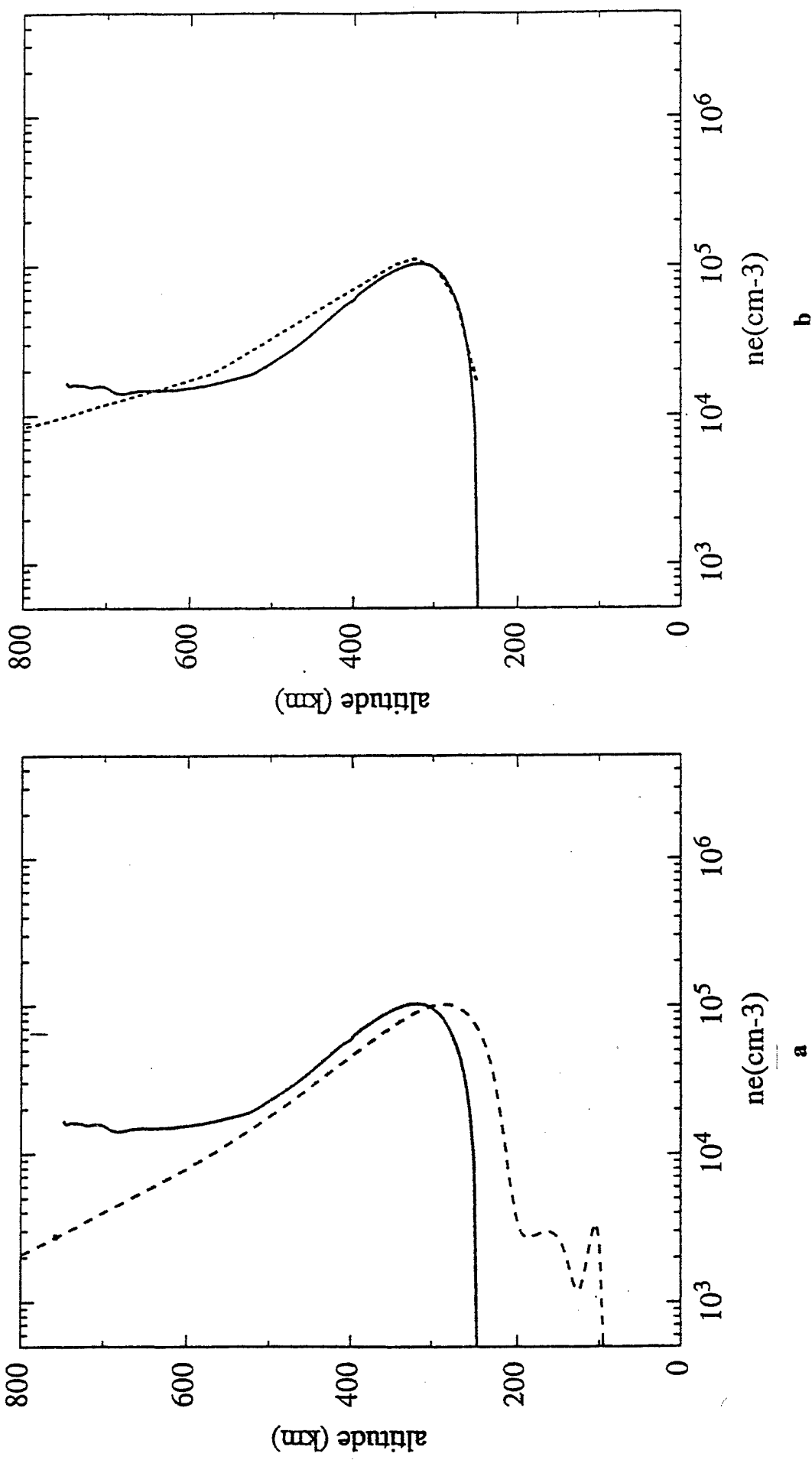


FIGURE 20. (a) Abel and PIM PRN 6 Test
 (b) Abel and Bent PRN 6 Test

Likewise, the thickness of the bottomside F-region is based on ionosonde measurements and has similar problems in coverage. The topside F-region is based on Alouette 1 and 2 topside sounder measurements from 1962 - 1966 [*Llewellyn and Bent*, 1973], however this period included only solar minimum and low solar moderate ($F10.7 < 130$) conditions. Given this non-uniform coverage in both location and time of the various databases, it is not surprising that IRI does an excellent job of specifying the ionosphere's climatology for some regions and times while having problems with other regions and times.

In this paper, we focus on the low latitude F_2 -region, a region where IRI has had some success reproducing the general climatology especially for lower levels of solar flux, but where there are some persistent disagreements between model and observations [*Abdu et al.*, 1996]. Early work based on total electron content (TEC) measurements found examples at low latitudes where IRI "severely underestimated" the observed TEC "during both day and night." Analysis of these cases suggested that the problem was in the relative shape of IRI's F_2 -region at low latitudes [*Bilitza*, 1985]. The topside of this layer comes from the Bent model [*Llewellyn and Bent*, 1973] and a correction to IRI's implementation of that model appeared in IRI-86. While this produced better agreement with satellite and incoherent scatter data, it was noted at the time that the new topside formula "only removed half of the difference between measured and predicted" TEC at the magnetic equator [*Bilitza*, 1985]. Further, while IRI-86 appeared to do a reasonable job at low solar activity, comparisons with in situ satellite measurements during high solar activity indicated that IRI's topside profile still significantly underestimated the observations [*Bilitza et al.*, 1987]. The other half of the "shape of the F_2 -region" is the bottomside of the F_2 -layer, which is described by an analytic function parameterized in terms of a thickness parameter for which IRI offers two options. The recommended option in most cases comes from the *Gulyaeva et al.* [1987] model for the half-density height. However, this bottomside thickness has also had some problems at low latitudes. *Mahajan et al.* [1995] showed using Arecibo incoherent scatter radar data that IRI produced a bottomside that was too thick by differing amounts depending on season and improvements to IRI have been suggested based on this work [*Gulyaeva et al.*, 1996]. Comparisons to digisonde data [*Reinisch and Huang*, 1996] have likewise shown some differences between data and IRI with the most dramatic differences occurring in August 1993 at Jicamarca where IRI's bottomside F_2 -layer was seen to be tens of kilometers thinner than observed. Finally, we turn to the F_2 -peak density (N_mF_2) and height (h_mF_2) which are used in IRI to complete the definition of the F-region. For these two parameters, the most persistent problem at low latitudes has been with h_mF_2 and, in particular, the inability of IRI in certain periods to reproduce the observed rising in altitude of the F_2 -layer just after sunset [*Bilitza et al.*, 1993; *Abdu et al.*, 1996].

As mentioned, the source of these problems is the non-uniform coverage of the available data. This is a particular problem at low-latitudes because vertical $\mathbf{E} \times \mathbf{B}$ drift leads to the formation of the equatorial anomaly and the development of a complex morphology quite different from that of the mid latitudes. However, the problems at low latitudes are also exacerbated by the large day-to-day variability of this region. In particular, it is problematic at best to attempt to model a feature such as the equatorial anomaly in terms of monthly medians when all the characteristics of the anomaly (intensity, location, extent, latitudinal shape) are known to vary greatly day-to-day. For example, due to the changing position and extent of the anomaly a single low latitude ground station can day-to-day effectively be sampling different geophysical regions. Assembling data averages from several such stations can result in a smeared out anomaly that is not

representative of an actual anomaly [Rawer, 1995]. While for some purposes such an average ionosphere is all that is needed, for other uses it is critical to have a representative or "typical" ionosphere.

One effect of the issues described above is that theoretical modeling has begun to appear as a complementary approach to strict empirical modeling. Rush *et al.* [1983, 1984] used theoretical modeling to fill in the data gaps over the mid-latitude oceans and along with ground-based ionosonde observations produced an improved set of maps of the F_2 peak critical frequency (f_oF_2). Such maps are the sources used by IRI for f_oF_2 and hence N_mF_2 . Further improvements to the f_oF_2 maps were made using theory over the oceans, a larger data base of ionosondes, and a harmonic analysis that was latitude dependent [Fox and McNamara, 1988]. At about the same time, efforts appeared that used first-principles theoretical models to produce parameterized models that would describe low latitude theoretical morphology [Anderson *et al.*, 1987, 1989]. The purpose was to produce a representative equatorial anomaly rather than a smeared out average anomaly [Daniell *et al.*, 1995]. In this paper, we propose a new option for IRI which would allow the results of low latitude theoretical modeling of electron density to be incorporated directly into IRI. The purpose is to both provide an improvement to IRI as well as to illustrate one way in which our theoretical understanding can be used to fill in the gaps of the observational databases used by IRI. In the next section, we present some observations compared with IRI-90 in order to quantitatively illustrate some of problems outlined above. This is followed by a description of the theoretical modeling of the low latitude ionosphere, an example of a PIM option to IRI, and finally a discussion and conclusion section.

Section 2 - Observations

In this section, we originally presented a comparison between IRI and Jicamarca observations from a particular day. The point of this comparison was to simply illustrate the type of problem that can be encountered at low latitudes when comparing IRI and actual observations. However, given that IRI is a model of monthly profiles, it should not be expected to necessarily reproduce the profiles on a given day. While the broad shape of the afternoon profiles and the post sunset lifting of the layer are not rare events and occur regularly, in order to validate that IRI has in fact a low latitude problem, comparisons need to be made between some sort of averaged data and IRI. In Figures 21-23, which are adapted from Creamer [1992], we show the hourly averaged data from several years of Jicamarca observations for moderate solar flux conditions. The December solstice refers to data taken during November through February and the June solstice refers to data from May to August. The equinox period was taken to be March and April along with September and October. These plots also include results from IRI-90 and the PIM. In this section, we will focus on the data (solid curves) and IRI-90 (dashed curves) results. PIM results (dotted curves) will be discussed in the following section. The IRI runs were made using a sunspot number of 80 and for days of the year 1, 100, and 182. The data are from days where the F10.7 ranged from 100 to 150.

We begin by noting that the observed profiles (solid curves) are generally broader than IRI-90 (dashed curves) though in several cases IRI-90 does a reasonable job. In Figure 21 (1200 LT) we see that for the December solstice, the shape of IRI's profile compares quite well with the averaged data. At equinox, we begin to see some differences in both the topside and bottomside shapes between IRI and data. For the June solstice, the differences in the bottomside shape are

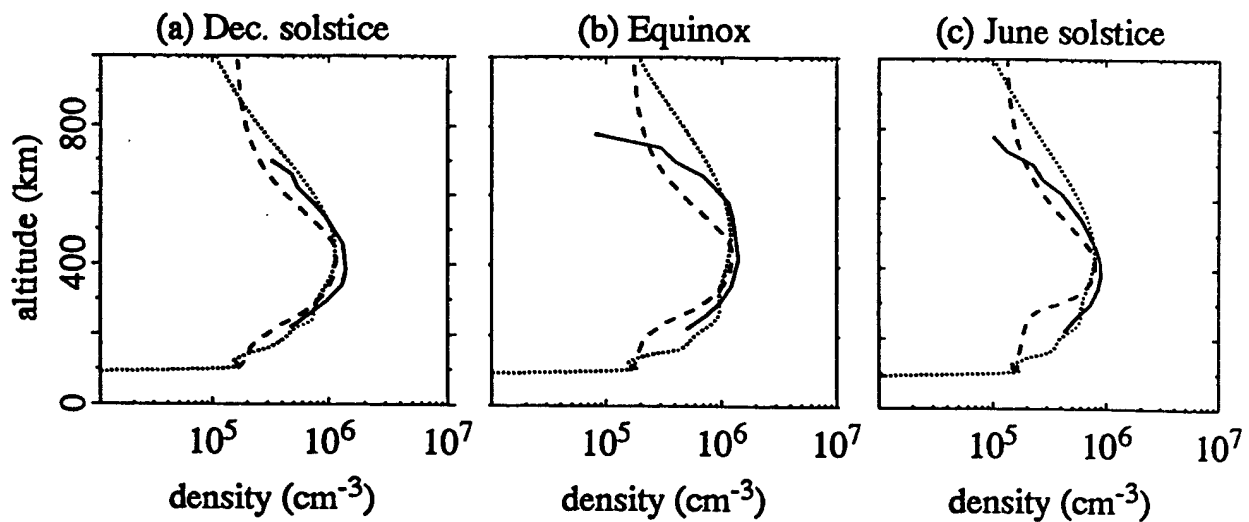


FIGURE 21. Density Profiles of PIM, IRI-90 and Jicamarca Data 1200 LT

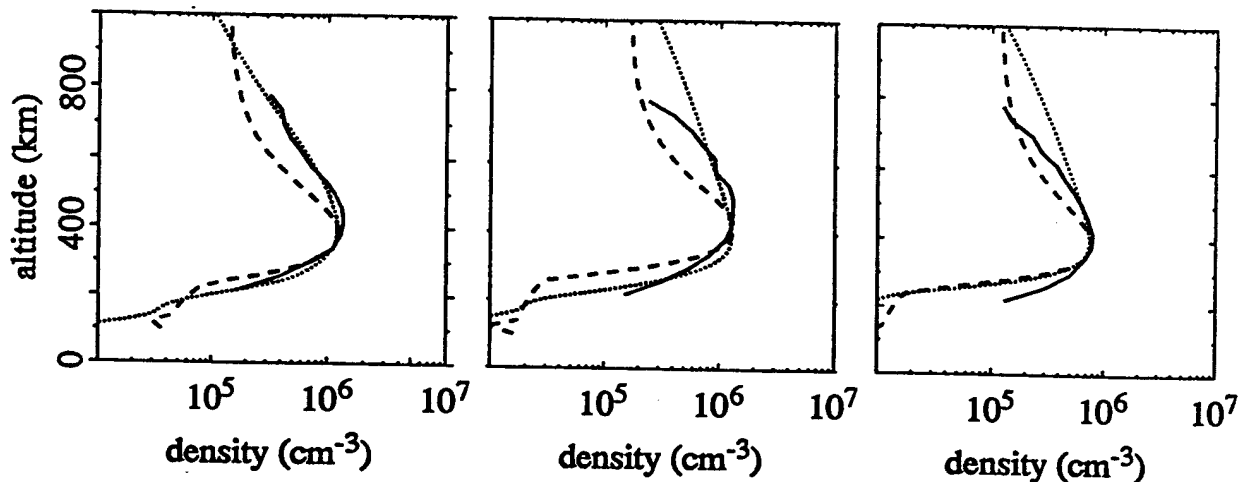


FIGURE 22. Density Profiles of PIM, IRI-90 and Jicamarca Data 1800 LT

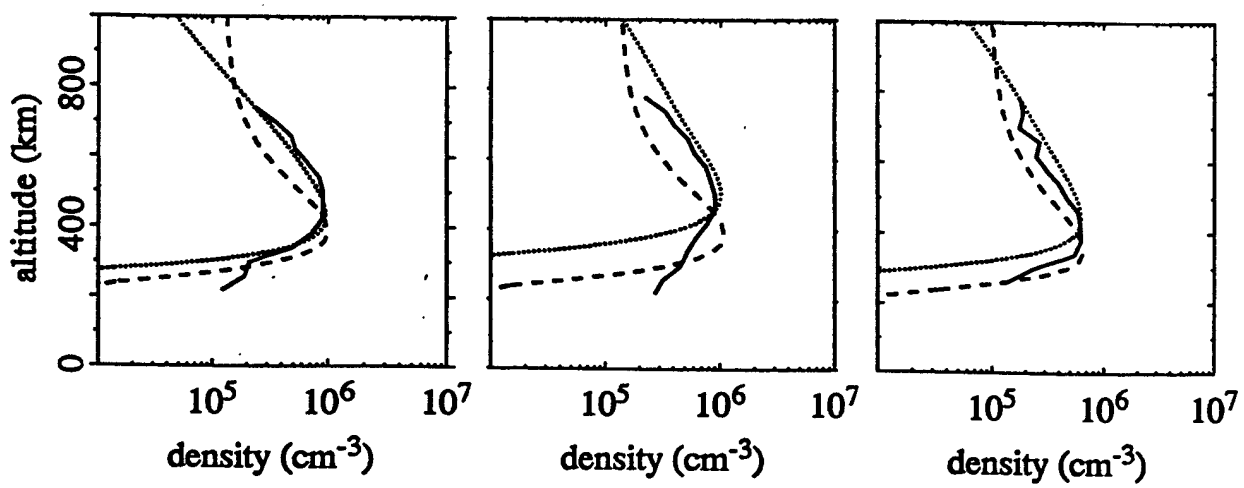


FIGURE 23. Density Profiles of PIM, IRI-90 and Jicamarca Data 2000 LT

most apparent. In Figure 22 (1800 LT) we see similar trends with clear differences between IRI-90 and data in topside shapes during the December solstice and the equinox and bottomside differences during the June solstice and the equinox. Finally, in Figure 23 (2000 LT), the post sunset lifting of the layer is evident (solid curves) during the December solstice and the equinox and is seen to be missed by IRI-90 (dashed curves). There is a smaller amount of lifting of the layer for the June solstice, but it is difficult to see given that the data was placed into 40 km bins when producing these average profiles. If $h_m F_2$ is taken from the unbinned data and then averaged, the June solstice results then show a peak rise of just 16 km between 1700 LT and 2000 LT. In contrast, the equinox shows a 55 km increase. Similar features are seen for maximum solar flux conditions but not for solar minimum conditions. IRI-90 also consistently shows an increased scale height above 700 km. While the data shows some evidence that this is not the case (see equinox at 1200 LT and 1800 LT), in general these observations are too low in altitude to clearly determine whether this increased scale height is appropriate.

While the observations shown thus far come from one location, similar features are also evident in other longitude sectors. Many of the works referenced in the introduction describe studies that included data from other longitude sectors. In Figure 24, we present profiles [*R. Tsunoda, personal communication, 1995*] observed by the Kwajalein incoherent scatter radar located near the equator in the Pacific sector. On the left is a profile from the early morning before the upward drift $\mathbf{E} \times \mathbf{B}$ drift has acted to broaden the peak, while on the right we see later in the day the characteristic broad layer of the low-latitude daytime that results from the upward $\mathbf{E} \times \mathbf{B}$ drift. Further, it has been clearly established that the equatorial anomaly is global in nature [*Walker, 1981; Su et al., 1996*] and that the $\mathbf{E} \times \mathbf{B}$ drift though different in detail is similar at all longitudes [*Fejer et al., 1995*]. Given that the discrepancies described above are related to the effects of vertical $\mathbf{E} \times \mathbf{B}$ drift and the equatorial anomaly, it is then consistent that IRI would have these low latitude problems at other longitudes.

Section 3 - Theoretical Modeling

In this section, we expanded our discussion to clarify the relation between PIM and GTIM and included comparisons between PIM and averaged Jicamarca data.

Over the last three decades, there have been many theoretical studies of the equatorial F_2 region and a number of computer models have been developed that reproduce the basic features of this region. Most recently, these models have evolved to the point that given realistic inputs for a particular day they are capable of reproducing the ionosphere of that day [*Preble, et al., 1994*]. One such model is the GTIM which calculates electron density profiles as a function of location and time by solving ion continuity and momentum equations. For the F-region, the O^+ ion density is determined by numerically solving the time-dependent ion (O^+) continuity equation. The needed velocity parallel to the magnetic field comes from combining the electron and ion momentum equations. The perpendicular velocity is taken as the $\mathbf{E} \times \mathbf{B}$ drift where the electric field has to be provided as an input to the model. A variety of other geophysical inputs are also required including the neutral constituents, temperature, and winds; the electron and ion temperatures; the solar extreme ultraviolet (EUV) fluxes; and the geomagnetic field. For the lower altitudes, the molecular ions are determined by numerically solving the steady-state local approximation of four coupled ion continuity equations [*Anderson et al., 1996*]. In Figure 25, we present vertical profiles for 1200 and 1900 LT from GTIM simulations (dotted curves) that used

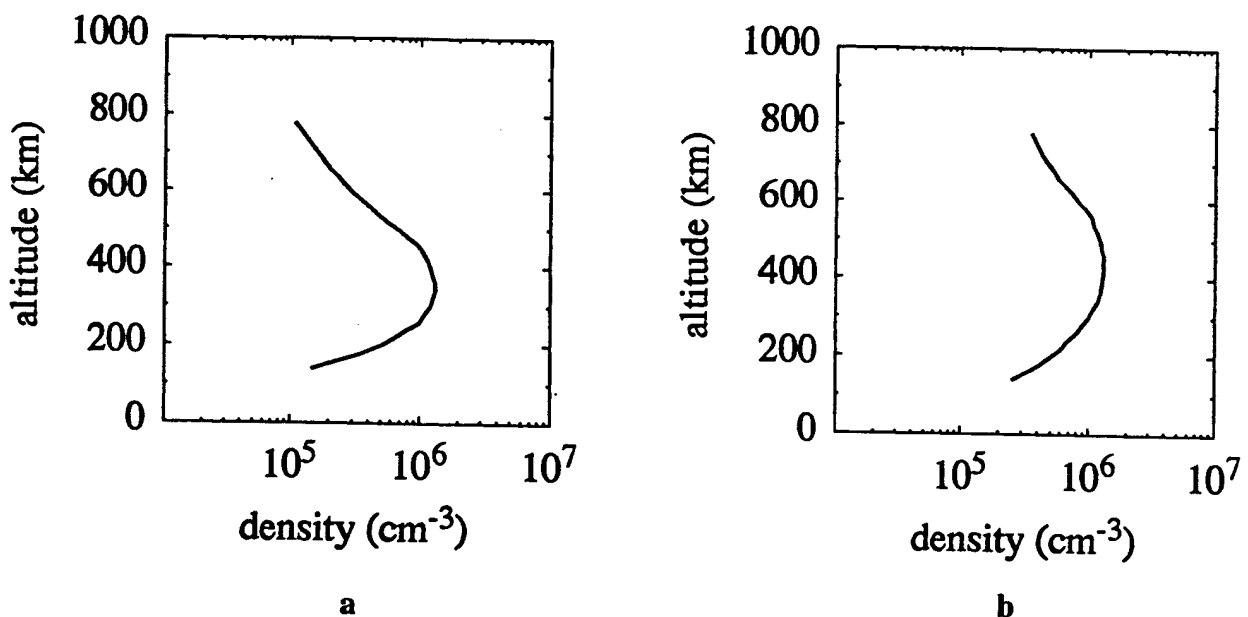


FIGURE 24. (a) Profiles from Kwajalein Radar Early Morning
 (b) Profiles from Kwajalein Radar Late in Day

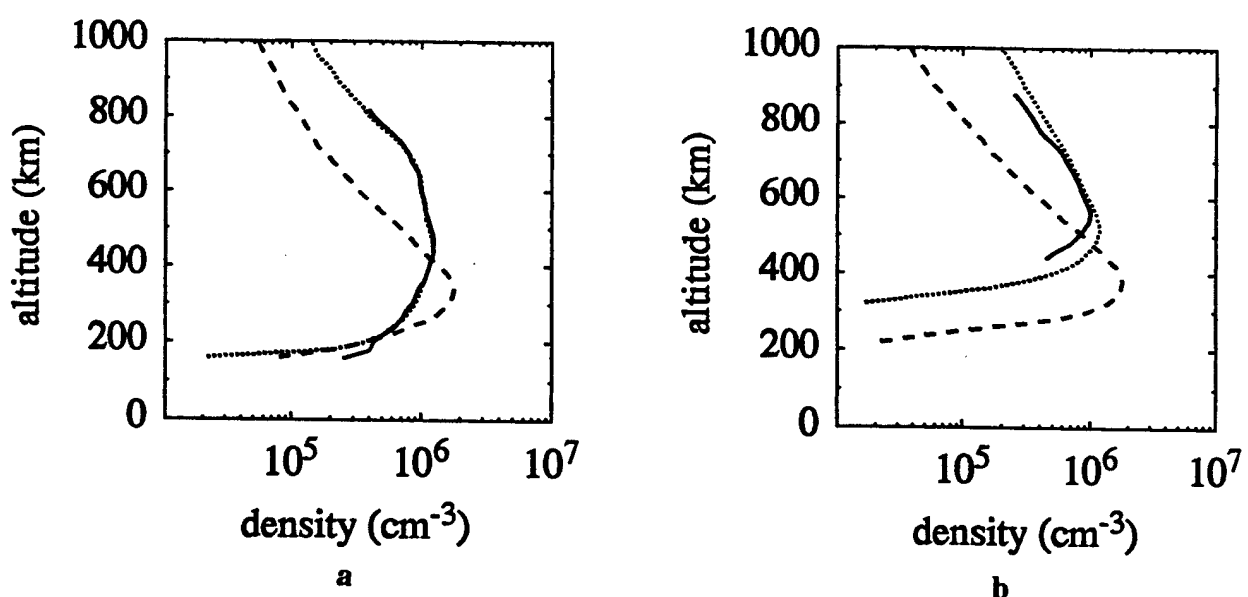


FIGURE 25. (a) GTIM and Jicamarca Profiles 1200 LT
 (b) GTIM and Jicamarca Profiles 1900 LT

the Jicamarca observed upward $\mathbf{E} \times \mathbf{B}$ drift of October 1 and 2, 1970. We also include in the plot the electron density profiles (solid curves) observed by the Jicamarca radar at those times. We see that when the observed drift is used as an input to the model that the agreement between model and observation is excellent. Further, we see that the model reproduces both the broad profile shape of the daytime and the lifting of the F_2 layer during the post-sunset period. The additional curves (dashed curves) are GTIM results when zero vertical $\mathbf{E} \times \mathbf{B}$ drift was used as input. These simulations illustrate the critical role that the magnitude of the $\mathbf{E} \times \mathbf{B}$ vertical drift has in determining both the shape of the daytime profile and the post sunset rising of the F_2 layer.

Recently, a computationally fast PIM was developed at the Phillips Laboratory Geophysics Directorate as part of a global, real-time ionospheric specification model called PRISM which is presently operational at the Air Force 50th Weather Squadron (50WS) in Colorado Springs [Daniell *et al.*, 1995]. PIM is based on many runs of several theoretical ionospheric models and, as such, is a global ionospheric model based on theoretical climatology rather than empirical climatology. For the low latitudes, the theoretical model used was an early version of GTIM. It was run under three solar cycle conditions (low, middle, and high F10.7 cm flux values) and three seasons (fall/spring equinox, summer, and winter solstice periods) for four longitude sectors (American, Brazilian, European/Indian, and Pacific). Electron density profiles every 2° latitude and every hour local time were parameterized by 9 Empirical Orthonormal Functions (EOFs). At low and mid-latitudes these EOFs were analytically fit in latitude and kept in tabular form over the 24-hour period. These tables and functions comprise the low-latitude portion of PIM and reproduce very accurately the electron density profiles generated by GTIM.

Given the success of theoretical models in reproducing the basic features of the low latitudes, we would expect that the PIM should likewise reproduce those features. In Figures 21-23, we have included PIM results (dotted curves) along with the averaged Jicamarca data (solid curves) and the IRI-90 (dashed curves) results. In Figure 21 for the December solstice, we see that the PIM produces a profile that is broader than the data. Both the PIM and IRI-90 underestimate $N_m F_2$ and to some extent the topside and bottomside data seem to split the difference between PIM and IRI-90. At the equinox, PIM's (dotted curve) topside shape gives good agreement with data (solid curve) up to around 600 km. Above that height both the PIM and IRI miss the sharp fall off in the data. Again in the bottomside, the data distribution splits the difference between the models, though if we normalize IRI to the F_2 peak of the observations, IRI (dashed curve) has the better bottomside shape. Finally for June solstice, the PIM produces a broader layer than IRI-90 with the data falling between the two models. However, this time it is the PIM that has the better bottomside shape with IRI-90 showing a much thinner bottomside than seen in the data. Turning to Figure 22 and 1800 LT, we again see a broader PIM (dotted curves) as compared to IRI-90 (dashed curves). For December, the PIM's topside agrees quite nicely with the data while IRI-90 shows a significantly different shape. Moving to equinox, up to around 600 km the PIM gives reasonable agreement with the observed topside but as was the case at 1200 LT both the PIM and IRI-90 miss the sharp fall off seen in the data at higher altitudes. In the bottomside the observed layer appears to be a bit thicker than either model. The June solstice again shows an observed topside shape that falls between the two models and a observed bottomside shape that is thicker than either model. At 2000 LT (Figure 23) similar trends continue. The PIM gives good agreement with observations over much of the F region. In particular, the PIM captures the lifting of the layer that was missed by IRI-90. For equinox, the PIM captures the topside shape and the lifting of the layer. However, both IRI-90 and PIM produce much thinner bottomsides

than seen in the averaged data. Finally for June solstice, the PIM shows a layer that has risen to a higher altitude ($h_m F_2 \sim 440$ km) than that seen in the observations ($h_m F_2 \sim 410$ km), while IRI-90 is down at a lower altitude ($h_m F_2 \sim 355$ km).

Having seen how both IRI and the PIM compare to data from Jicamarca for solar moderate conditions, let us now compare the two models over a larger region and for solar maximum conditions. In Figure 26, we directly compare the PIM and IRI-90 profiles at 1700 UT in Jicamarca longitude meridian. The local time is around 1200 and we see that the PIM produces a much broader F layer around the magnetic equator than does IRI-90. However, the PIM anomaly falls off much faster with latitude than does IRI-90 so that 20° north of the magnetic equator (around 10° north geographic) IRI-90 is producing a thicker layer. This illustrates how in regions of great variability theoretical models can produce sharper features (in this case an anomaly that is narrower in latitude) than may be seen in models based on averaged data. In Figure 27, it is $h_m F_2$ that is compared over the entire globe at 0 UT and we see that the largest differences between the PIM and IRI-90 are confined to the post sunset period near the equator. The topside half thicknesses are compared in Figure 28 and here a sizable difference is seen near the magnetic equator but extended over 180° in longitude. This also points out how the differences in thickness between models are not confined to just one longitude sector. In Figure 26, a clear difference in layer thickness was seen in the American sector at 1700 UT. At 1200 UT, this difference is seen in the European/Indian sector.

Section 5

While Section 4 required few changes, Section 5 was considerably expanded by including a discussion of the validation of the PIM as well as the effect of using IRI-95 versus IRI-90.

While we have demonstrated the possibility and potential of the PIM option, the same type of validation is needed for the PIM as is necessary for any version of IRI. However, validating the PIM option faces the same problems that have hampered IRI validations; that is, the availability of suitable observations. To date, validation of the low-latitude portion of the PIM has been confined to the American sector, primarily to comparisons with data from the Jicamarca incoherent scatter radar. Further validation for the PIM option awaits other data sources. One near term possibility is the TEC observations that are available from the dual frequency, dispersive radar on the TOPEX/POSEIDON satellite [Bilitza *et al.*, 1996]. These observations, which began around the beginning of 1993, would appear to offer an exciting opportunity for low latitude testing of IRI, PIM and GTIM.

A key issue when considering the validation of models such as the IRI or the PIM is that of day-to-day variability. This is especially critical in a region, such as the low latitudes, where that variability can be quite large. This issue manifests itself in several ways. For example, the process by which one constructs an average from data becomes critical especially if dealing with any type of variable structure. As mentioned in the introduction, the latitude extent of the anomaly can easily be smeared out if one takes routine averages of ground based measurements. Another example is that of the shape of the altitude profile changing markedly from day to day even when the solar and magnetic conditions are not markedly different. In that case an "average profile" may represent only one of the possible profile shapes. In Figure 21 for the December solstice, we see an average profile with a topside shape falling between IRI-90 and the PIM. If

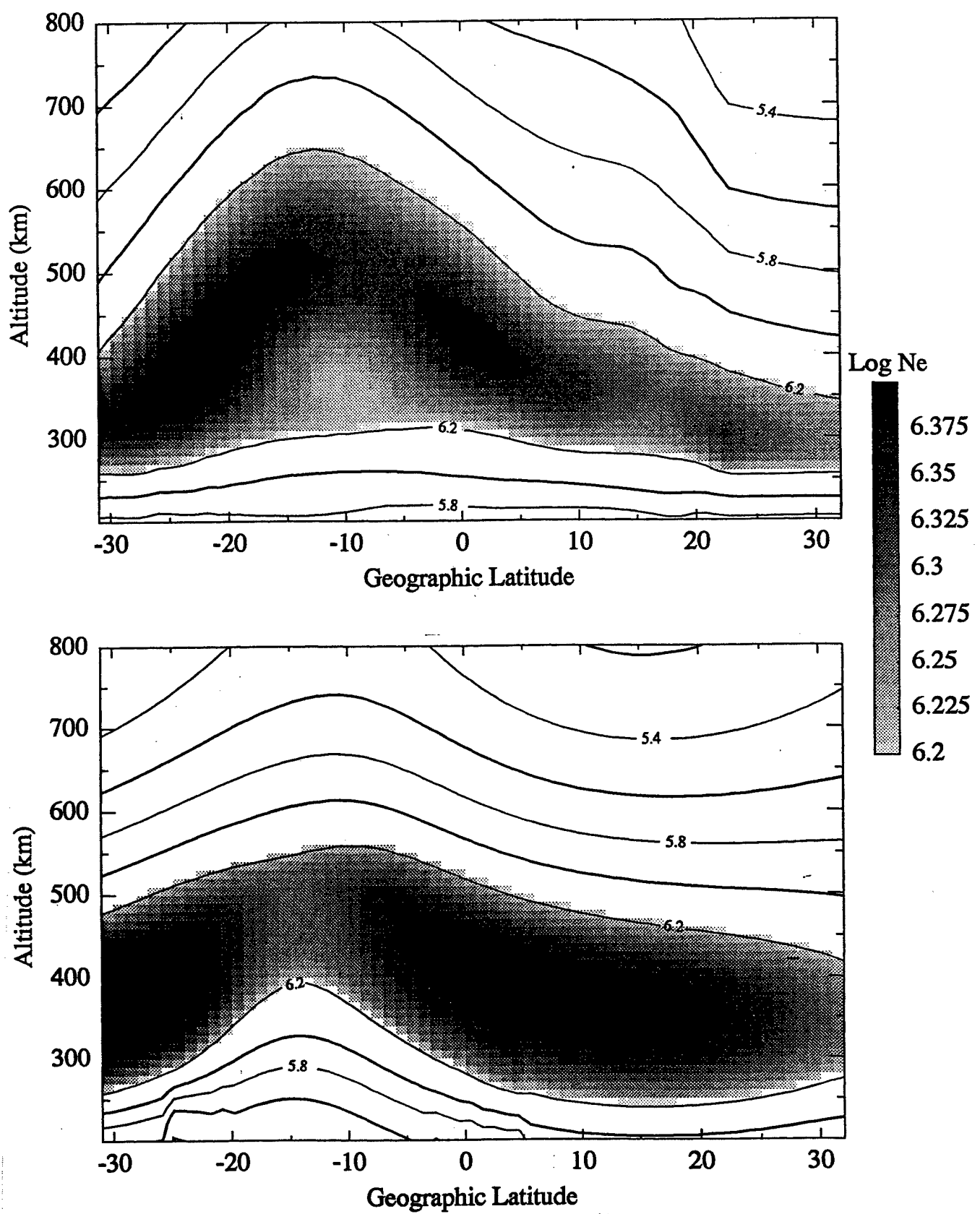


FIGURE 26. (top) PIM Electron Density Profile
 (bottom) IRI Electron Density Profile

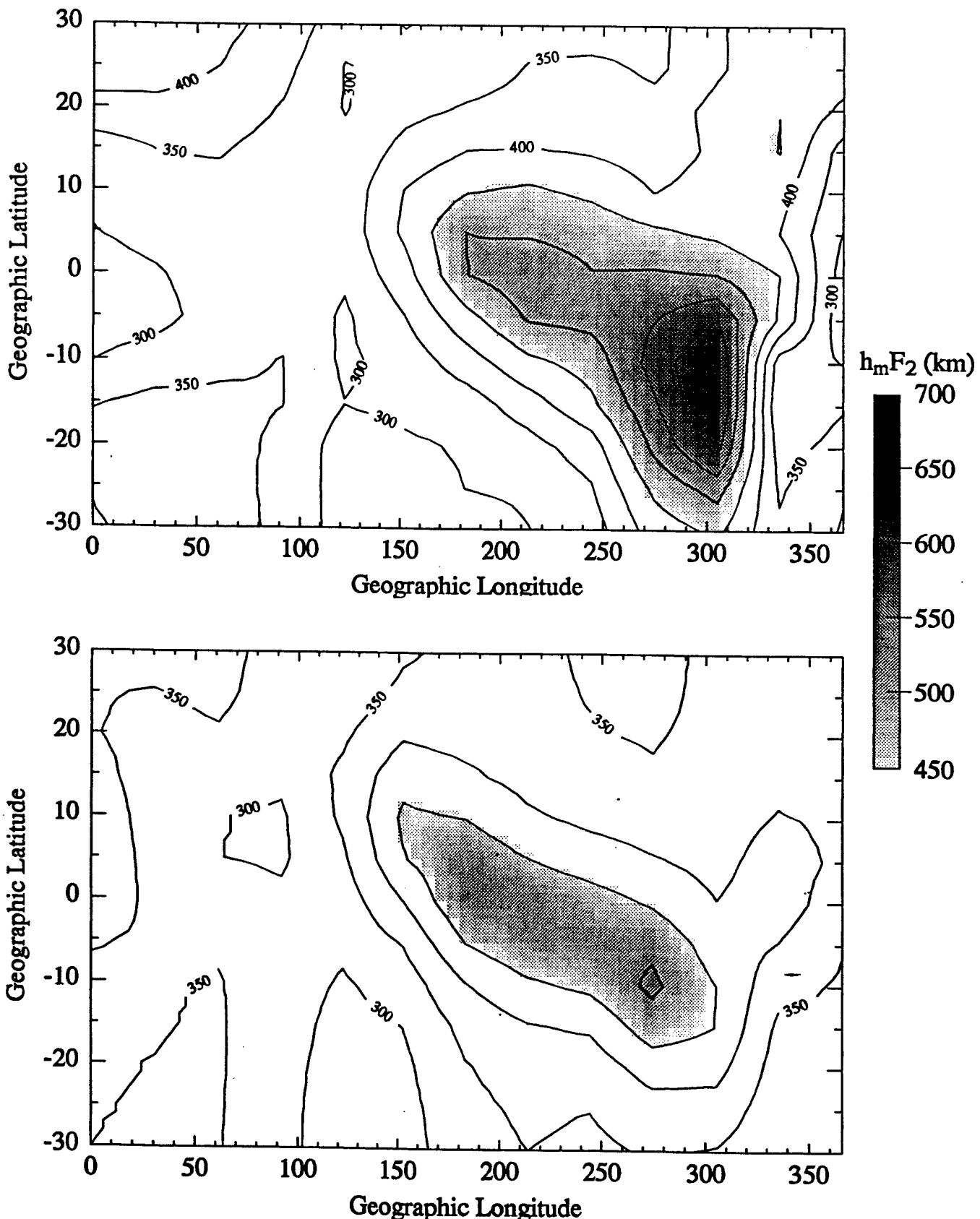


FIGURE 27. (top) PIM h_mF_2
 (bottom) IRI h_mF_2

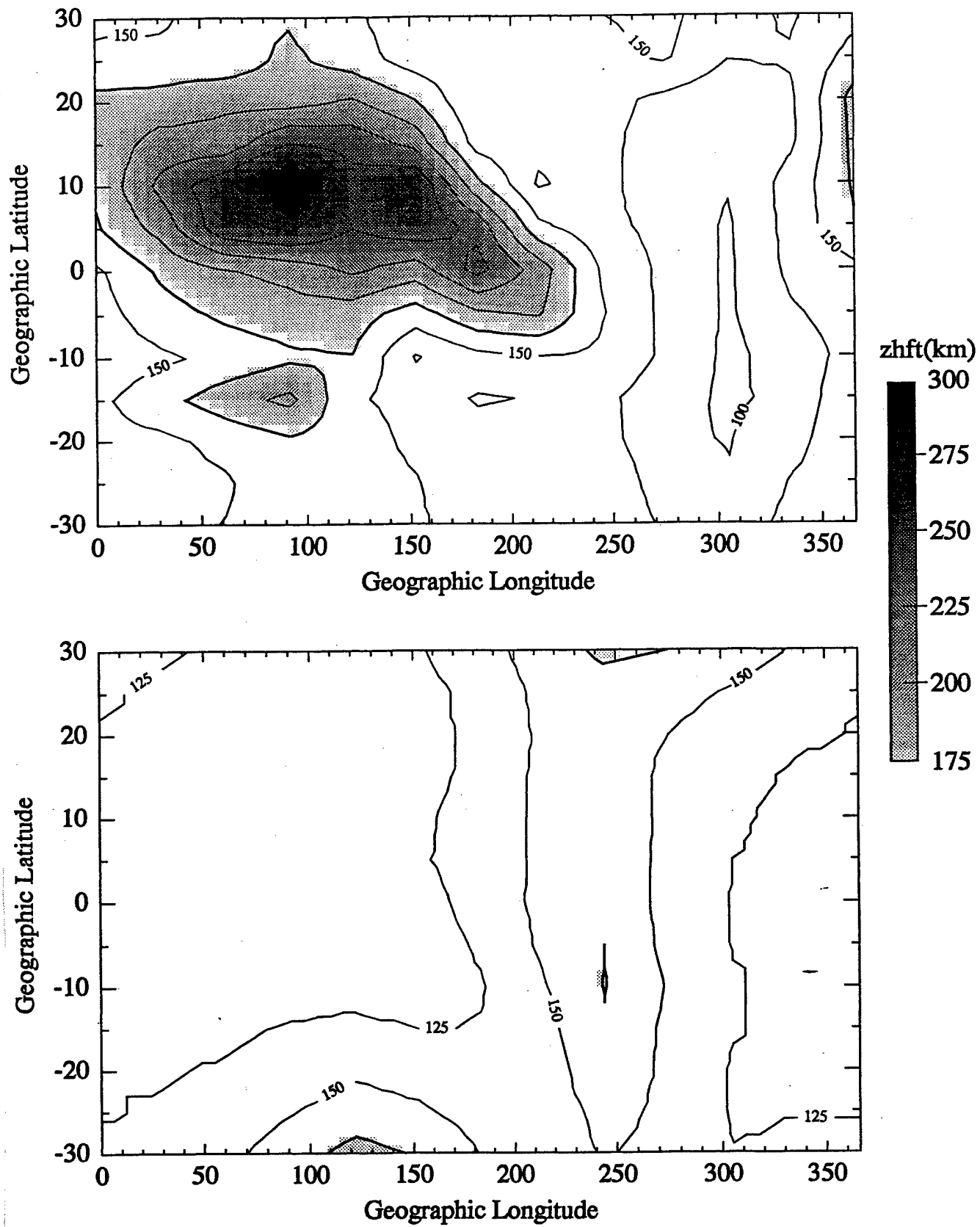


FIGURE 28. (top) PIM Topside Half Thickness
 (bottom) IRI Topside Half Thickness

one examines the scatter plots of the 18 profiles that went into making up this average [Creamer, 1992], you see a range of profiles that go from very broad shapes, low peak densities (7×10^5), and high $h_m F_{2s}$ (> 400 km) to thin topsides (thinner than IRI), high peak densities (2.5×10^6), and lower $h_m F_{2s}$ (~ 325 km). In this case, both IRI and the PIM fall within this range of profile shapes. We can speculate that the PIM profile shape is representative of those days when the electric field was of a certain strength, while IRI, based on solar minimum data, possibly represents those profiles from days with weaker electric fields. But all the cases fall into the same category of magnetically quiet, moderate solar conditions. Of course with such a range of shapes, it is difficult to determine what is "typical" and there is little reason to expect that a theoretical model driven by an average $E \times B$ drift based on one limited set of drift data will necessarily produce the "average" seen in a limited set of electron density profile data from a different period. In such regions with large variability, what is needed for IRI is an expanded capability that quantifies the variations about the "average profile." As for the PIM, it is planned that the next version will be parameterized by some sort of electric field strength parameter. In order to validate such a version of the PIM and the above speculation, it would be useful to perform a GTIM model study where a database of simultaneous vertical drift and electron density profile measurements are available. In that case, one could verify whether the observed day-to-day variations in profile shape can be modeled as directly coming from the observed day-to-day variations in vertical drift.

The scale height differences above 700 km between the IRI-90 and the PIM profiles are an obvious issue that needs to be addressed as we consider the issue of model validation. As mentioned in Section 2, the increased scale height shown in IRI-90 suggests a transition from an O^+ dominated F region to an H^+ dominated topside. This suggestion comes from both theory and observations that have shown that this type scale height change occurs when this transition of species occurs [Bilitza, 1990]. Further, the transition heights observed at solar minimum are generally consistent with the transition heights evident in the IRI-90 profiles. That this is so is of course reasonable given that IRI's topside is based on solar minimum topside sounder data. However, observations have shown that the transition height moves up in altitude at higher levels of solar activity. This has been verified recently in a study of DMSP satellite data [West *et al.*, 1997] that showed during low solar activity the transition height is well below 800 km and well above 800 km during higher solar activity. Further for the times of the DMSP data, it was seen that the H^+ density at 800 km never gets much above 1 or 2×10^4 . In disagreement with this are the IRI-90 results that show for solar moderate conditions at 21.8 LT (the time of DMSP data) a scale height change at around 700 km and H^+ densities at 800 km of around 9×10^4 . An observational approach to this problem should come from topside sounder data. However, only a small part of the Alouette-ISIS topside sounder database has been available for use [Bilitza, 1994]. It is expected that if and when more of this database becomes available significant improvements can be made in IRI's topside morphology. On the theoretical side, we find that the PIM does not include H^+ and so obviously cannot describe the transition between species. Fortunately, a new version of GTIM is under development that includes H^+ at low-and mid-latitudes. It is anticipated that the next version of the PIM will be produced using this improved GTIM and thus should include the transition from O^+ to H^+ that occurs in the topside. The two issues discussed above (daily profile shape changes and O^+/H^+ transitions) are examples of the problems that arise in part from the lack of suitable databases. They are also examples of how theoretical models can be used to complement pure empirical modeling. That is, validated theory can serve to fill in the data gaps and provide a spatial and temporal framework when databases

are too sparse to do so. We expect that a next generation PIM that includes both H^+ and an electric field parameterization can play such a role and serve to complement strict empirical modeling.

Finally, this work was done using IRI-90; however, during the writing of this paper IRI-95 became available and could be run interactively via a World Wide Web site. We have rerun the cases shown in Figures 21-23 using IRI-95 and find essentially no differences in the topside and F_2 peak parameters. However for day 1 and 100, the bottomsides at 12 LT coming from IRI-95 are somewhat thinner than the IRI-90 results. Given these results, it is evident that essentially all our conclusions based on IRI-90 remain true for IRI-95.

2.5. Ionospheric Modeling Using Systems of Plasma Kinetic Equations

In certain regions of the ionosphere, plasma kinetic equations can be useful for studying problems where wave-particle interactions are important sources of particle heating and transport. However, a general system of kinetic equations coupled with Maxwell's equations forms a formidable set of equations. One approach for solving this set is to assume that the fluctuating E and B fields are known and can be used in a physical model that describes the wave-particle interactions. This model is then used in the set of equations to solve for the one-particle distribution function and the quasistatic electric field. However, difficulties still remain in self-consistently solving for the quasistatic (ambipolar field) electric field and the distribution function. In particular, it is not practical to attempt a direct numerical solution of Poisson's equation. The approach being explored here is to use a multi-energy-group (MEG) method to derive moment equations and to solve these equations for the moments and the ambipolar field. This electric field can then be used in solving a kinetic equation for the one-particle distribution function.

A multi-energy-group method of analyzing a system of plasma kinetic equations involves defining the one-particle distribution function for each type of particle as a sum of functions, one for each major energy group, and then constructing a set of moment equations. The set of equations that then need to be solved depend on the number of energy groups chosen and the method used to close the set of moment equations. We have been working on two versions of this method. One produces a set of 8 differential equations while the second involves 11 equations. These equations describe how 8 or 11 variables vary in one spatial dimension. A computer program was written that performs the symbolic manipulation needed to transform these sets of equations into a triangular form so they can be easily solved using standard techniques. This program also calculates the necessary derivatives and generates the FORTRAN code that is needed for the subroutines that are used by a standard differential equation solver. A driver program that uses the equation solver has been written and the first preliminary solutions for these sets of equations have been obtained.

Work began on developing a numerical solution to the kinetic equation. The first attempts have involved solving a differential equation in two velocity variables and one spatial variable. A split operator method is used with one operator describing the effects of gravity, the ambipolar electric field, and the magnetic field (mirroring force) while the other describes the effects of the wave-particle interactions. The most difficult step in writing the algorithm has been the proper handling of the coordinate grids as these have to be modified every half step as the equation is

integrated. A preliminary code was implemented and tested on several simple examples of the differential equation. The preliminary code was then rewritten several times to improve the way the coordinate grids were varied at each half step. In addition, numerical integration of results at the full step was used to see if the various moment equations were being satisfied. In several preliminary runs of the latest code, it was found that the moment equations were not being satisfied. Work continues to identify the reason for this.

3. OBSERVATIONAL DATABASES

3.1. Solar Cycle Dependence of Absolute Ionospheric Total Electron Content

The aim of this research is to aid in the development of an improved single frequency GPS user algorithm by defining an improved fit between TEC and long-term solar activity and to determine if that fit changes for different seasons and geographic locations. The ionosphere is the most substantial source of error in GPS positioning and navigation. Since the ionosphere is a dispersive medium, the dual-frequency GPS user can automatically correct for ionospheric effects. For the single frequency GPS user, the Ionospheric Correction Algorithm (ICA) was developed to correct for approximately 50 percent rms of the ionospheric error. The ICA was developed in 1975 using the Bent Model, a state-of-the-art empirical ionospheric model that was based on data recorded during an average solar cycle. Solar cycle maximum values since that period have been much higher. As a result, the ICA does not adequately represent periods of extremely high solar maximum activity. In addition, the ICA is deficient in describing the significant ionospheric changes that are characteristic of the equatorial and low-latitude regions. The study is accomplished by correlating values of the 10.7 cm solar radio flux ($F_{10.7}$) with a worldwide data base of f_0F2 measurements recorded from 1958 through 1992, a period covering almost four solar cycles. This study is further augmented with TEC from Faraday rotation measurements and TEC from dual-frequency GPS data recorded at Goldstone CA. A special emphasis will be placed on resolving whether there is a *real* saturation effect in TEC at extreme levels of 10.7 cm solar flux as evidenced in work by *Balan et al.* [1993, 1994].

The results of this study illustrate that day-to-day variations in $F_{10.7}$ do not correlate well with day-to-day changes in TEC. In particular, one day spikes in $F_{10.7}$ do not result in spikes in TEC. This is likely because spikes in solar radio flux are not well correlated with spikes in solar EUV radiation, the primary source of ionization in the F2 region of the ionosphere. This study further illustrates that a much better correlation between solar activity and observed TEC is obtained by using a 27 day running mean of $F_{10.7}$ rather than the daily value or shorter period (e.g., 5 day) running means. This smoothes out the individual spikes and results in better correlation between solar activity and observed TEC. This result is important in the development of an improved GPS single frequency correction algorithm.

As part of this study, we have continued to access and analyze dual frequency GPS measurements from the GPS International GPS Geodynamics Service for (IGS) maintained by the Jet Propulsion Laboratory. As of the end of this year, we have completed data processing for the data recorded through August 1996 at four different geographic locations. In addition, the GPS measurements made at Goldstone CA from December 90 through June 96 have been utilized to estimate the potential errors made with the current GPS single frequency algorithm.

Unfortunately, there is a significant gap in the data from September 91 through July 92. This gap limits our attempts to quantify the potential errors of the current single frequency algorithm during solar maximum. Figure 29 illustrates the results of the Goldstone analysis. In the top three figures, daily values of 10.7 cm solar flux are plotted versus dual-frequency GPS measurements made at 1400 hours local time for each of three seasons, winter (November, December, January and February), equinox (March, April, September and October) and summer (May, June, July and August). The bottom three figures illustrate the corresponding predictions of ionospheric behavior for the Goldstone site from the current single-frequency ionospheric correction algorithm. In comparing the measured data with the algorithm predictions, one notes a similar linear trend up to an $F_{10.7}$ value of approximately 210. At that point, the ionospheric correction algorithm underestimates the measured data. Much of this apparent saturation effect is caused by the strong one day-peaks in $F_{10.7}$.

3.2. Absolute Real-Time Ionospheric Measurements from GPS Satellites in the Presence of Anti-Spoofing

GPS satellites transmit coherent radio signals at two frequencies, L1 at 1.575 GHz and L2 at 1.227 GHz. These carriers are phase-modulated with two types of code, coarse acquisition (C/A) on L1 and precise code (P-code) on L1 and L2. The P codes are used to determine the group delay measurements. Absolute measurements of the ionospheric range delay can be obtained by differencing the group delay from both frequencies. On 31 January 1994, anti-spoofing (a/s) was turned on for most block II GPS satellites. When a/s is turned on the precision code (P-code) is encrypted and replaced by an unknown Y-code. Only military receivers equipped with an authorized key can use the Y-code directly. In this study, we have accessed dual-frequency GPS data recorded with GPS Rogue and Turborogue receivers designed by Allen Osborne Associates, Inc.. When a/s is activated, these receivers continue to provide group delay and carrier phase measurements in a codeless mode by cross correlating the L1 and L2 signal. Because of the degraded signal-to-noise ratio obtained by the receiver when the satellites are in a/s mode, there is a significantly higher level of system noise, particularly at low-elevation angles. This increased noise can seriously affect many of the real-time applications for GPS that require high precision and accuracy, such as the precision aircraft approaches in the FAA's Wide Area Augmentation System (WAAS).

The purpose of this research was to illustrate the limitations to which ionospheric range delay can be measured in real-time under both a/s on and off conditions. This was carried out by testing various filter techniques on real-time dual frequency GPS data recorded at several sites under a/s on and off conditions. A summary of the results is given in the abstract of Gendron et al. included in Section 5, Presentations and Proceedings.

3.3. Total Electron Content of the Earth's Protonosphere

Continuous measurements of the protonospheric contribution to TEC from the ATS-6 satellite were made from a number of stations covering middle and near-equatorial latitude regions from July 1974 through December 1978, a period of low to moderate solar activity. These ATS-6 measurements are unique in that they afforded the only opportunity to continuously monitor TEC using both the Faraday rotation and the differential group delay technique of radio waves from

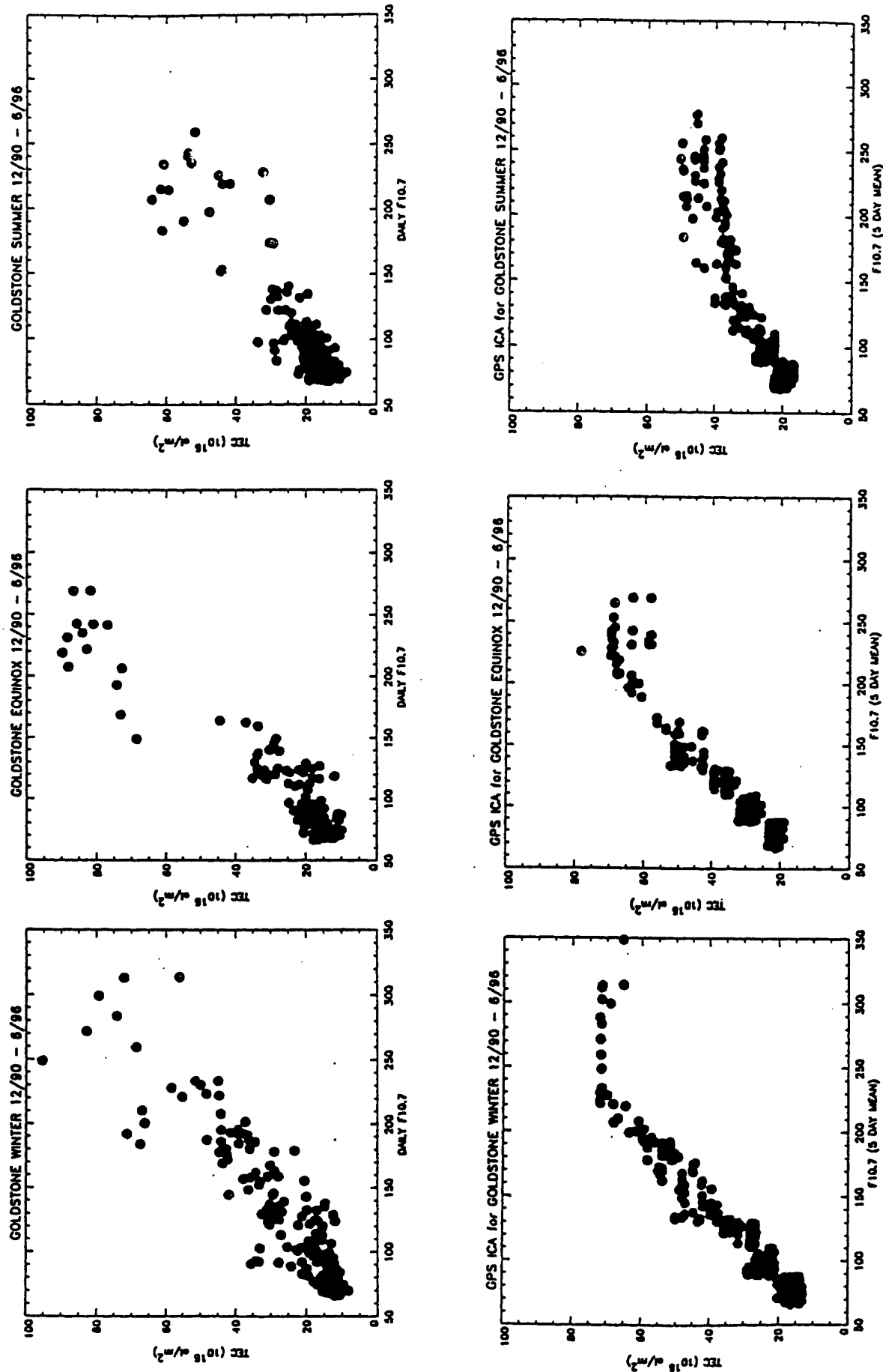


FIGURE 29. (top) Daily Values of 10.7 cm Solar Flux vs Dual-Frequency GPS Measurements 1400 LT
 (bottom) Predictions of Ionospheric Behavior from Current Single-Frequency Ionospheric Correction Algorithm

the same satellite. This combination of methods allowed the measurement of the contribution of TEC from the earth's protonosphere, that region extending from approximately 2,000 km altitude to the height of the geostationary ATS-6 satellite at 35,800 km. These measurements form the major source of our knowledge of the geographic and temporal variations in the contribution to TEC from the earth's protonosphere. In this quarter, a study was initiated to compare the available protonospheric electron content observations from a few representative stations with a model of the earth's protonosphere. The model will then be used to infer the protonospheric electron content contribution to TEC measured by the currently used technique of differential group delay from the dual-frequency transmissions from the GPS satellites.

Initial steps of this research included a review of some of the more important results of the ATS-6 experiment and some additional data processing and analysis of the measurements recorded at Palehua, Hawaii. Monthly averages of TEC and protonospheric electron content (N_p) from September 1977 through December 1978 are shown in Figure 30. In winter, the protonospheric content N_p is essentially constant throughout the day and night. In summer, there are daytime maxima in the early afternoon (1400 LT). In Figure 31, the ratio of N_p to TEC changes markedly with local time with a minimum of about 10 percent in the early afternoon and a distinct maximum (between 50 percent and 90 percent) near 0500 LT in all months.

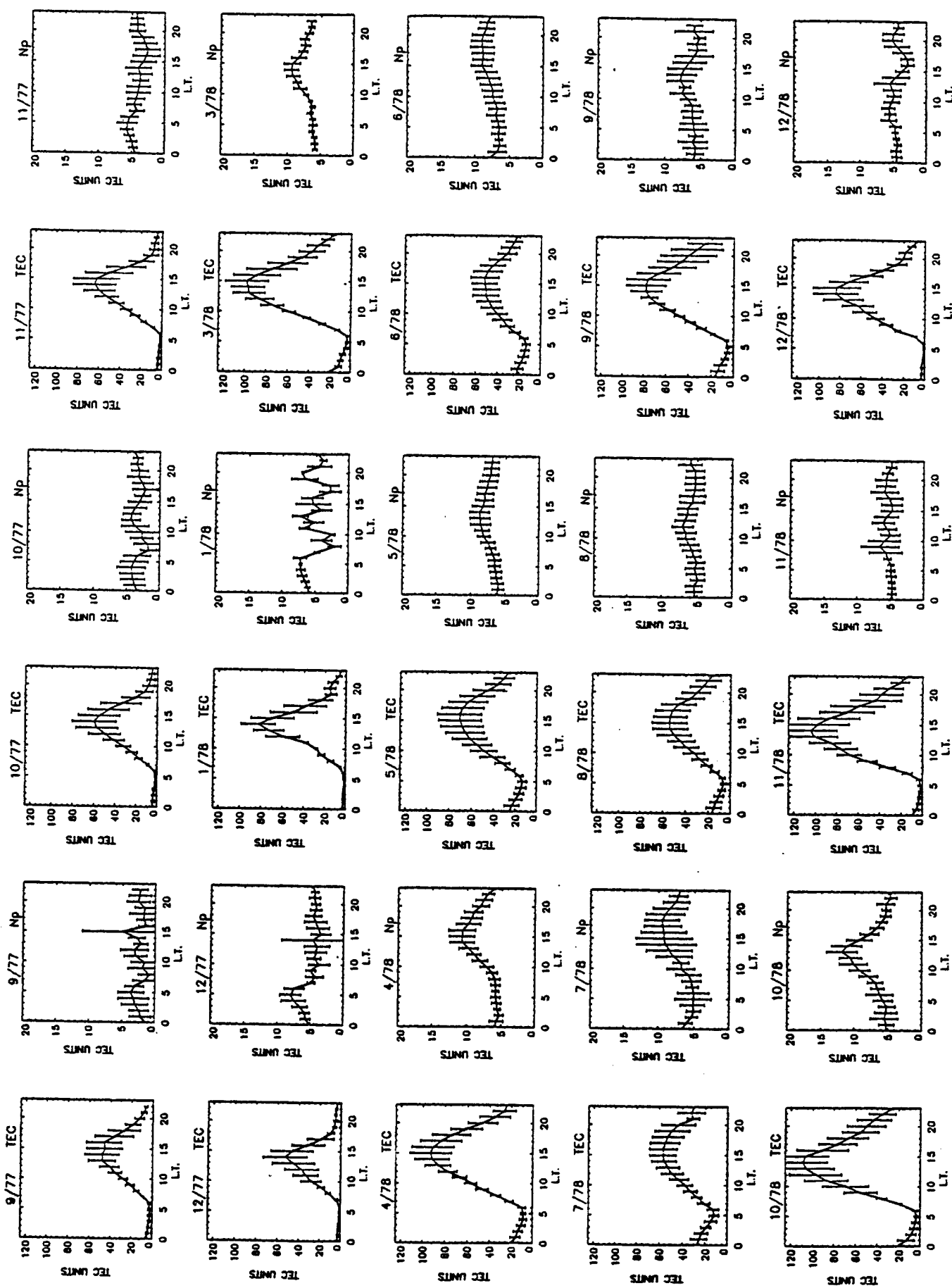
3.4. Instrumental Bias in GPS Measurements

Line-of-sight ionospheric measurements derived from differencing dual-frequency GPS range data are corrupted by instrumental biases in both the receiver and GPS satellite transmitters. The instrumental bias is the difference of the two dispersive delays introduced by the analog hardware in the L1 and L2 signal paths. These instrumental biases have continued to be a major concern for ionospheric research using GPS. Since it is highly desirable to be able to make measurements of TEC from GPS to an absolute accuracy of 1 TEC unit, (10^{16} el/m^2), it is important to be able to estimate the satellite and receiver biases with a very high degree of accuracy.

Several research groups have reported satellite and receiver bias values derived from various estimation strategies. *Wilson and Mannucci* [1994] have evolved a technique that takes advantage of a global network of more than 50 dual-frequency stations. *Sardon et al.* [1994] have developed a technique that uses a local network of stations and generates results consistent with *Wilson and Mannucci* [1994]. These studies have illustrated that the satellite biases have magnitudes of +/- 5 nanoseconds (ns) of differential delay (1 ns of differential delay at L band = 2.85 TEC units) and remain constant over a fairly long period of time. These studies have also generated receiver biases for a number of stations. Receiver biases have been shown to be as large as 20 ns (nearly 60 TEC units).

In our research activities using GPS, we have frequently applied the satellite and receiver biases provided by the Jet Propulsion Laboratory (JPL) and described in *Wilson and Mannucci* [1994]. Our experience has shown that the satellite biases are consistent and dependable. The receiver biases, however, are not reliable. This is due to the fact the any change in the receiver, pre-amp, cabling and antenna position or configuration has a significant effect on the overall receiver bias value. Unfortunately, JPL calculates receiver biases only on an occasional basis and they are not reported in the data base. As a result, the ionospheric researcher is often faced with *guessing* at the receiver bias.

FIGURE 30. Monthly Averages of TEC and Protonospheric Electron Content Sept 77 – Dec 78



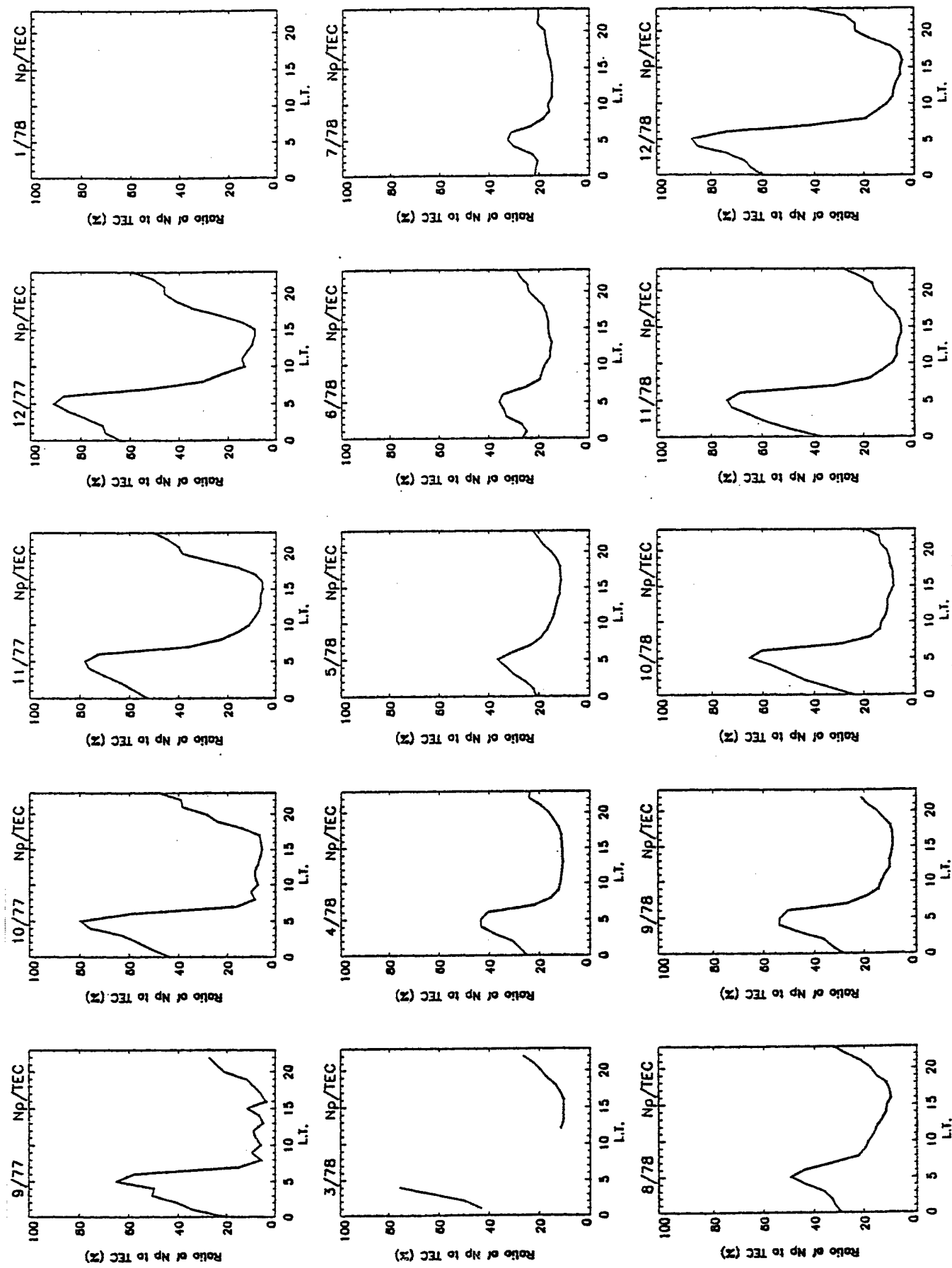


FIGURE 31. Ratio of Protonospheric Electron Content to TEC

We have attempted to validate a new technique that provides estimates of combined satellite and receiver biases at individual locations. The Self-Calibration of Pseudorange Errors (SCORE) [Bishop *et al.*, 1996] concept uses a self-consistency constraint on the receiver's own measurements of ionospheric delay to derive the sum of the receiver system and pseudorange error for each satellite. The self-consistency concept of SCORE is defined as a constraint that the ionosphere changes only moderately over space and time. Thus, two different satellites should exhibit a common TEC induced range delay if their ray paths intersect the ionosphere at "near space-time." Other differences should then be attributed to the receiver and satellite hardware biases. SCORE quantifies "near space time" in a weighted least squares approach, where divergence in TEC measurements are down-weighted according to their space-time separation. The advantages that this method has over those previously described is that it requires data from only one site and it is faster computationally. If sufficiently correct, this method may enable the ionospheric researcher to make single site ionospheric measurements at high levels of accuracy.

The approach of this initial validation study was to apply the SCORE algorithm to dual-frequency GPS measurements collected at various mid-and low-latitude locations for a series of geomagnetically quiet days. The results were then compared for validity and consistency. The data used in this study was recorded from 16 to 20 September 1995 at the following six locations:

Westford, MA	42.42°N	71.49°W
Bermuda	32.30°N	64.70°W
Richmond, FL	25.46°N	80.38°W
Bogota, Columbia	4.61°N	74.08°W
Arequipa, Peru	16.36°S	71.49°W
Santiago, Chile	32.97°S	70.67°W

These sites were selected because they span a wide latitudinal range over the American Sector. In particular, the near equatorial sites should exhibit extreme gradients in the ionosphere and will represent a worst case scenario for SCORE. Figure 32 summarizes the results of the study. In this figure, the combined satellite and receiver biases derived with SCORE over the 5-day period together with their standard deviations are plotted on the y-axis for each of the six recording stations. Note that the biases have been normalized to zero to enable a visual comparison between the individual stations. In this figure, the results exhibit a similar pattern at the three mid-latitude stations at Westford, Bermuda and Richmond. The Westford station illustrates the most consistent results with very small deviations from the mean. The Bermuda and Richmond plots show larger standard deviations, although they are still less than 3 TEC units (approximately 1 meter). Results for the near equatorial location at Bogota exhibit very large error bars and the pattern seems different than the one seen at the mid-latitude stations. Results at Arequipa are slightly better than those at Bogota but the error bars are still as large as 9 or 10 TEC units (nearly 3 meters). At Santiago, the standard deviations are smaller but there are large discrepancies in the magnitude of some of the biases with those illustrated in the northern mid-latitude sector.

Figures 33 and 34 show data analysis results when the SCORE biases that are represented in Figure 32 are utilized. In general, if the satellite and receiver bias calculations are correct, a reasonable diurnal plot of TEC will be obtained with high elevation measurements. In Figure 33,

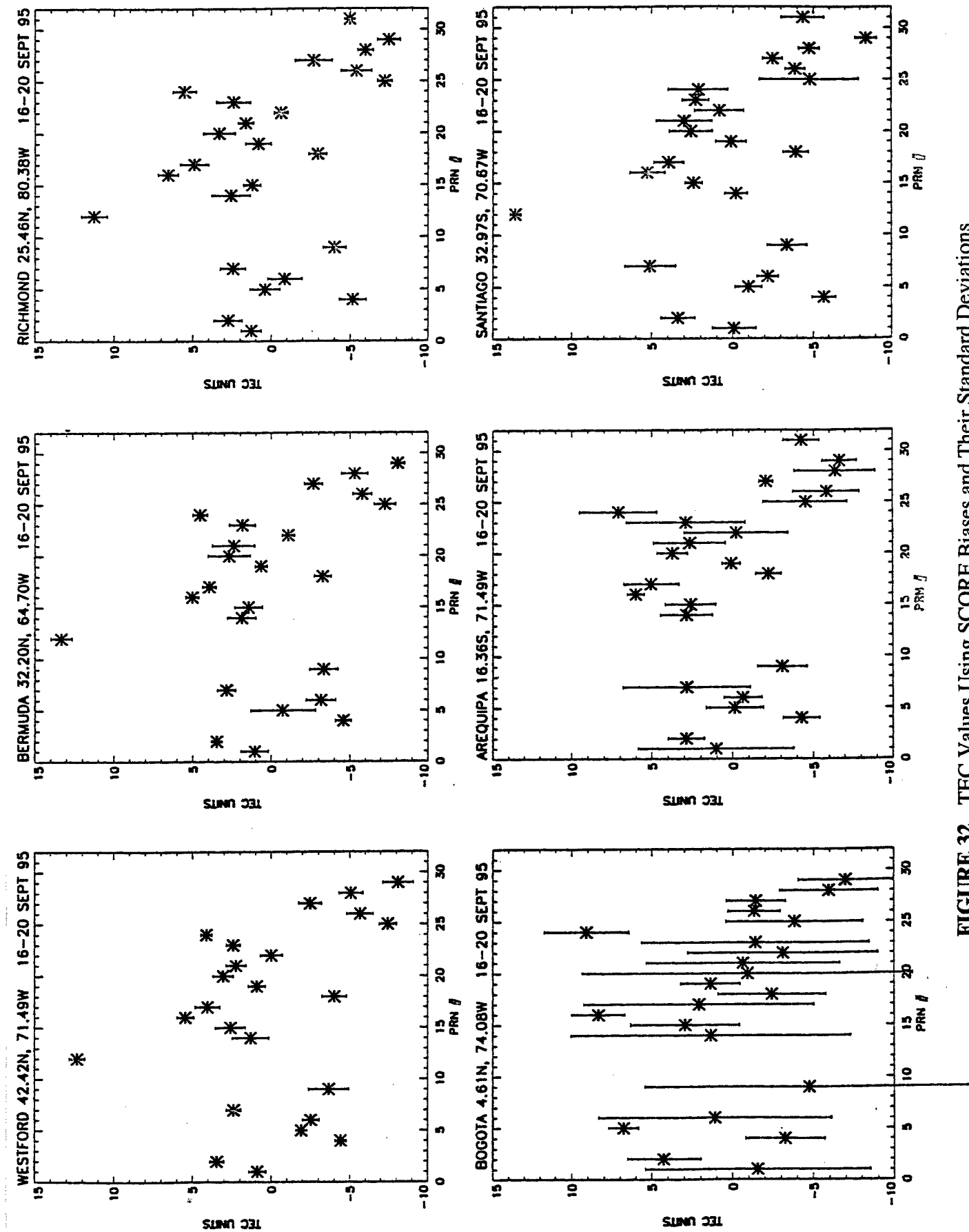


FIGURE 32. TEC Values Using SCORE Biases and Their Standard Deviations

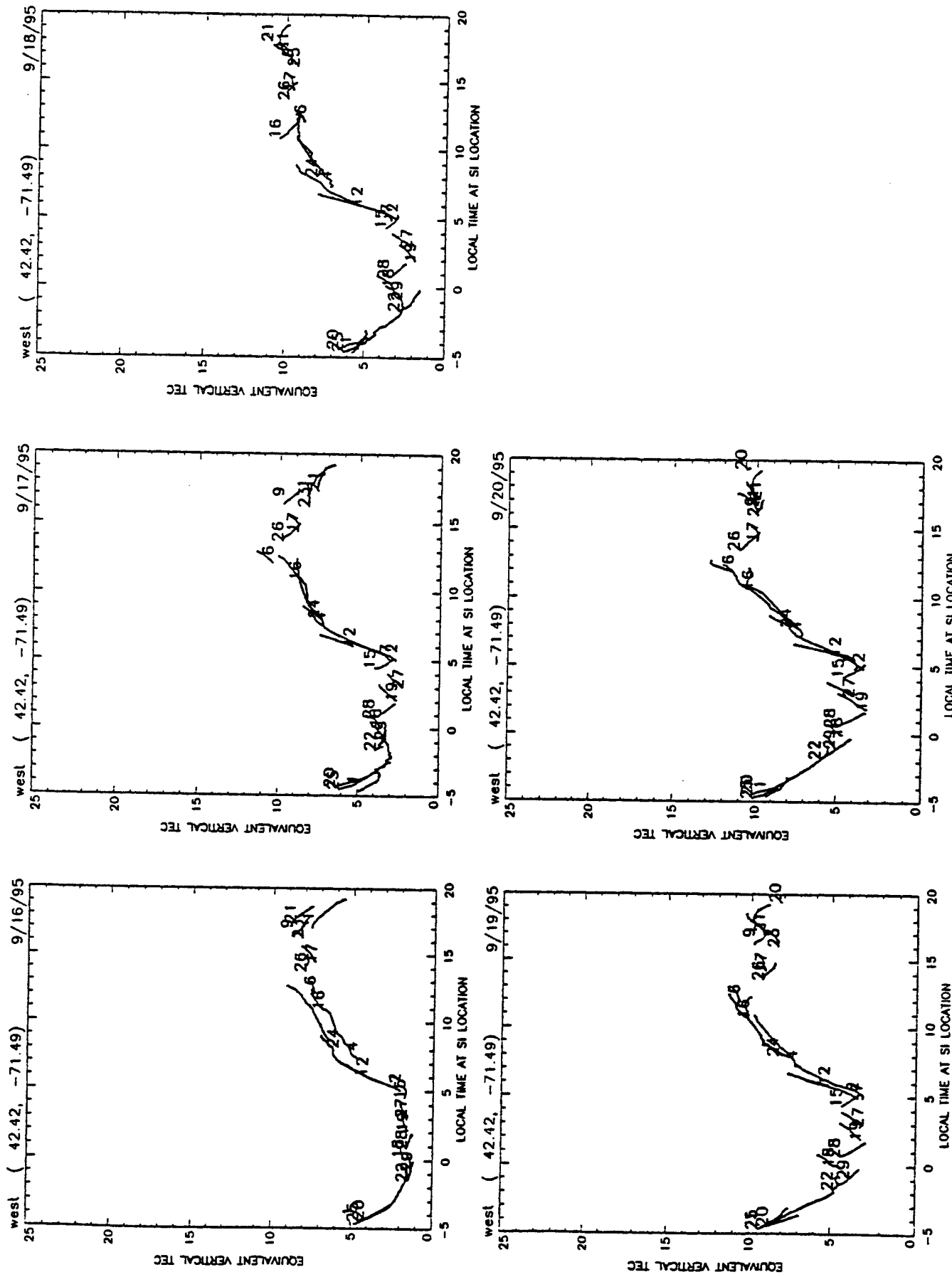


FIGURE 33. Westford High Elevation Tec Data Using SCORE Biases

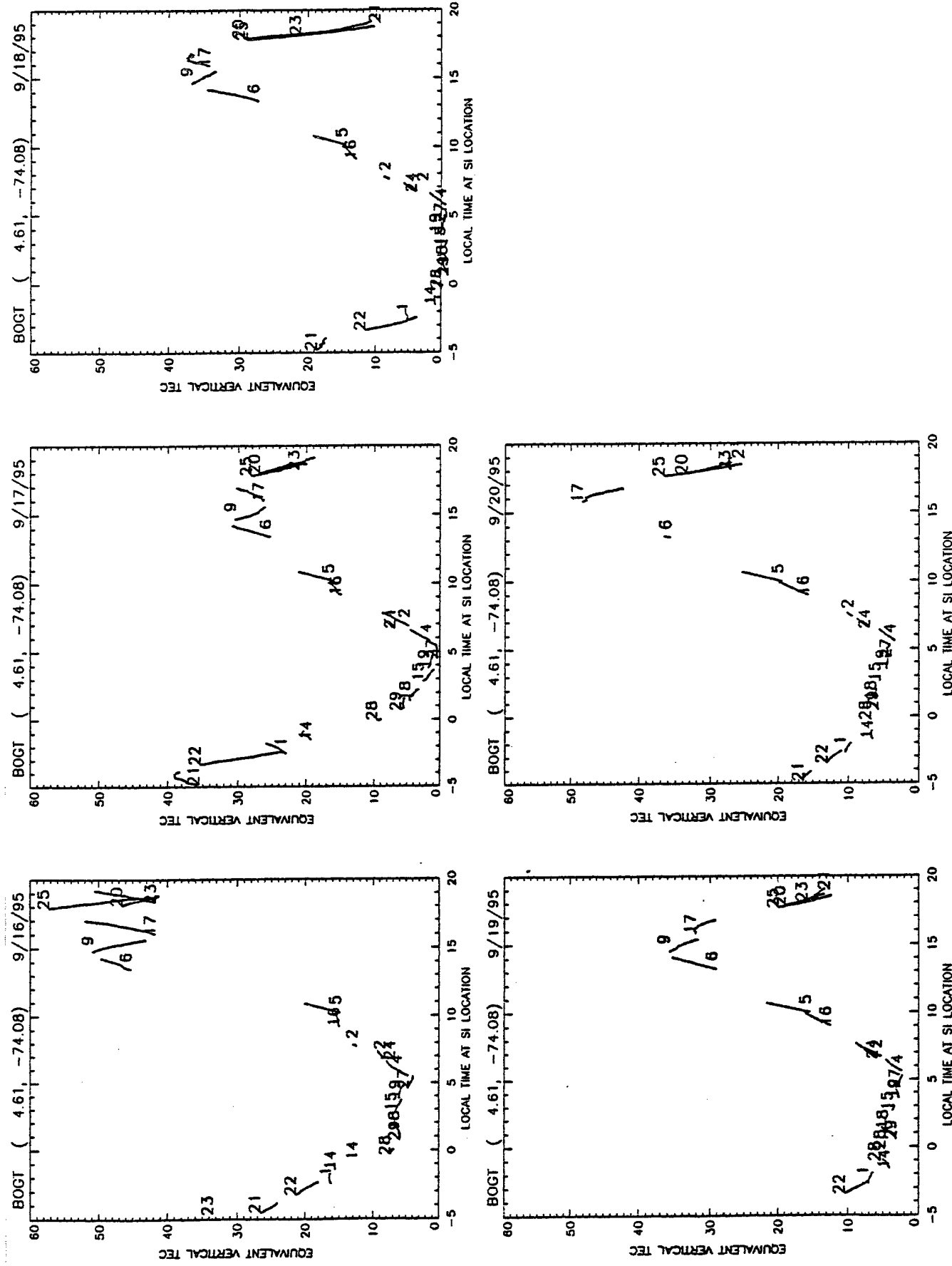


FIGURE 34. Ionospheric Effects At Bogota

high elevation data recorded at Westford over the 5-day period is plotted using the SCORE biases. Note that a reasonable diurnal curve is achieved on all five days. Similar figures were obtained with the Bermuda and Richmond data. Figure 34 illustrates the data analysis results at Bogota. This station is situated near the equatorial anomaly region, a region characterized by the highest values of TEC and peak electron density in the worldwide ionosphere. In addition, the day-to-day variability of the near-equatorial ionosphere can be very large, due to changes in the strength of the $\mathbf{E} \times \mathbf{B}$ drift at the magnetic equator and from the differences in the day-to-day strength of the meridional and zonal wind component. The results shown in Figure 34 reflect these ionospheric effects at Bogota. Although reasonable diurnal curves for Bogota are achieved with the SCORE calculations, the negative TEC values shown on 9/18/95 indicate that there are errors in the overall magnitude of the biases.

The results illustrated in these figures indicate that SCORE provides excellent estimation of the combined satellite and receiver biases at mid-latitude locations. Calculations at low-latitude locations, however, are still questionable. Bishop (1996) suggests that some of the problems with the SCORE calculations at the Bogota and Arequipa sites may be related to the large ionospheric gradients in the equatorial region but the major problems are more likely due to the fact the many of the measurements at these sites were not continuous. He also suggested that the large day-to-day deviations in the combined biases could be related to different satellite coverage and multi-path errors at the individual stations. In order to affirm the performance of SCORE in the low-latitude region, it is necessary to continue this study with additional measurements and to compare the results with calculations from other bias estimation algorithms.

3.5. Statistics of the Spatial and Temporal Variations in Ionospheric Range Delay

Work has been initiated to observe the spatial and temporal variations in ionospheric range delay. This study will be based on dual-frequency GPS measurements recorded from 1993 through early 1997 by the IGS network, managed by the JPL. GPS measurements provide the unique opportunity to observe simultaneous ionospheric estimates in up to eight different slant paths from a single receiver. These measurements can imply the spatial variations viewed from one location. In addition, the temporal variation in range delay at a single location can be made by determining the rate of change in the ionospheric as measured with the highest elevation satellite at particular times of day.

This analysis is intended to provide a characterization of the ionospheric variations that will be encountered in the Federal Aviation Administration's (FAA) operational WAAS. The WAAS system is expected to experience the most problems during periods of ionospheric scintillation and during periods of major geomagnetic storms activity when the spatial and temporal gradients in the ionosphere can be higher than usual. This study is to be performed to quantify the magnitude and frequency of these large spatial and temporal gradients.

To date, we have obtained and processed GPS data for March, June and September of 1993 and for January and March of 1994 at the following sites:

Westford, Massachusetts
Goldstone, California
Albert Head, British Columbia

Fairbanks, Alaska
Kokee, Hawaii.

Data analysis and statistical routines are continuing into the next year.

3.6. Airglow Data

Programs for the SUN workstation were modified to accept the new version of the AURIC Code (version 46) that was received. Considerable time was spent in examining the AURIC 46 code in anticipation of using it to analyze STS-4, ST4-39, and Polar Bear airglow data. We have also examined programs that were written for analysis of Polar Bear data by Bob Rosenberg and students at Tel Aviv University, such as converting the raw data to images, filtering the data, roll adjustment, superimposing the landmass on the images, and showing the data in the corrected geomagnetic coordinate system.

We started work on analyzing data from the STS-4 flight. Programs for plotting tangent altitude data and spectral data obtained on the STS-4 flight were examined and modified as needed. We were then in a position to plot all the STS-4 data. Programs for obtaining tangent altitude models using AURIC for the same parameter as the data such as solar zenith angle, latitude, longitude, $F_{10.7}$, etc. were examined. Several of these models were then plotted and compared with the data plots. In some cases, the data and models agree very well, in others only fair. Only a few such comparisons have been made. It is planned to make the comparisons for all the STS-4 tangent altitude data.

In order to analyze the data obtained on STS-39, we also needed the ephemeris data for this flight. With the cooperation of Paul Pruneau of Boston College, we obtained the following parameters: time of flight (month, day, year, hour, minute, second), latitude, longitude, solar zenith angle, pitch, roll, and yaw. We have written programs to show the pertinent parameters on the graphs depicting the intensities of the radiations measured. Using these parameters, models using AURIC were prepared. In doing this, averaging of spectra up to 45, was accomplished. A comparison of the models with the data examined so far, in the wavelength range of 1100 to 1700 Angstroms, showed good results with the one exception being the comparison at Lyman alpha.

3.7. Signature of Equatorial Scintillation Onset in Near-Sunset DMSP Satellite Data

During this year, we worked on a study of ion density data from the DMSP SSIES sensor. Previous work has shown that the overall shape of latitude profiles of total ion density can be related to the strength of the ionospheric eastward electric field, and to the strength and direction of the meridional neutral wind. Since the occurrence of equatorial spread-F (a source of equatorial radio signal scintillation) is dependent on both of these physical parameters it should be possible to correlate them with the occurrence of spread-F. A comparison of ground-observed scintillation data from a receiver on Ascension Island (346° E) with corresponding DMSP passes from 1989 shows that days when spread-F did occur match up well with days when DMSP latitude profiles of ion density showed signatures of strong ionospheric electric fields and weak

neutral winds. Further work in this study will compare scintillation occurrence with DMSP satellite parameters for other longitudes and for different times in the solar activity cycle.

4. REFERENCES

- Abdu, M.A., I.S. Batista, and J.R. de Souza, An overview of IRI-observational data comparison in American (Brazilian) sector low latitude ionosphere, *Adv. Space Res.*, 18 (6), 13-22, 1996.
- Anderson, D.N., M. Mendillo, and B. Herniter, A semi-empirical low-latitude ionospheric model, *Radio Sci.*, 22, 292-306, 1987.
- Anderson, D.N., J.M. Forbes, and M. Codrescu, A fully analytical, low- and middle-latitude ionospheric model, *J. Geophys. Res.*, 94, 1520-1524, 1989.
- Balan, N., G.J. Bailey, and B. Jayachandran, Ionospheric evidence for a nonlinear relationship between the solar e.u.v. and 10.7 cm fluxes during an intense solar cycle, *Planet. Space Sci.*, 41, 141-145, 1993.
- Balan, N., G.J. Bailey, B. Jenkins, P.B. Rao, and R.J. Moffett, Variations of ionospheric ionization and related solar fluxes during an intense solar cycle, *J. Geophys. Res.*, 99, 2243-2253, 1994
- Bilitza, D., Electron density in the equatorial topside, *Adv. Space Res.*, 5 (10), 15-19, 1985.
- Bilitza, D., International reference ionosphere 1990, NSSDC/WDC-A-R&S Report 90-22, Goddard Space Flight Center, Greenbelt, Maryland, 1990.
- Bilitza, D. and K. Rawer, New options for IRI electron density in the middle ionosphere, *Adv. Space Res.*, 10(11), 7-16, 1990.
- Bilitza, D., C. Koblinsky, S. Kia, R. Williamson, and B. Beckley, The equatorial anomaly region as seen by the TOPEX/POSEIDON satellite, *Adv. Space Res.*, 18(6), 23-32, 1996.
- Bilitza, D., K. Rawer, L. Bossy, and T. Gulyaeva, International reference ionosphere - past, present, and future: I. Electron density, *Adv. Space Res.*, 13 (3), 3-13, 1993.
- Bilitza, D., K. Rawer, S. Pallaschke, C.M. Rush, N. Matuura, and W.R. Hoegy, Progress in modeling the ionospheric peak and topside electron density, *Adv. Space Res.*, 7 (6), 5-12, 1987.
- Bishop, G. private communication, 1996.
- Bishop, G., A. Mazzella, E. Holland, and S. Rao, Algorithms that Use the Ionosphere to Control GPS Errors, Proceedings of IEEE 1996 Position Location and Navigation Symposium (PLANS), Atlanta GA, April 1996.
- Creamer, A.P., Equatorial F-region electron densities over a solar cycle: Comparisons between observations and numerical models, M.S. thesis, 201pp., Utah State University, 1992.

- Daniell, Jr., R.E., L.D. Brown, D.N. Anderson, M.W. Fox, P.H. Doherty, D.T. Decker, J.J. Sojka, and R.W. Schunk, Parameterized ionospheric model: A global ionospheric parameterization based on first principles models, *Radio Sci.*, 30, 1499-1510, 1995.
- Fejer, B.G., E.R. de Paula, R.A. Heelis, and W.B. Hanson, Global equatorial ionospheric vertical plasma drifts measured by the AE-E satellite, *J. Geophys. Res.*, 100, 5769-5776, 1995.
- Fox, M.W. and L.F. McNamara, Improved world-wide maps of monthly median f_oF_2 , *J. Atmos. Terr. Phys.*, 50, 1077-1086, 1988.
- Gulyaeva, T.L., Progress in ionospheric informatics based on electron-density profile analysis of ionograms, *Adv. Space Res.*, 7 (6), 39-48, 1987.
- Gulyaeva, T.L., K.K. Mahajan, and N.K. Sethi, Modification of IRI half-density height option for low latitudes, *Adv. Space Res.*, 18 (6), 149-152, 1996.
- Hajj, G.A., R. Ibanez-Meier, E.R. Kursinski, and L.J. Romans, Imaging the ionosphere with the global positioning system", *International Journal of Imaging Systems and Technology*, 5, 174-184, 1994.
- Llewellyn, S.K. and R.B. Bent, Documentation and description of the Bent ionospheric model, Air Force Geophysics Laboratory, *Report AFCRL-TR-73-0657*, Hanscom AFB, Massachusetts, 1973.
- Mahajan, K.K., R. Kohli, N.K. Sethi, and V.K. Pandey, Variability of the F-region parameter $h_{0.5}$, *Adv. Space Res.*, 15 (2), 51-60, 1995.
- Preble, A.J., D.N. Anderson, B.G. Fejer, and P.H. Doherty, Comparison between calculated and observed F region electron density profiles at Jicamarca, Peru, *Radio Sci.*, 29, 857-866, 1994.
- Rawer, K., Ionospheric mapping in the polar and equatorial zones, *Adv. Space Res.*, 16 (1), 9-12, 1995.
- Reinisch, B.W. and Xueqin Huang, Low latitude digisonde measurements and comparison with IRI, *Adv. Space Res.*, 18 (6), 5-12, 1996.
- Rush, C.M., M. PoKempner, D. Anderson, F.G. Stewart, and J. Perry, Improving ionospheric maps using theoretically derived values of f_oF_2 , *Radio Sci.*, 18, 95-107, 1983.
- Rush, C.M., M. PoKempner, D. Anderson, J. Perry, F.G. Stewart, and R. Reasoner, Maps of f_oF_2 derived from observations and theoretical data, *Radio Sci.*, 19, 1083, 1984.
- Sardon, E., A. Ruis, and N. Zarraoa, Estimation of the transmitter and receiver differential biases and the ionospheric TEC from GPS observations, *Radio Sci.*, 29(3), 577-586, 1994.

Su, Y.Z., K.-I. Oyama, G.J. Bailey, S. Fukao, T. Takahashi, and H. Oya, Longitudinal variations of the topside ionosphere at low latitudes: Satellite measurements and mathematical modelings, *J. Geophys. Res.*, 101, 17191-17205, 1996.

Szusczewicz, E.P., D. Torr, P. Wilkinson, P. Richards, R. Roble, B. Emery, G. Lu, M. Abdu, D. Evans, R. Hanbaba, K. Igarashi, P. Jiao, M. Lester, S. Pulinet, B.M. Reddy, P. Blanchard, K. Miller, and J. Joselyn, F region climatology during the SUNDIAL/ATLAS 1 campaign of March 1992: Model-measurement comparisons and cause-effect relationships, *J. Geophys. Res.*, 101, 26741-26758, 1996.

Walker, G.O., Longitudinal structure of the F-region equatorial anomaly - a review, *J. Atmos. Terr. Phys.*, 43, 763-774, 1981.

West, K.H., R.A. Heelis, and F.J. Rich, Solar activity variations in the composition of the low-latitude topside ionosphere, *J. Geophys. Res.*, 102, 295-305, 1997.

Wilson, B. and A. Mannucci, Extracting ionospheric measurements from GPS in the presence of anti-spoofing, *Proceedings of ION GPS-94*, The Institute of Navigation, Washington DC, September, 1994.

5. PRESENTATIONS AND PROCEEDINGS

We were involved in 15 presentations at various scientific meetings of which 7 appeared in published proceedings. There are also 4 presentations that have been submitted to meetings that are to be held in the summer of 1997.

- B. Basu, D.T. Decker, and J.R. Jasperse, "Incident Proton Spectra: Ionospheric Effects of High Energy Power Law Tails", presented at the Ionospheric Effects Symposium held in Alexandria, VA in May, 1996. It also appeared in *1996 Ionospheric Effects Symposium*, 340-345, 1996.

Abstract

Studies of ion populations in the central plasma sheet (CPS) [Christon *et al.*, 1988, 1989, 1991] have found that at high energies ($E >$ characteristic or peak energy) there is a nonthermal power law tail which can be fitted using a kappa distribution. While similar studies for ionospheric altitudes are fewer in number, Lyons and Evans [1984] combined data from various instruments to show that proton distributions at ionospheric altitudes have high-energy tails and are the same as those seen for earthward-streaming protons in the outer boundary of the plasma sheet. More recently, the Particle Environment Monitor (PEM) experiment on board the Upper Atmosphere Research Satellite (UARS) [Sharber *et al.*, 1993] has observed ionospheric ion spectra with a high-energy power law tail similar to that described by Christon *et al.* [1991] as typical of CPS ion populations. However, previous theoretical calculations of proton-hydrogen atom transport have generally assumed a Maxwellian distribution for the incident proton spectra [Strickland *et al.*, 1993]. In this paper, we present the impact that high-energy power law tails have on calculations of the ionospheric effects of precipitating protons.

Christon, S.P., D.G. Mitchell, D.J. Williams, L.A. Frank, C.Y. Huang, and T.E. Eastman, Energy spectra of plasma sheet ions and electrons from ~ 50 eV/e to ~ 1 MeV during plasma temperature transitions, *J. Geophys. Res.*, 93, 2562, 1988.

Christon, S.P., D.J. Williams, D.G. Mitchell, L.A. Frank, and C.Y. Huang, Spectral characteristics of plasma sheet ion and electron populations during undisturbed geomagnetic conditions, *J. Geophys. Res.*, 94, 13409, 1989.

Christon, S.P., D.J. Williams, D.G. Mitchell, C.Y. Huang, and L.A. Frank, Spectral characteristics of plasma sheet ion and electron populations during disturbed geomagnetic conditions, *J. Geophys. Res.*, 96, 1, 1991.

Lyons, L.R. and D.S. Evans, An association between discrete aurora and energetic particle boundaries, *J. Geophys. Res.*, 89, 2395, 1984.

Sharber, J.R., R.A. Frahm, J.D. Winningham, J.C. Biard, D. Lummerzheim, M.H. Rees, D.L. Chenette, E.E. Gaines, R.W. Nightingale, and W.L. Imhof, Observations of the UARS particle environment monitor and computation of ionization rates in the middle and upper atmosphere during a geomagnetic storm, *Geophys. Res. Lett.*, 20, 1319, 1993.

Strickland, D.J., R.E. Daniell, Jr., J.R. Jasperse, and B. Basu, Transport-theoretic model for the electron proton-hydrogen atom aurora: 2. Model results, *J. Geophys. Res.*, 98, 21533, 1993.

- P.H. Doherty, D.N. Anderson, J. Eicher and J.A. Klobuchar, "Total Electron Content Over the Pan American Longitudes: March-April 1994", presented at the Ionospheric Effects Symposium held in Alexandria, VA in May, 1996. It also appeared in *1996 Ionospheric Effects Symposium*, 441-449, 1996.

Abstract

An experimental campaign to measure diurnal changes in Total Electron Content (TEC), over the wide latitude range from approximately 50 degrees North to 40 degrees South was carried out from 28 March through 11 April 1994 by monitoring the differential carrier phase from the US Navy TRANSIT Navigation Satellites, using a chain of ground stations aligned along the approximate 70 degree west longitude meridian. This campaign was conducted primarily to study the day-to-day variability of the equatorial anomaly region. The experimental plan included using the received values of TEC from the chain of stations to construct profiles of electron density versus latitude using tomographic reconstruction techniques, and then, to compare these reconstructions against a theoretical model of the low-latitude ionosphere.

The diurnal changes in TEC along this latitude chain of stations showed a high degree of variability from day-to-day, especially during a magnetic storm which occurred near the beginning of the campaign. The equatorial anomaly in TEC, showed large changes in character in the two hemispheres, as well as differences in magnitude from day-to-day. The latitudinal gradients of TEC, especially in the lower mid-latitudes, also showed large differences between magnetic storm and quiet conditions. Comparisons of the TEC data with the theoretical model illustrate the sensitivity of the model calculations to changes in magnetic ExB drift, and serves to validate the strong dependence of these drifts of the formation and the strength of the equatorial anomaly regions.

- A.J. Preble, D.T. Decker, and D.N. Anderson, "Improving IRI90 Low Latitude Ionospheric Specification", presented at the Ionospheric Effects Symposium held in Alexandria, VA in May, 1996. It also appeared in *1996 Ionospheric Effects Symposium*, 243-251, 1996.

Abstract

At low latitudes, a number of comparisons between the IRI90 model of F-region electron density profiles with observed profiles measured by the Jicamarca incoherent scatter radar indicate that during the daytime, the observed profile shape is much broader in altitude than that specified by IRI90; while at night, just after sunset, observed Hmax values are significantly higher. This is especially true during periods of high solar activity. The theoretically-derived ionospheric parameters such as Hmax, Nmax and profile shape which are contained in the Parameterized Ionospheric Model (PIM) have been shown to be in better agreement with Jicamarca observations. This paper describes an attempt to improve IRI90 at low latitudes by calculating three ionospheric parameters, the profile half thickness, Nmax, and Hmax from PIM as a function of latitude, longitude, and solar local time for a variety of solar cycle, seasonal and geomagnetic conditions. The generation of electron density profiles using these three parameters will be presented as well as a description of how these expressions might be implemented into the IRI90 model. Finally, we discuss the degree of improvement which has been achieved by comparing these profile parameters with a number of ionospheric observations not only at the magnetic equator but also at higher magnetic latitudes near the crests of the equatorial anomaly.

- P.J. Sultan, "Satellite Signatures of the Global Occurrence Morphology of Equatorial Spread-F", presented at the Ionospheric Effects Symposium held in Alexandria, VA in May, 1996. It also appeared in *1996 Ionospheric Effects Symposium*, 287-292, 1996.

- P.J. Gendron, P.H. Doherty, and J.A. Klobuchar, "Absolute Real-Time Ionospheric Measurements from GPS Satellites in the Presence of Anti-Spoofing", presented at the ION-GPS 52nd Annual Meeting held in Cambridge, MA in June 1996. It also appeared in the *Proceedings of the ION 52nd Annual Meeting*, 547-556, 1996.

Abstract

Determining user position and velocity using signals from the constellation of GPS satellites depends upon receiving signals from satellites in widely disparate directions in the sky to minimize the effects of geometric dilution of precision (GDOP). The range error due to the electron content of the earth's ionosphere is normally corrected by using signals of both the GPS L2 and L1 frequencies to automatically correct for the first order ionospheric range error effect. When a GPS satellite is just rising above the horizon it is desirable to use it in the navigation solution, as soon as it reaches an elevation above, say 5° , so that the newly acquired satellite aids in producing a position solution with a minimum GDOP. However, the lower signal-to-noise ratio when a GPS satellite is viewed near the horizon, especially evident when anti-spoofing (a/s) is turned on, can limit the accuracy of making measurements of *absolute* ionospheric range delay to values higher than approximately one meter until the satellite reaches an elevation angle greater than approximately 30° .

The comparative effects of a/s and high multi-path on the GPS differential group delay signal have been examined and the results clearly demonstrate that even in a high multi-path environment, a/s is the dominant effect which limits early determination of absolute ionospheric range error. A novel, non-recursive, robust residual-adaptive filter was found to give the best results in obtaining absolute ionospheric range error corrections at low elevation angles in the presence of a/s. The times required from satellite rise until an absolute ionospheric range error of less than 0.16 meters rms. could be obtained corresponded to elevation angles of approximately 30° in the presence of a/s, and considerably lower with a/s turned off. Multi-path was a significant limitation in determining absolute ionospheric range error only with a/s turned off, and then only in a relatively bad multi-path environment.

- J.A. Vladimer, V.R. Ewell, M.C. Lee, P.H. Doherty, D.T. Decker, and D.N. Anderson, "Ionospheric TEC Observations from the TOPEX Satellite", presented at the 23rd IEEE International Conference of Plasma Science in Boston, MA in June 1996 and the PRIMO session at the Cedar Workshop in Boulder, CO in June 1996.

Abstract

Variability of Total Electron Content (TEC) in the equatorial anomaly region of the ionosphere can be studied extensively using the results of measurements taken by the NASA/CNES satellite, TOPEX/Poseidon, which provides global ocean coverage (0 to 360° longitude, -66 to 66° latitude). The NASA Radar Altimeter (NRA) is the first space-borne dual-frequency altimeter capable of accurately measuring vertical ionospheric TEC below 1340 km. TOPEX TEC observations have already been used to support results from an ionospheric measurements campaign that was conducted in the equatorial region of South America by

Phillips Laboratory in the spring of 1994. The best agreement in TEC values is seen during intervals of longitudinal proximity of the satellites' paths.

Vertical measurements from TOPEX are obtained at a rate of one per second at 5.3 and 13.6 GHz along the same surface tracks every 10 days during which global ocean coverage is accomplished. TOPEX data records from 9/92 to 9/95 have been processed and reduced to one CDROM disc using one degree averaging over 110 km along the track for evaluation of the TEC measurements. Various plotting programs have been developed to display the observations. To facilitate further TEC studies, interface software has been prepared to provide identification of anomaly formation and structure. The TOPEX over-ocean data can be used as a supplement to land-based measurements in applications to ionospheric research at low and mid latitudes. This study focuses on comparisons between TOPEX vertical TEC data and GPS equivalent vertical TEC measurements taken near the east and west coastal regions of South America. Also, the Phillips Laboratory Global Parameterized Ionospheric Model (PIM) is utilized in an effort to estimate slant-to-vertical conversion errors.

- P.J. Sultan, "DMSP-Based Prediction of Equatorial Scintillation", presented at the Cedar Workshop held in Boulder, CO in June, 1996.
- P.H. Doherty, D.T. Decker, D.N. Anderson and B.D. Wilson, "Observed Ionospheric Dependence on Solar Activity: Implications for a New Single Frequency GPS User Algorithm", presented at the ION-GPS 96 Meeting held in Kansas City, MO in September, 1996. It also appeared in the *Proceedings of The 9th International Technical Meeting of The Satellite Division of the Institute of Navigation*, 1996.

Abstract

The ionosphere is the most substantial source of error in GPS positioning and navigation. Radio waves propagating through the ionosphere suffer an additional time delay as a result of their encounter with the total number of free electrons (TEC) along the path from the satellite to a ground station. The ionosphere is a highly variable and complex region that is a function of geographic location, local time, season, geomagnetic activity and solar activity. For the dual-frequency GPS user, the range error caused by the ionosphere is corrected for by using the signals of both the GPS L1 and L2 frequencies. For the single frequency user, the Ionospheric Correction Algorithm (ICA) was developed to correct for approximately 50 percent rms of the error. The ICA was developed in 1975 using the Bent Model [Llewellyn and Bent, 1973], a state-of-the-art empirical ionospheric model that was based on data recorded during an average solar cycle. Solar cycle maximum values since that period have been much higher. As a result, the ICA does not adequately represent periods of extremely high solar maximum activity.

The aim of this paper is to aid in the development of a new GPS single frequency user algorithm by defining an improved fit between long term solar activity and to determine if that fit changes for different seasons and geographic locations. This study is accomplished by correlating ionospheric measurements recorded at several widely spaced geographic locations over the last four solar cycles with various proxies of the 10.7 cm solar flux ($F_{10.7}$). Results are provided in a statistical format for geomagnetically quiet and disturbed conditions. The results of this study will be used in the development of new coefficients that describe worldwide ionospheric behavior. The improved Ionospheric Correction Algorithm will benefit all users of single-frequency GPS receivers.

- C.G. Stergis, "Instrumentation for UV and Visible Measurements Above Thunderstorms", presented at the annual meeting of the International Society for Optical Engineering held in Denver, CO in August, 1996. Also in *Proc. Intern. Soc. Optical Eng.*, Vol. 2831, Nov. 1996.
- D.T. Decker, C.E. Valladares, and D.N. Anderson, "Modeling F-Region Polar Cap Patches and Boundary Blobs", presented at the 31st COSPAR Scientific Assembly held in Birmingham, United Kingdom in July, 1996.

Abstract

Over the last 30 years, observations have shown that the high-latitude F-region contains a variety of mesoscale structures. In particular by the end of the 1980s, enough was known that a sequence of events could be described where various mesoscale structures evolved from one to another. The sequence begins at subauroral latitudes in the afternoon sector where a broad wedge of enhanced ionization is observed. At higher latitudes, this wedge thins in longitude to what is typically referred to as a tongue of ionization. Then by some process, that wasn't clearly defined but presumably took place near or within the cusp or throat, the tongue is structured into patches which then drift across the polar cap. The patches, in turn, are then reconfigured into boundary and subauroral blobs as the enhanced plasma convects out of the polar cap into the auroral zone. For the most part, this picture was built up from observations with little theoretical support from F-region modeling. However, over the last several years there have been significant successes in the modeling of both patches and blobs. We will discuss the theoretical approaches, simulations involving time-varying global convection, simulations involving meso-scale convection (plasma jet, vortices, flow channels, etc.), and future directions.

- D.N. Anderson, D.T. Decker, and P.H. Doherty, "Global Ionospheric Modeling of Geomagnetic Storms", presented at the 31st COSPAR Scientific Assembly held in Birmingham, United Kingdom in July, 1996.

Abstract

It is well established that the ionospheric impact of geomagnetic storms is global in nature; however, many past theoretical studies have focused on particular sub regions of the ionosphere. For example, we have previously used a low latitude ionospheric model to study the impact of storms on the low-latitude ionosphere. In particular, we used as input to the model the observed vertical drift velocities measured by the Jicamarca, Peru incoherent scatter radar facility during storms on 22,23 March 1990 and 13,14 June 1991. The resultant simulations produced dramatic changes in the electron density profiles that were consistent with DMSP in-situ electron density measurements. This same model has also been used in other studies that focused on specific storm effects in the low and mid-latitude ionosphere. However, in order to study the storm effects on a global scale, it would be useful to have a global model. In recent years, we have developed such a global theoretical ionospheric model (GTIM) and successfully used it to study problems at high, mid, and low latitudes. In this paper, we will review earlier low latitude work as well as discuss our initial simulations of the global ionospheric impact of geomagnetic storms.

In particular, we will focus on the uniqueness of individual storms and the difficulty of defining a typical or average storm.

- D.N. Anderson, D.T. Decker, and C.E. Valladares, "Modeling High Latitude F-region Mesoscale Structures", presented at the 25th General Assembly of URSI held in Lille, France from August 28 to September 5, 1996.

Abstract

Over the last 30 years, observations have shown that the high-latitude F-region contains a variety of mesoscale structures. In particular, it has been found that during periods of negative or southward directed B_z enhanced "patches" of ionization drift across the polar cap in an antisunward direction. These polar cap patches come in a wide variety of shapes and scale sizes. The typical sizes range from a few hundred to ~1000 km, and the enhancements of plasma densities can be up to an order of magnitude above the surrounding background. Over the years, there have naturally been a variety of suggestions as to how patches might be produced; however, identification of the precise mechanisms of patch creation has remained elusive.

By the end of the 1980s, enough was known that a "descriptive working model" could be constructed.^[1] This model described a sequence of events where various large scale structures evolved from one to another. The sequence begins at subauroral latitudes in the afternoon sector where a broad wedge of enhanced ionization is observed. At higher latitudes, this wedge thins in longitude to what is typically referred to as a tongue of ionization. Then, by some process that wasn't clearly defined, but presumably took place near or within the cusp or throat, the tongue is structured into patches which then drift across the polar cap. The patches, in turn, are then reconfigured into boundary and subauroral blobs as the enhanced plasma convects out of the polar cap into the auroral zone.

For the most part, this picture was built up from observations with some theoretical support from F-region modeling. But there were many gaps in the details, many uncertainties, and actually very few theoretical studies had explicitly focused on how F-region structure might be produced. However, over the last several years, modelers have successfully simulated the creation of high-latitude large scale plasma structure using two separate mechanisms (time-varying global convection and meso-scale events). Morphological predictions have been made that are currently being tested against data. A study at Sondrestrom has suggested that both mechanisms can be important and may very well operate together in a complex and intertwined manner. Simulations using time-dependent convection have also illustrated how patches can evolve into blobs in much the way predicted in the work of *Robinson et al.*^[2]. The purpose of this paper is to report on this recent progress in patch and blob modeling. We will discuss the theoretical approaches, simulations involving time-varying global convection, simulations involving meso-scale convection (plasma jet, vortices, flow channels, etc.), and future directions.

[1] R.T. Tsunoda, *Rev. Geophys.*, 26, 719, 1988.

[2] R.M. Robinson et al., *J. Geophys. Res.*, 90, 7533, 1985.

- D.T. Decker and D.N. Anderson, "Simulations of GPS/MET Ionospheric Observations", presented at the 25th General Assembly of URSI held in Lille, France from August 28 to

September 5, 1996. Also presented at the 1996 Fall AGU meeting held in San Francisco, CA in December, 1996.

Abstract

GPS/MET is a program using a low-earth orbiting satellite instrumented with a GPS receiver to perform limb soundings of the atmosphere using radio occultation of GPS satellites. The primary purpose of the program is to perform remote sensing of the troposphere and stratosphere. However, the limb-viewing geometry does provide a unique opportunity for ionospheric research. The useful measured quantity in this case is the Total Electron Content (TEC) between the low-earth-orbiting satellite and a particular GPS satellite. In contrast to ground based GPS measurements, the limb viewing geometry can provide the type of vertical information that is poorly measured by ground-based GPS measurements.

In this paper, the Global Theoretical Ionospheric Model (GTIM) is used to simulate the TEC as observed by both ground-based GPS receivers and GPS/MET. The model calculates the atomic oxygen ion density as a function of altitude, latitude, and local time. It includes the effects of production of ionization by solar extreme ultraviolet radiation and electron precipitation; loss through charge exchange with molecular nitrogen and oxygen; and transport by diffusion, neutral winds, and ExB convection drifts. The simulations are designed to contrast the signatures of various features of the ionosphere such as the Appleton anomaly, the high latitude trough, boundary and auroral blobs, and polar cap patches. Of particular interest is the contrast between the ground-based signatures and GPS/MET signatures. We also contrast the TEC given by a realistic ionosphere to that given by simple approximations of the ionosphere.

- P.H. Doherty, R. Loh, and D.N. Anderson, "Statistics of the Spatial and Temporal Variations in Ionospheric Range Delay", submitted to ION-GPS 97 to be held in Kansas City, MO in September, 1997.

Abstract

In this study, we present the statistics of the spatial and temporal variations in ionospheric range delay recorded at several locations in the continental US, Canada, Alaska and Hawaii. These measurements, recorded from 1993 through early 1997, were obtained from the International GPS Geodynamics Service (IGS) network, managed by the Jet Propulsion Laboratory. The statistics of spatial variations are based on simultaneous measurements made along different lines of sight at each location. Statistics of the temporal ionospheric variations are based on the highest elevation measurement at particular times of day at each individual receiver location. Since these measurements cover only solar moderate to minimum conditions, we augment the statistics on the temporal variations with a historical data base of ionospheric measurements recorded at similar locations over a full solar cycle. The historical data is based on Faraday rotation measurements of VHF signals from geostationary satellites of opportunity. Unfortunately, the sites included in the historical data are too widely spaced to infer spatial variations in the next solar maximum.

This analysis is intended to provide a characterization of ionospheric variations that will be encountered in the Federal Aviation Administration's (FAA) operational Wide Area Augmentation System (WAAS). The WAAS is intended to support en-route and precision approach flight operations. An important factor in the operational system will be the accuracy of

the vertical ionospheric delay estimates that will be provided to a user aircraft in a satellite broadcast message. These estimates of vertical ionospheric delay will be based on slant dual-frequency GPS measurements of ionospheric range delay made at 24 reference stations (21 in the continental US, 1 in Hawaii, 1 in Alaska and 1 in Puerto Rico). Historically, the ionosphere has proved to be extremely variable in nature. Its behavior is a function of geographic location, local time, season, geomagnetic activity and solar activity. In the continental US, measurements of ionospheric range delay at midday can range from less than 2 meters at solar minimum to nearly 20 meters at solar maximum. In Hawaii, daytime observations of range delay as high as 30 meters have been recorded during a solar maximum period. Fortunately, these large variations in the ionosphere develop slowly as a function of long term changes in solar activity and are not likely to cause degraded accuracy in the vertical ionospheric delay estimates for the WAAS. The most critical problems of ionospheric estimation for the WAAS will occur during periods of ionospheric scintillation and during periods of major geomagnetic storm activity when the spatial and temporal gradients in the ionosphere can be significantly higher than usual. This study will quantify the magnitude and frequency of these large spatial and temporal gradients observed with dual-frequency GPS from single locations during solar moderate to minimum periods. It will also provide a historical reference to the temporal gradients observed during a previous solar maximum period.

- D.T. Decker, C.E. Valladares, and D.N. Anderson, "Specifying the High Latitude F Region Weather" submitted to IAGA meeting to be held in Uppsala, Sweden in August 1997.

Abstract

Observations have shown that much of the high-latitude F-region weather is caused by small scale (irregularities) and large scale electron density structures. These same observations also suggest that there is an intimate cause and effect relation between the large scale structures (>10 km) and the smaller scale (<10 km) irregularities. Theoretical work on modeling large scale structures has recently demonstrated that we can simulate the formation and evolution of polar cap patches and boundary blobs, two types of F-region structures that are observed coincident with smaller scale irregularities. However, it has not been demonstrated that we can accurately model such structures at a particular place and time. In this paper, we report on efforts to use the Global Theoretical Ionospheric Model (GTIM) to determine what is required to accurately specify the appearance of patches and blobs. We will particularly focus on the sensitivity of model results to details of the time-varying convection pattern and the need for a weather specification of the high-latitude electric field.

- D.N. Anderson, D.T. Decker, P.H. Doherty, and M.W. Fox, "Modeling the Low Latitude F Region Weather" submitted to 1996 IAGA meeting to be held in Uppsala, Sweden in August, 1997.

Abstract

The low-latitude F-region is known as a very dynamic region where dramatic plasma irregularities can occur over a large range of scale sizes and amplitudes. However, it is also a region where the ambient F-region plasma has great day-to-day variability. In large part, this variability comes from the day-to-day behavior of the F-region electric field, in particular, the zonal field (vertical drift). This is so because the vertical drift is a key factor in determining the basic character of the low-latitude F-region. Thus, a primary requirement for modeling the low latitude space weather will be the ability to monitor the electric field and use it as a weather input to an ionospheric model. In this work, we are examining several observational sources (radar, digisonde, and magnetometer) for the day-to-day behavior of the vertical drift and will be using the resultant drifts as inputs to the Global Theoretical Ionospheric Model (GTIM). The usefulness of these sources will be judged by comparisons between GTIM results and various ionospheric measurements such as digisonde, radar, GPS, and TOPEX observations.

- D.T. Decker, C.E. Valladares, E. MacKenzie, D.N. Anderson, S. Basu, and Su. Basu, "Modeling the Climatology and Weather of Blobs", submitted to 1996 IAGA meeting to be held in Uppsala, Sweden in August, 1997.

Abstract

Over the last 30 years, observations have shown that the auroral F region contains mesoscale structures known as blobs. While these regions of enhanced plasmas have been categorized into several types and a variety of sources have been postulated, most work has been observational and only a few theoretical efforts have been reported [Robinson *et al.*, 1985; Anderson *et al.*, 1996]. In the recent work of Anderson *et al.* [1996], the Global Theoretical Ionospheric Model (GTIM) was used to model the formation of boundary blobs using time-varying convection. The structures produced had many of the features associated with boundary blobs. However, the next step is to demonstrate that both the general climatology of blobs can be modeled and that blobs in a particular region at a particular time can be modeled. We will report on efforts to compare theoretical blob morphology to observed scintillation morphology and first efforts to reproduce blobs observed on a specific day by the Chatanika radar. Discussion will focus on the global observations needed to provide the model inputs as well as the observations with which to constrain the model outputs.

Anderson, D.N., D.T. Decker, and C.E. Valladares, "Modeling Boundary Blobs Using Time Varying Convection", *Geophys. Res. Lett.*, 23, 579-582, 1996.

Robinson, R.M., R.T. Tsunoda, and J.F. Vickrey, "Sources of F region ionization enhancements in the nighttime auroral zone, *J. Geophys. Res.*, 90, 7533-7546, 1985.

6. JOURNAL ARTICLES

Copies of reprints of the following two papers appear in this section:

- C.E. Valladares, D.T. Decker, R. Sheehan, and D.N. Anderson, "Modeling the formation of polar cap patches using large plasma flows", *Radio Science*, **31**, 573-593, May-June 1996.
- D.T. Decker, B.V. Kozelov, B. Basu, J.R. Jasperse, and V.E. Ivanov, "Collisional Degradation of the Proton-H Atom Fluxes in the Atmosphere: A Comparison of Theoretical Techniques", *J. Geophys. Res.*, **101**, 26947-26960, 1996.

A copy of the following camera-ready paper also appears in this section:

- P.H. Doherty, D.N. Anderson, and J.A. Klobuchar, "Total Electron Content Over the Pan American Longitudes: March-April 1994", *Radio Science*, *in press*.

Modeling the formation of polar cap patches using large plasma flows

C. E. Valladares, D. T. Decker, and R. Sheehan

Institute for Space Research, Boston College, Newton Center, Massachusetts

D. N. Anderson

Phillips Laboratory, Geophysics Directorate, Hanscom Air Force Base, Massachusetts

Abstract. Recent measurements made with the Sondrestrom incoherent scatter radar have indicated that the formation of polar cap patches can be closely associated with the flow of a large plasma jet. In this paper, we report the results of a numerical study to investigate the role of plasma jets on patch formation, to determine the temporal evolution of the density structure, and to assess the importance of O⁺ loss rate and transport mechanisms. We have used a time-dependent model of the high-latitude F region ionosphere and model inputs guided by data collected by radar and ground-based magnetometers. We have studied several different scenarios of patch formation. Rather than mix the effects of a complex of variations that could occur during a transient event, we limit ourselves here to simulations of three types to focus on a few key elements. The first attempt employed a Heelis-type pattern to represent the global convection and two stationary vortices to characterize the localized velocity structure. No discrete isolated patches were evident in this simulation. The second modeling study allowed the vortices to travel according to the background convection. Discrete density patches were seen in the polar cap for this case. The third case involved the use of a Heppner and Maynard pattern of polar cap potential. Like the second case, patches were seen only when traveling vortices were used in the simulation. The shapes of the patches in the two cases of moving vortices were defined by the geometrical aspect of the vortices, i.e. elliptical vortices generated elongated patches. When we “artificially” removed the Joule frictional heating, and hence any enhanced O⁺ loss rate, it was found that transport of low density plasma from earlier local times can contribute to ~60% of the depletion. We also found that patches can be created only when the vortices are located in a narrow local time sector, between 1000 and 1200 LT and at latitudes close to the tongue of ionization.

1. Introduction

Large-scale density structures are commonly observed in the polar cap. When the interplanetary magnetic field (IMF) is directed southward mesoscale (100 to 1000 km), density enhancements, named polar cap “patches”, drift across the polar cap in the antisunward direction [Buchau *et al.*, 1983; Weber *et al.*, 1984, 1986; Fukui *et al.*, 1994]. When the IMF is directed northward, elongated streaks of precipitation-enhanced F region

plasma extend aligned to the noon-midnight meridian and move toward dawn or dusk [Buchau *et al.*, 1983; Carlson *et al.*, 1984; Valladares *et al.*, 1994a]. Both types of structures can be associated with intense levels of scintillation [Weber *et al.*, 1984; Buchau *et al.*, 1985; Basu *et al.*, 1985, 1989] and disrupt radio satellite communication systems. In this paper, we investigate theoretically the formation of plasma density enhancements that occur during B_z south conditions. To conduct this study, we have used a three-dimensional time-dependent model of the high-latitude F region ionosphere developed by Anderson *et al.* [1988, 1996] and Decker *et al.* [1994]. Differing from previous attempts, we have incorporated into the model analytical expressions of localized electric field structures and their

Copyright 1996 by the American Geophysical Union.

Paper number 96RS00481.
0048-6604/96/96RS-00481\$11.00

time-dependence. We checked the validity of the model results by conducting a detailed comparison with data gathered from the Sondrestrom incoherent scatter radar (ISR) during patch formation events.

The source of the plasma and the physical processes that form the polar cap patches have been under investigation for over 10 years. *Buchau et al.* [1985] and *de la Beaujardiere et al.* [1985] were the first researchers to address the question of the origin of the density inside the patches. *Buchau et al.* [1985] measured values of $f_o F_2$ at Thule, Greenland (86° magnetic latitude), showing large fluctuations. The minimum $f_o F_2$ values were equal to densities produced locally by the sun EUV radiation, but the maximum values were similar to the densities that were produced at locations equatorward of the auroral oval. These observations suggested that the plasma density inside the patches was produced by solar radiation in the sunlit ionosphere, probably at subcusp latitudes, and then carried into and across the polar cap by the global convection pattern. In fact, *Weber et al.* [1984] and *Foster and Doupinik* [1984] confirmed the presence of a large eastward electric field near midday, likely directing the subauroral plasma poleward. *Buchau et al.* [1985] found also that the occurrence of patches displayed a strong diurnal UT control. The patches were seen at Thule almost exclusively between 1200 and 0000 UT. This UT control of the polar cap F layer ionization was interpreted in terms of the displacement of the convection pattern with respect to the geographic pole. It is because of this displacement that the polar convection is able to embrace higher-density plasma only at certain UT hours [*Sojka et al.*, 1993, 1994]. However, the mechanism (or mechanisms) by which the auroral plasma can break up into discrete entities is still a matter of debate.

Tsunoda [1988] summarized the role of different mechanisms conducive for patch generation. He suggested that changes in the B_y and/or B_z components of the IMF could originate temporal variations in the global flow pattern, drastically disturbing the density distribution within the polar cap. In the mid 1980s, several theoretical studies were designed to study the production, lifetime, and decay of large-scale structures inside the polar ionosphere [*Sojka and Schunk*, 1986; *Schunk and Sojka*, 1987]. These authors indicated that hard precipitation could produce plasma enhancements similar to the patches and blobs found in the auroral oval. They argued that in the absence of solar radiation, although the particle-produced E region will rapidly recombine, the longer lifetime enhanced F region ionization could build up and persist for several hours. *Sojka and Schunk*

[1988] theoretically demonstrated that large electric fields could create regions of density depleted by a factor of 4. *Anderson et al.* [1988] presented a model of the high-latitude F region that was used to investigate the effect of sudden changes in the size of the polar cap upon density enhancements transiting the polar cap. While these model studies were able to form structures, most of the success in patch modeling has been attained only after the first High Latitude Plasma Structures meeting was convened at Peaceful Valley, Colorado, in June 1992. *Sojka et al.* [1993] conducted numerical simulations of the effect of temporal changes of the global pattern. The latter two studies were successful in producing density structures at polar cap latitudes. *Decker et al.* [1994] used six different global convection patterns and localized velocity structures to reproduce the digisonde measurements of $f_o F_2$ values at Sondrestrom. *Lockwood and Carlson* [1992] used the formulation of transient reconnection [Cowley et al., 1991] to suggest that a transient burst of reconnection together with the equatorward motion of the ionospheric projection of the X line could extract a region of the high density subauroral plasma, divert the subauroral density poleward, and finally "pinch off" the newly formed patch. More recently, *Valladares et al.* [1994b] has shown a case study where a fast plasma jet containing eastward directed velocities in excess of 2.5 km s^{-1} was able to increase the O^+ recombination rate and yield an east-west aligned region of reduced densities across a poleward moving tongue of ionization (TOI). *Rodger et al.* [1994] presented data from the Halley Polar Anglo-American Conjugate Experiment radar in Antarctica, suggesting that a region of depleted densities can be carved out by increased O^+ recombination due to large plasma jets.

This paper presents a detailed modeling of the mechanism of patch formation presented by *Valladares et al.* [1994b] and *Rodger et al.* [1994]. The mechanism described here operates in conjunction with a background poleward convection to produce mesoscale polar structures from subauroral plasma. This process may also have an essential role in determining the size and the shape of the polar cap patches. The basic elements of this mechanism are (1) a fast plasma jet, observed near the midday auroral oval, (2) enhanced ion temperature due to Joule frictional heating, (3) enhanced recombination rates of O^+ , and, (4) transit of low density plasma from earlier local times.

The paper has been organized in the following manner. Section 2 succinctly describes our model of the high-latitude ionosphere [*Anderson et al.*, 1988; *Decker et al.*, 1994] and the calculations of the localized electric fields

incorporated into the model. Section 3 presents results of a computer model of a patch formation mechanism using convection patterns for typical IMF B_y positive and negative values. An assessment of the ability of enhanced recombination loss to erode parts of the TOI and to disconnect regions from the oval is also discussed in this section. Section 4 presents model calculations for vortices located at several different local times. The paper concludes with the discussion and conclusions section.

2. Model Description

The Global Theoretical Ionospheric Model (GTIM) calculates the density altitude profile of a single ion (O^+) along a flux tube. It solves the coupled continuity and momentum equations for ions and electrons. The solution of the differential equations is simplified by selecting a coordinate system in which one dimension is defined parallel to the local magnetic field. The model attains three-dimensionality by repeating the profile calculations along many (a few thousand) flux tubes. The locations of the flux tubes are selected to cover the range of latitudes and local times desired for the simulation. The mathematical foundation of the GTIM model was introduced by *Anderson* [1971, 1973]. Although initially used to study the low-latitude ionosphere, it has been extended to include physical processes of the high-latitude ionosphere, such as the effects of large electric fields and particle precipitation [*Anderson et al.*, 1988; *Decker et al.*, 1994]. Recently, *Decker et al.* [1994] have described how the inputs to the GTIM model can easily accommodate a time-dependent convection pattern and spatially localized regions containing high flows to represent highly variable situations, such as those existing in the cusp region. Other geophysical input parameters, such as the neutral density and wind, along with several initial conditions, such as the plasma density, can be freely defined to simulate different scenarios. In this paper, we have adjusted the global convection pattern and included a local electric field to reproduce the velocities measured on February 19, 1990, by the Sondrestrom ISR.

The radar and magnetometer measurements used to define the model inputs were discussed by *Valladares et al.* [1994b]. These authors observed a large channel oriented in the east-west direction containing jet-type eastward velocities of order 2 km s^{-1} . In this channel, the ion temperature (T_i) was enhanced and the density (N_e) was depleted. These signatures in the T_i and N_e

values implied a likely increase in the O^+ recombination rate. Successive radar scans indicated that the plasma jet was continuously moving poleward. This motion was also confirmed by the large negative deflection seen at later times by magnetometers located at latitudes poleward of Sondrestrom. The large negative deviation of the H component due to Hall currents appeared at Qaanaaq 29 min after being observed at Sondrestrom. This implied an average poleward displacement of 620 m s^{-1} for the plasma jet. *Valladares et al.* [1994b] also presented equivalent velocity vectors deduced from the magnetometers located along the east coast of Greenland, implying a flow vorticity. Similar vorticity was seen in the resolved radar velocity vectors. The radar line-of-sight velocity also indicated that adjacent to and both northward and southward of the large plasma jet there existed regions of westward flows. In summary, the radar and magnetometer data suggested the presence of two adjacent vortices of opposite vorticity with the common region in the middle comprising the plasma jet. The GTIM model also requires other geophysical parameters, such as the neutral density, wind and temperature, the ionization, and chemical loss rates, and the diffusion coefficients. These latter atmospheric parameters were selected as described by *Decker et al.* [1994]. The neutral densities and winds were calculated using the mass spectrometer/incoherent scatter 1986 (MSIS-86) model [Hedin, 1987] and Hedin's wind model [Hedin et al., 1991]. The ion loss rate was computed as a function of an effective temperature. This parameter is derived using the following equation of *Schunk et al.* [1975]:

$$T_{\text{eff}} = T_n + 0.329E^2$$

where E is the magnetospheric electric field in millivolts per meter.

Plate 1 displays the $N_m F_2$ values of the high latitude ionosphere as a function of magnetic latitude and local time. These values were obtained with the GTIM model after following 7200 flux tubes during 8 hours of simulation time. During this time, the global convection pattern and other relevant ionospheric parameters were kept constant. The purpose here was to obtain the initial ionospheric densities to be used as a convenient starting point for simulating the ionospheric effects of a plasma jet. The actual ionosphere rarely has 8 hours of such steady conditions. However, this allows us to single out individual effects that can be produced by various ionospheric processes. The real ionosphere may be a superposition of several of these plasma jet



Plate 1. Polar plot of the NmF2 (peak F region density) of the high-latitude ionosphere at 1300 UT. This density plot corresponds to the initial values used in the simulations of sections 3.1, 3.2, 3.4, and 4. The values in this plot were obtained by running the model for 8 hours and using steady state inputs. We include in the lower right corner the black and white version of this plot in a format that will be shown in subsequent plots. The black dots correspond to the locations of the Sondrestrom and Qaanaaq stations, and the white dot indicates the location of the European Incoherent Scatter station. The latitudinal circles are in steps of 10°.

and density break-off events. A prominent feature of Plate 1 is the presence of the TOI. At 1300 UT it extends from longitudes close to European Incoherent Scatter EISCAT (19°E) up to 51°W, where it turns poleward. The TOI is bounded at the equatorward edge by a region of densities reduced by 30% and poleward by densities almost an order of magnitude smaller. The larger densities in the TOI are due mainly to two factors, a small westward flow in the dusk cell and an upward lift of the F region. The longer transit time and the relatively smaller solar zenith angle permit the solar radiation to build up much higher densities in this

confined region. Similar steady structures have been presented by *Crain et al.* [1993] in their total electron content maps of the high-latitude region.

The vorticity suggested by the radar and magnetometer data and other theoretical implications of solar wind - magnetosphere interactions [Newell and Sibeck, 1993] led us to infer that the plasma jet may actually consist of a system of two vortices superimposed on the background convection. With this as a guide, we searched for a system of two ellipsoidal potential vortices added to a global convection pattern. The search was carried out by varying the cross polar

Table 1. Global and Local Velocity Patterns

Global pattern	B_y	Polar Cap Potential, kV	Number of Vortices	Major Axis, deg	Minor axis, deg	Vortex Potential, kV	Latitude of Vortices, deg	Local Time of Vortices, deg
Heelis 12° radius	+	80	2	10, 10	2.4, 1	20, -5	74, 71.5	11, 11
Heppner-Maynard	-	76	2	10, 10	2.4, 1	20, -5	74, 71.5	11, 11

cap potential, the global pattern, the radius of the polar cap and other geometrical parameters of the two-vortex system. The size, peak-to-peak voltage, location, orientation and aspect of the vortices were systematically changed iteratively to obtain the best fit to the radar velocities. We tried over 10 million combinations. Table 1 presents the general parameters of the vortices and the global pattern that provided the best fit to the Sondrestrom velocity data. A Heelis-type pattern gave the smallest error. However, a Heppner and Maynard $B_y < 0$ pattern provided errors almost as small as the Heelis-type pattern. Because the radar azimuthal scan covers a small region of the total pattern, this method is not very sensitive in discriminating the

convection pattern. Figures 1a and 1b show the Heelis-type global convection pattern and the system of the two vortices of Table 1. Figure 1c depicts the result of adding the velocity patterns of Figures 1a and 1b. Figure 1d represents the simulated line-of-sight velocities which would have been measured at Sondrestrom if the pattern in Figure 1c had been in effect. The agreement between Figure 1d and Figure 6a of Valladares et al. [1994b], reproduced here as Figure 1e, is very good. Figure 1f shows the total vector velocity that was obtained using the convection pattern of Figure 1c.

Figure 2 shows the plasma density measured by the Sondrestrom ISR on February 19, 1990, during four

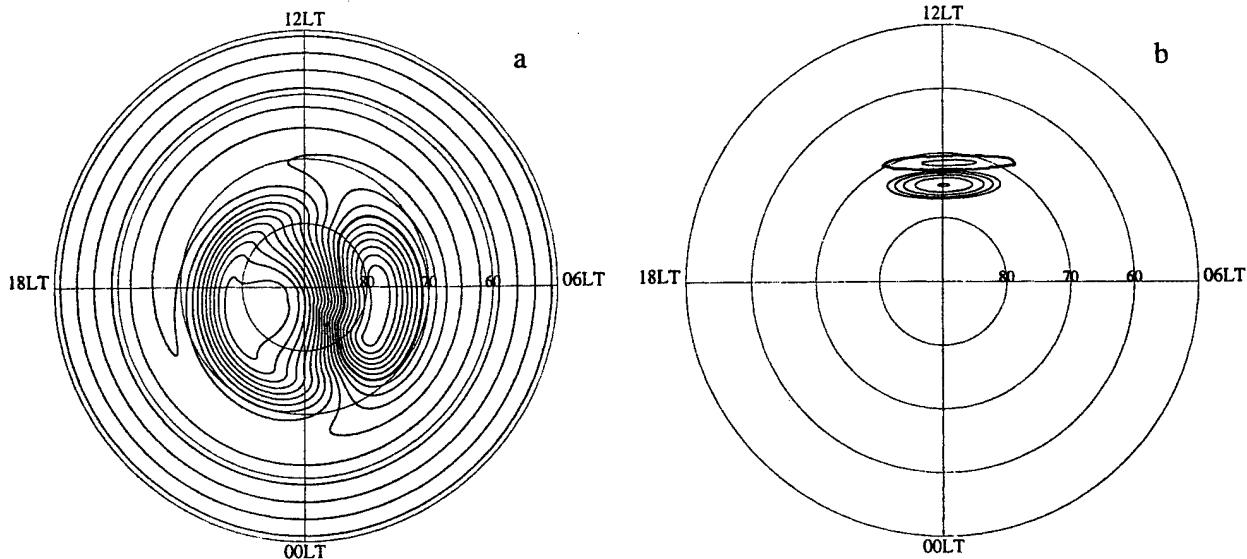


Figure 1. Series of polar plots. (a) High-latitude potential corresponding to a Heelis-type pattern for $B_y = +8$ nT. The cross polar cap potential is 80 kV, and the radius of the polar cap is 12°. (b) the potential of the convective vortices. (c) Addition of the potentials in Figures 1a and 1b. (d) Simulated Sondrestrom line-of-sight velocities considering that the potentials of Figure 1c were in effect. (e) Line-of-sight velocities measured by the Sondrestrom radar on February 19, 1990 [Valladares et al., 1994b, Figure 6a]. (f) Simulated vector velocities using the potential of Figure 1c.

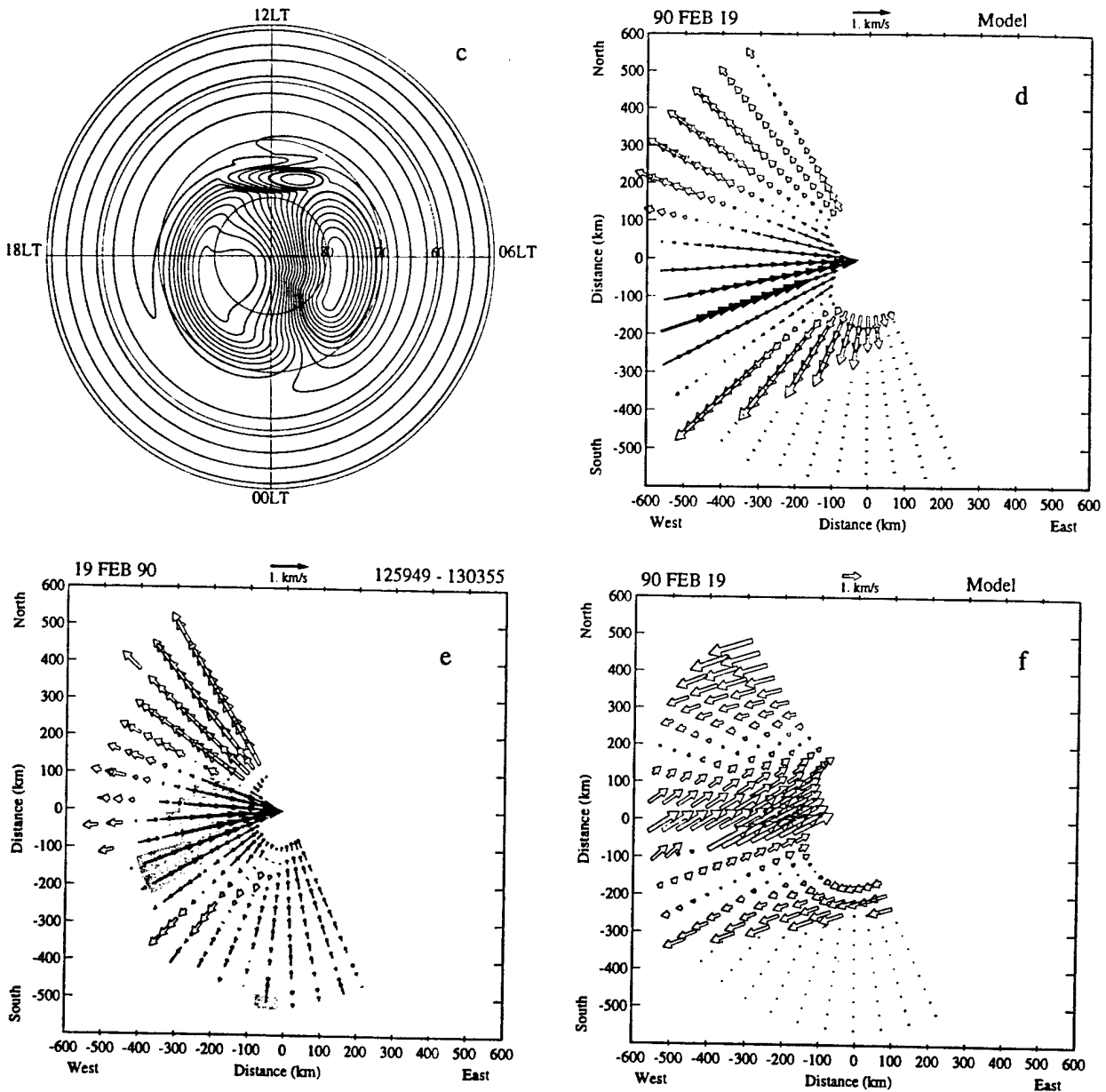


Figure 1. (continued)

consecutive elevation scans. Figure 2a, obtained between 1251 and 1254 UT and before the appearance of the plasma jet, shows a density value above $3 \times 10^5 \text{ cm}^{-3}$ to the south of the radar. Overhead and to the north, the density is structured and peaks at $5.5 \times 10^5 \text{ cm}^{-3}$. These values are in good qualitative agreement with the modeled densities of Plate 1. The maximum modeled peak densities are $5 \times 10^5 \text{ cm}^{-3}$ and $9 \times 10^5 \text{ cm}^{-3}$ for the south and north locations respectively.

3. Patch Modeling Using Mesoscale Velocity Structures

During the last decade, a large array of transient events have been measured in the high-latitude ionosphere. Convective vortices, double vortices, east-west elongated ellipses, and vortices moving poleward, equatorward, downward and duskward have all been observed. While the magnetic response of these events have been studied

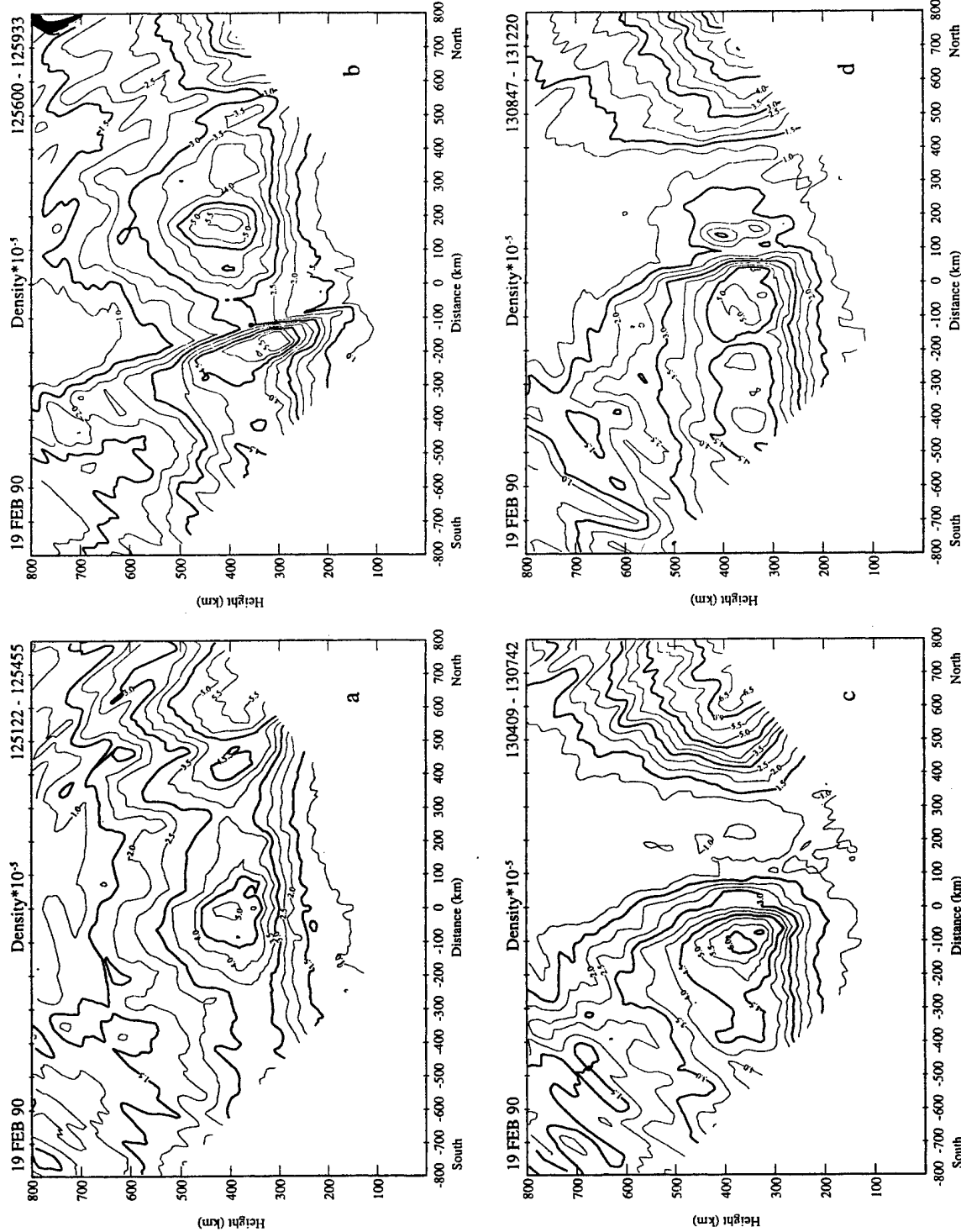


Figure 2. Density contours corresponding to four elevation scans of the Sondrestrom Incoherent Scatter Radar. The spacing between the contours is $.5 \times 105$ cm $^{-3}$. The antenna azimuth angle was kept fixed at -27° (magnetic meridian), and the elevation varied from 30° south to 30° north. The number density is displayed as a function of height and distance along the magnetic meridian.

in some detail [Goertz *et al.*, 1985; Heikkila *et al.*, 1989; Ma *et al.*, 1991], very little is known about their effect upon the ionospheric densities. Furthermore, transient events have been observed to have a fairly complex temporal behavior that is not well understood. As a result, rather than attempting a simulation that tries to include all of the observed behavior of a transient event, we have performed four numerical simulations that focus on just a few key elements of the event. The four scenarios modeled were chosen to help us learn how the density evolves under different conditions of the local and global patterns and to give us some insight as to how sensitive our results are to the various properties of these events. In the next four subsections, we report on the results from these simulations. First, we describe a case study in which a pair of transient vortices are kept fixed in a corrected geomagnetic coordinate system. In the next case, we include the observation that these transient vortices move by allowing the vortices to drift according to the background polar cap flow. We continue with a model case study that uses a Heppner-Maynard-type convection pattern as the global convection. This allows us to assess the sensitivity of our previous results to the global pattern that is chosen. Finally, in the fourth simulation, we establish the importance of the enhancement of the recombination rate in producing regions of depleted density across the TOI.

3.1. Stationary Vortices

The first modeling effort was implemented using two vortices which were maintained stationary in a local time versus latitude frame of reference. The vortices' potential is set equal to the predetermined value at 1300 UT; 15 min later the potential is turned off. Figure 3 and successive figures present a limited region of the northern hemisphere high latitude ionosphere. Here we show a series of snapshots of the $N_m F_2$ corresponding to nine different times during the formation of the density structure. The area covered in each panel is about $3500 \times 3500 \text{ km}^2$. Figures 3a through 3f are 3 min apart. Figures 3g - 3i display the density in steps of 10 min. Figure 3a displays the initial density at the time of the potential vortices onset. This plot corresponds to a view looking down from a satellite that is traveling from the pole toward the equator. Lower latitudes are at the top of the figure, and poleward latitudes are at the bottom. The magnetic pole is at the center of the bottom edge of each panel. The locations of the Sondrestrom and Qaanaaq facilities are indicated by white dots.

The TOI is clearly depicted in Figure 3a; it extends nearly aligned with the equipotential lines and turns poleward near Sondrestrom. We remind the reader that the $N_m F_2$ pattern of Figure 3a was calculated for February 19 at 1300 UT using the actual magnetic and solar flux conditions measured on that day and the inferred size of the polar cap, as defined in section 2. A weaker TOI may be obtained for other days of the year, different UT, or even different parameters of the convection pattern. Figure 3b displays the peak density 3 min after the vortex potential has been activated. Even at this time, the TOI is already drastically distorted. A section of the TOI has rotated anticlockwise; simultaneously, three parallel channels containing depleted densities have been created, two equatorward and one poleward of the fragmented TOI segment. All three elongated traces of low density are coincidental with the equatorward, center, and poleward walls of the vortices, which is where the high speed flows and the enhanced temperatures are. Three minutes later at 1306 (Figure 3c), all three low-density channels are further elongated in the east-west direction. A region of low density starts propagating poleward at the poleward edge of the vortex system. The following three panels (Figures 3d to 3f) show further elongation and deeper depletions in all three density channels. Clearly, the presence of the vortices has produced density structures. However, the density structure aligned in the east-west direction (Figure 3f) is still attached to what remains of the TOI. After the localized potential is turned off at 1315 UT, the density structures lose their east-west alignment. Figures 3g to 3i show that the density enhancement acquires instead a more north-south alignment. This additional change in the shape of the density structure is due to a nonuniform velocity near the center of the polar cap of the Heelis-type pattern in Figure 1a. If the flow were uniform, then the equipotential lines should have been parallel lines in the polar plot.

Figure 4 presents simulated radar elevation scans through the modeled ionospheric volume. Each of the panels shows an equivalent elevation scan in the meridian plane that would have been measured at Sondrestrom if the modeled densities were the real densities around the station. This scheme allows us to perform a one-to-one comparison with the data presented by Valladares *et al.* [1994b]. It helps us to better understand the radar data when only elevation scans are conducted during the experiment. Each of the scans of Figure 4 are constructed from the density data displayed in the corresponding panels of Figure 3. The orientation of the scans is shown by the white lines in each panel of Figure 3. The larger

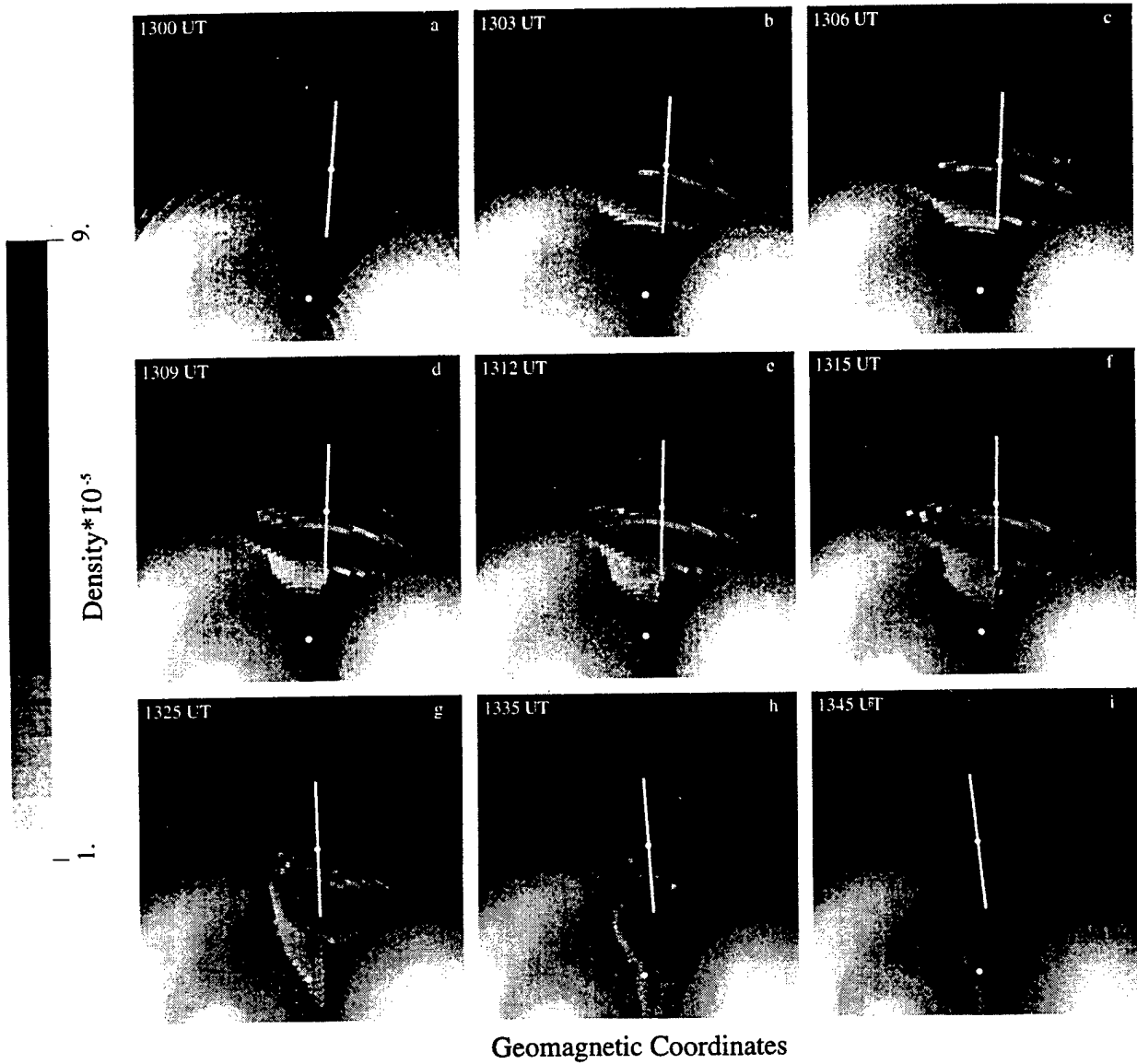


Figure 3. Each panel presents NmF2 values of a section of the high-latitude ionosphere at different times during the modeling that uses stationary vortices as input. See section 3.1 for more details. The white dots correspond to the locations of the Sondrestrom and Qaanaaq stations. The white line that crosses the Sondrestrom site indicates the extension of the elevation scans of Figure 2.

density at the northern part of the scan of Figure 4a is due to the passage of the TOI. Figure 4b, corresponding to 3 min along the simulation, shows mesoscale structuring coincident with the vortices. Two deep depletions are evident, one overhead and the other 500 km north of the station. The density of the northern depletion is $3 \times 10^5 \text{ cm}^{-3}$. The density remains unperturbed at the northern and southern extremes of the scan; no vortices are located

there. At 1309 UT, 9 min after the beginning of the simulation, both depletions reach a minimum value of $2 \times 10^5 \text{ cm}^{-3}$. The N_e depletion located almost overhead coincides with the center of the vortex, where the plasma flow is maximum. Figure 4e presents the modeled densities 12 min after the onset of the potential vortices. These contours can be closely compared with Figure 2c which shows the density measured by the Sondrestrom

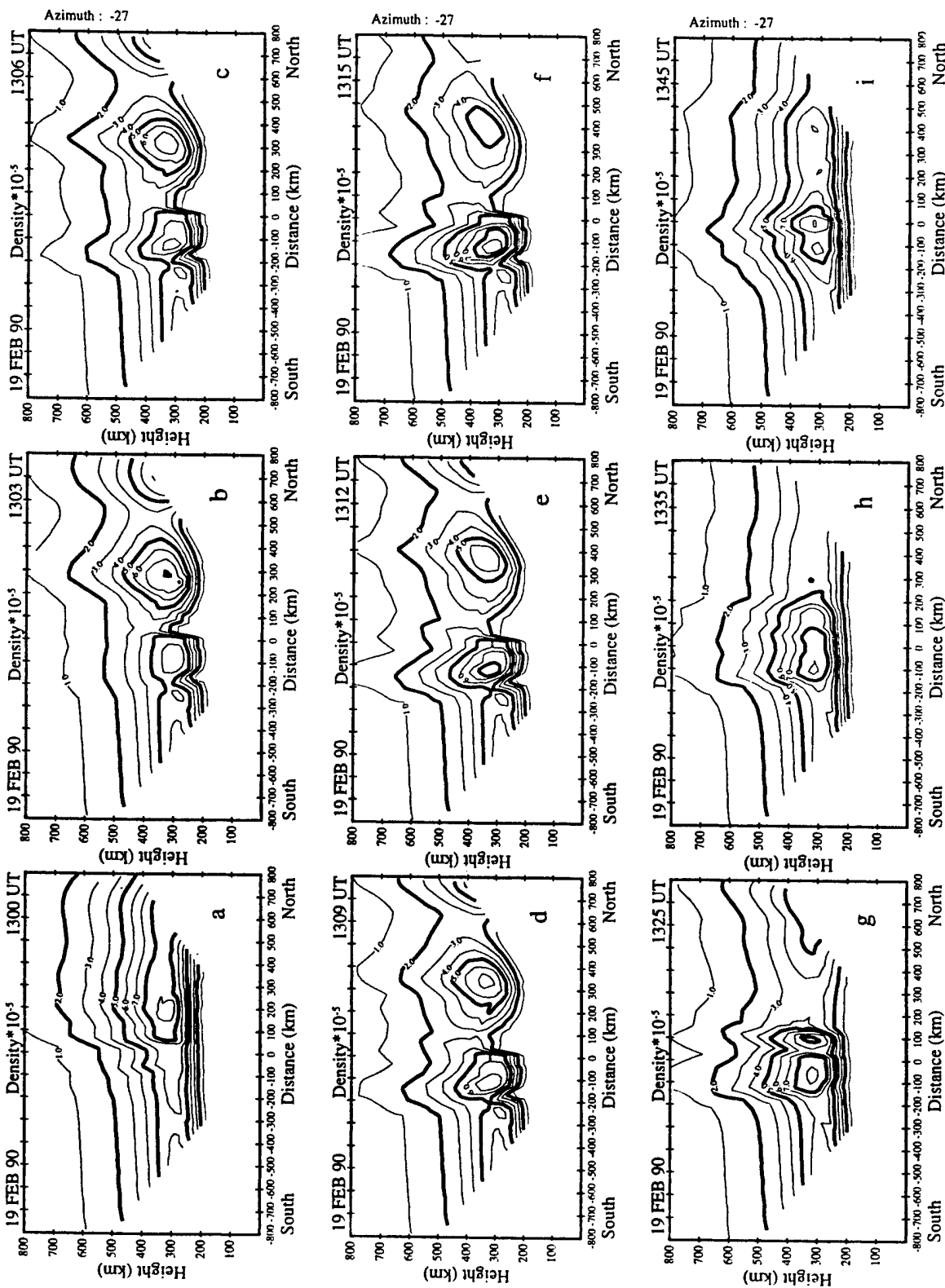


Figure 4. Simulated radar elevation scans through the simulated volume of section 3.1. (a) The large-scale density structure corresponds to the TOI. (b) - (i) The fragmentation of the TOI and formation of smaller-scale structures.

radar ~12 min after the start of the break-off event. Each figure displays two density structures separated by a channel of low density located almost overhead. The peak density in each of the structures shows a good agreement between modeled and measured values. However, the minimum density situated between structures is much more depleted in the experimental data. It is below 10^5 cm^{-3} in the radar data but above $2 \times 10^5 \text{ cm}^{-3}$ in the model. Other differences between the measured and modeled densities are (1) the larger north-south extension of the density depleted region of the measured data, and (2) the noticeable higher bottomside F layer density of the experimental data.

While the stationary vortices scheme increases the amount of density structures transiting within the polar cap, it fails to produce isolated islands of enhanced density structures detached from the auroral oval. A camera located within the polar cap will be able to indicate this effect. Moreover, our definition of polar cap patches postulates that less dense plasma should surround the higher density plasma in all directions in order to qualify as a patch. Thus we conclude that stationary vortices do not reproduce all the characteristics of polar cap patches.

3.2. Traveling Vortices

The second modeling effort was carried out using a set of two traveling vortices moving with the background plasma flow. To generate the motion of the vortices, the two-vortex system was displaced in the antisunward direction as a whole entity. The displacement was set by the velocity of the plasma at the center of the line joining the vortices' centers. Similar to the previous case, the vortices potential was introduced at 1300 UT. The potential was then reduced by half 15 min later. The location of the vortices in the polar cap was updated every 30 s; this interval was equal to the step time of the simulation. Figure 5a repeats the initial density of Plate 1. During the first 9 min of the simulation (Figures 5b - 5d), the TOI is drastically distorted in a fashion similar to the nonconvective case. However, the width of the depletion channel and the depth of the density decrease are larger for the convecting vortices case. The dawn-dusk extension of the density structure is smaller in this convective scenario. We call this structure a region of enhanced density, because N_e is higher inside the structure than in the rest of the polar cap. Figures 5d through 5f show that both density structures develop an east-west or dawn-dusk alignment. They are also well collocated with the corresponding vortices. In contrast to

the nonconvecting vortices case, we see (Figure 5f) that the more northern density structure has no attachment to the oval or subauroral plasma. The last three panels at the bottom of Figure 5 show that as two patches travel antisunward across the polar cap, they suffer little distortion. This feature is also different from the previous case, where only one structure was fully formed. The prominent characteristic continues to be that both structures are individual entities with no attachment to the oval or subauroral plasma. The polar cap patches, as described here, are very similar in shape to the "cigar" patches, elongated in the east-west direction, described by Fukui et al. [1994].

A more quantitative view of the formation of the density enhancement and depletion is displayed in Figure 6. Figures 6b and 6c show the cross section in the magnetic meridian plane of two structures that were formed by the convective vortices. The structure located at 100 km south of the station was formed from plasma located at subauroral latitudes (south of the TOI). The N_e structure located at 300 km north is formed from the TOI. The particular location of the vortex causes plasma from the fragmented TOI to intrude into the southern velocity structure and reach values near $9 \times 10^5 \text{ cm}^{-3}$. The minimum density between patches is 10^5 cm^{-3} , as seen at 100 km north in Figure 6e. This depletion is replenished partially by solar radiation and reaches values near $3 \times 10^5 \text{ cm}^{-3}$ in Figure 6h. Comparison of Figures 6e and 2c indicates a good qualitative agreement. The modeled densities of Figure 6e show a slightly higher density value and a narrower width in the region of depleted densities. In this region, the modeled density are $<10^5 \text{ cm}^{-3}$ at 300 km altitude, similar to the experimental values.

The traveling vortices scenario brought only a qualitative agreement with the density of Figure 2c. However, it was able to produce islands of high density transiting the polar cap. Thus we conclude that the convecting vortices are able to form patches of enhanced densities when they are located near the boundary between the polar cap and the auroral oval.

3.3. Heppner-Maynard-Type B_y Negative Global Pattern

As mentioned in section 2.1, the radar data is not effective at discriminating between different global patterns. Thus it is of interest to see how our results might change if a different global pattern is used with the vortices. For this purpose, we repeated the calculations of the previous section to determine the effect on patch formation using a Heppner-Maynard-type pattern. Figure

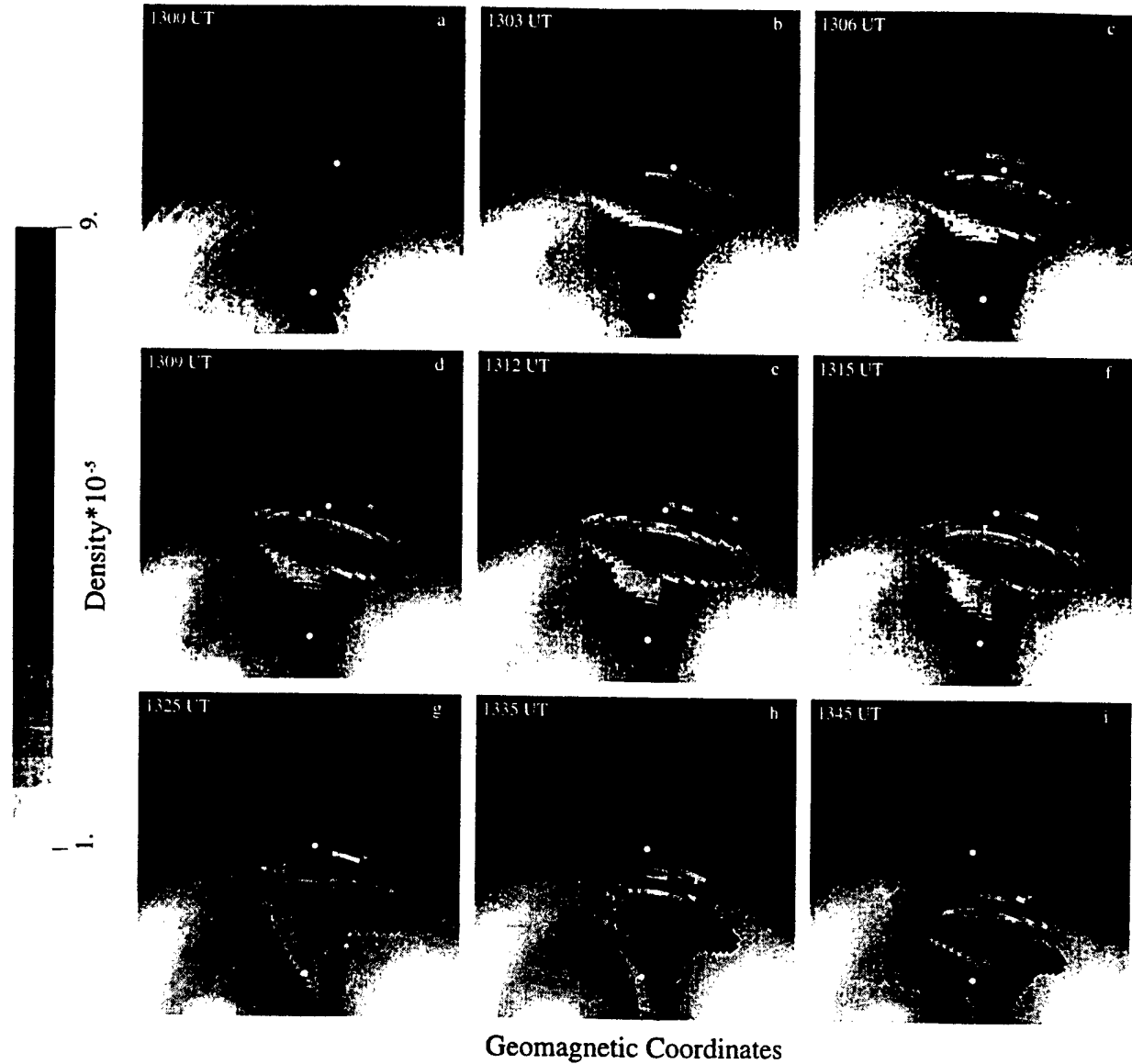


Figure 5. Same as Figure 3 but for the modeling study of traveling convective vortices (section 3.2).

7a displays the initial conditions of the $N_m F_2$ values before the start of the simulation. The TOI shows a few peculiar differences with respect to the Heelis-type convection pattern of section 3.1. The maximum density is slightly higher, and the TOI is a much wider before it turns poleward. These differences are attributed to a slower flow velocity (stagnation region) near the dayside region in the Heppner-Maynard global convection patterns. The initial location of the vortices and the amplitude of each vortex potential are similar to the case described in section 3.2.

Figures 7b and 7c show that the vortices are able to bisect a region of the TOI and orient the major axis of the density structure in the dawn-dusk direction. A second region of depleted densities is seen at the lower latitudes in Figures 7c through 7f; however, this structure is not completely isolated from the TOI. Moreover, it joins the new TOI that is being formed during the last stages of the simulation. The patch located at higher latitudes retains its alignment for several minutes after the potential was reduced by 50% (Figures 7g - 7h). Figure 8 shows that the patch is bounded on the equatorward side by plasma

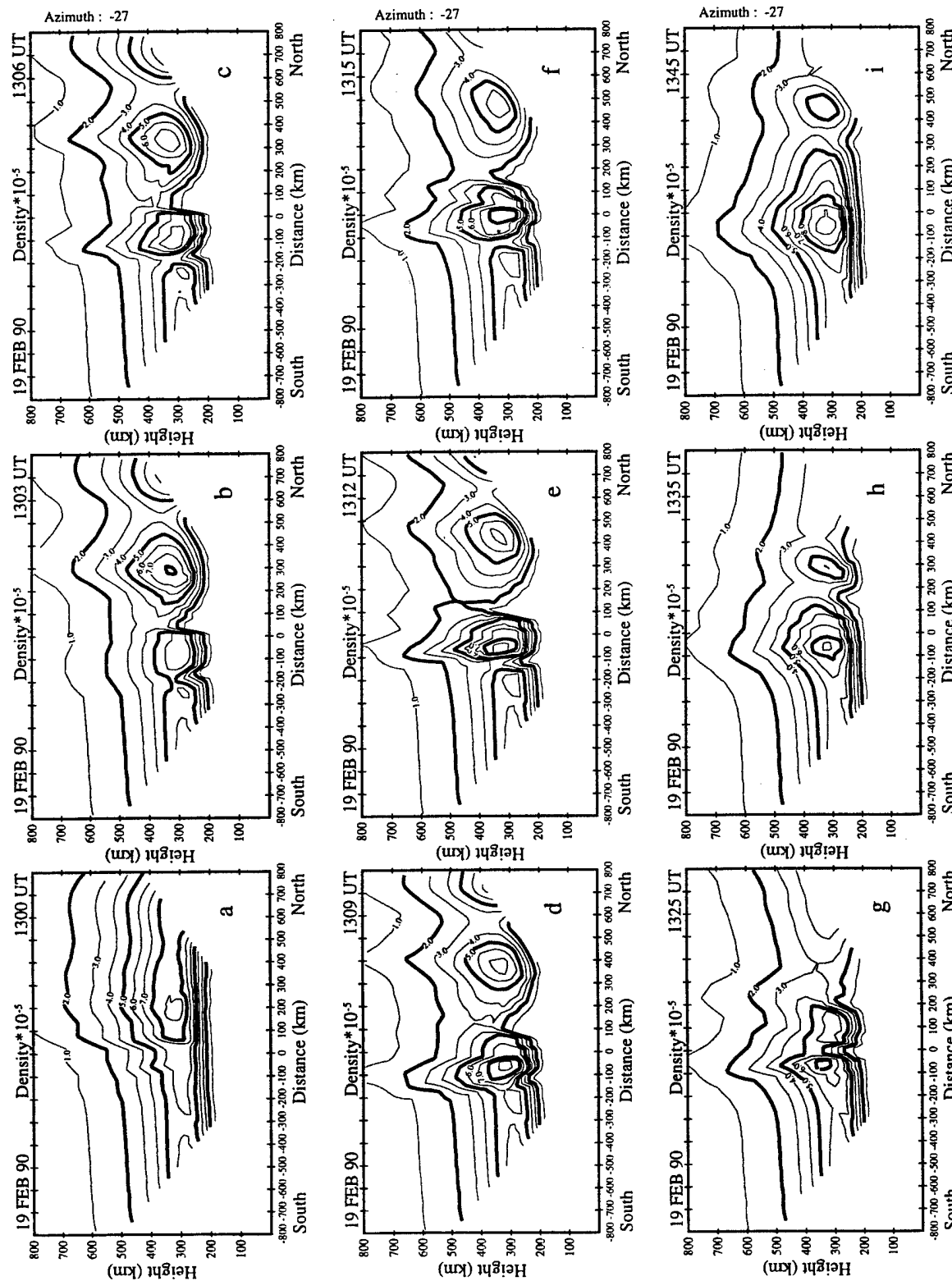


Figure 6. Same as Figure 4 but for the modeling study of traveling convective vortices (section 3.2).

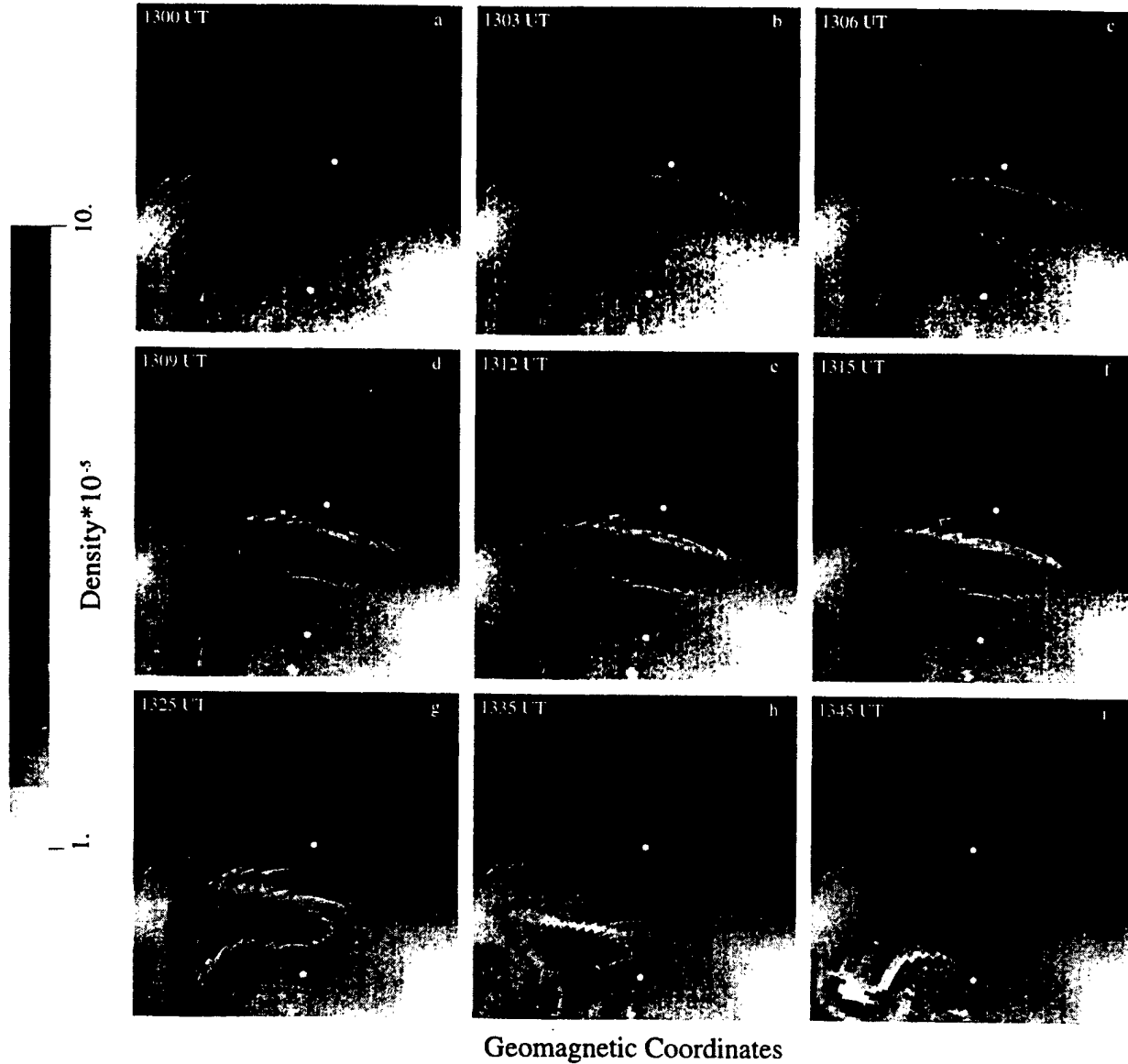


Figure 7. Same as Figure 3 but for the Heppner-Maynard convection pattern (section 3.3).

as low as 10^5 cm^{-3} . It also demonstrates that the patch moves toward the pole and subsequently breaks from the TOI. When the patch is circulating across the polar cap, the peak density inside the patch is $8 \times 10^5 \text{ cm}^{-3}$, a value much higher than the typical $1-2 \times 10^5 \text{ cm}^{-3}$ seen in the polar cap and outside the TOI. Figures 8e and 8f show a more pronounced depletion between the density structures as compared to the Heelis/traveling vortices scenario. When compared to the experimental values of Figure 2c, we notice that several features are well

reproduced. The altitude extension of both structures are very similar. $N_e = 7 \times 10^5 \text{ cm}^{-3}$ at 700 km is observed in both experimental and modeled data. The region of depleted density is wider than in the previous case. The poleward motion of the structures also resembles more closely the movement of the structures seen in the experimental data. The Heppner-Maynard pattern successfully produced a density structure with all the characteristics of a polar cap patch. In contrast to the Heelis convection pattern, it creates a single structure.

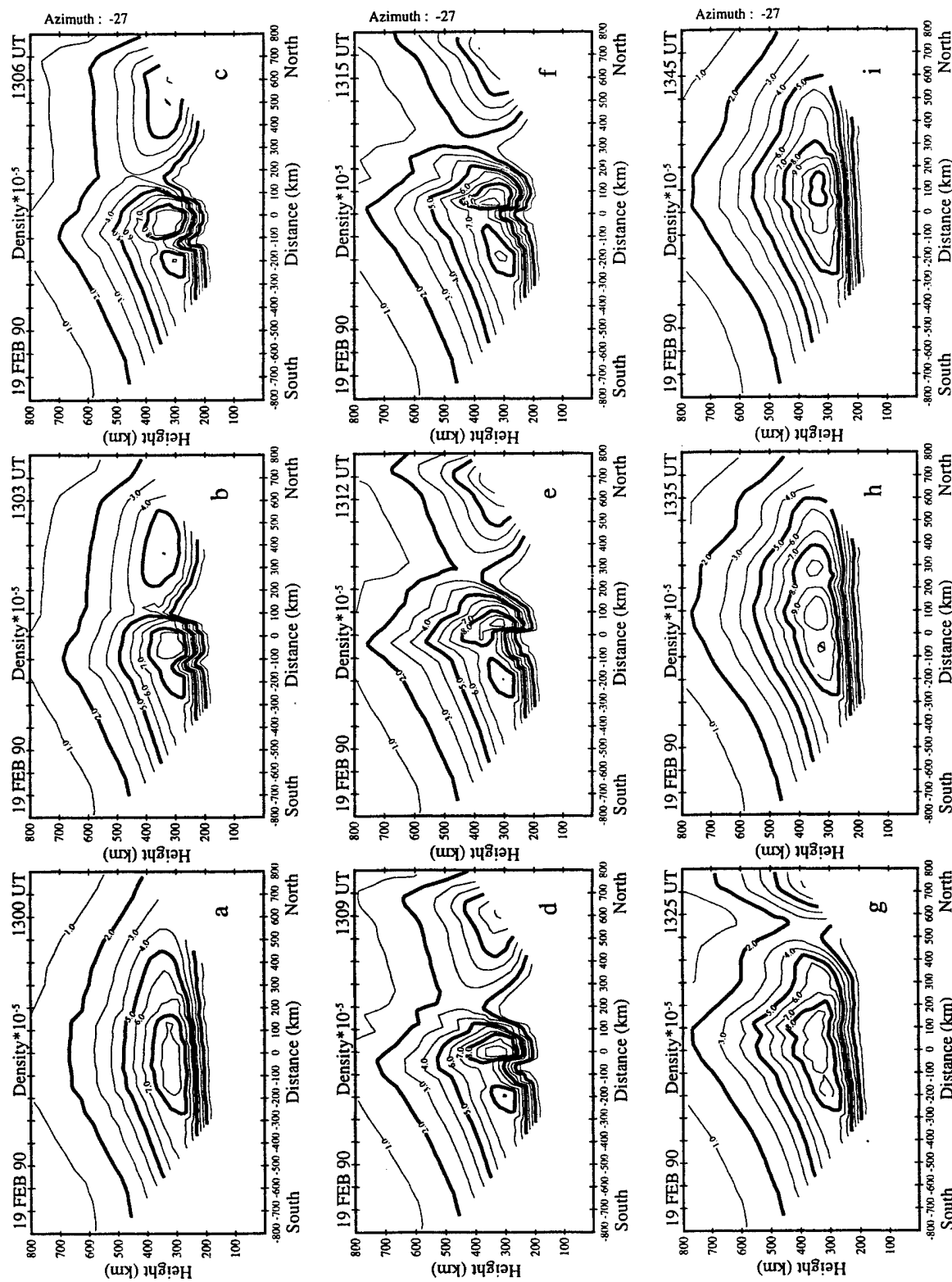


Figure 8. Same as Figure 4 but for the Heppner-Maynard convection pattern (section 3.3).

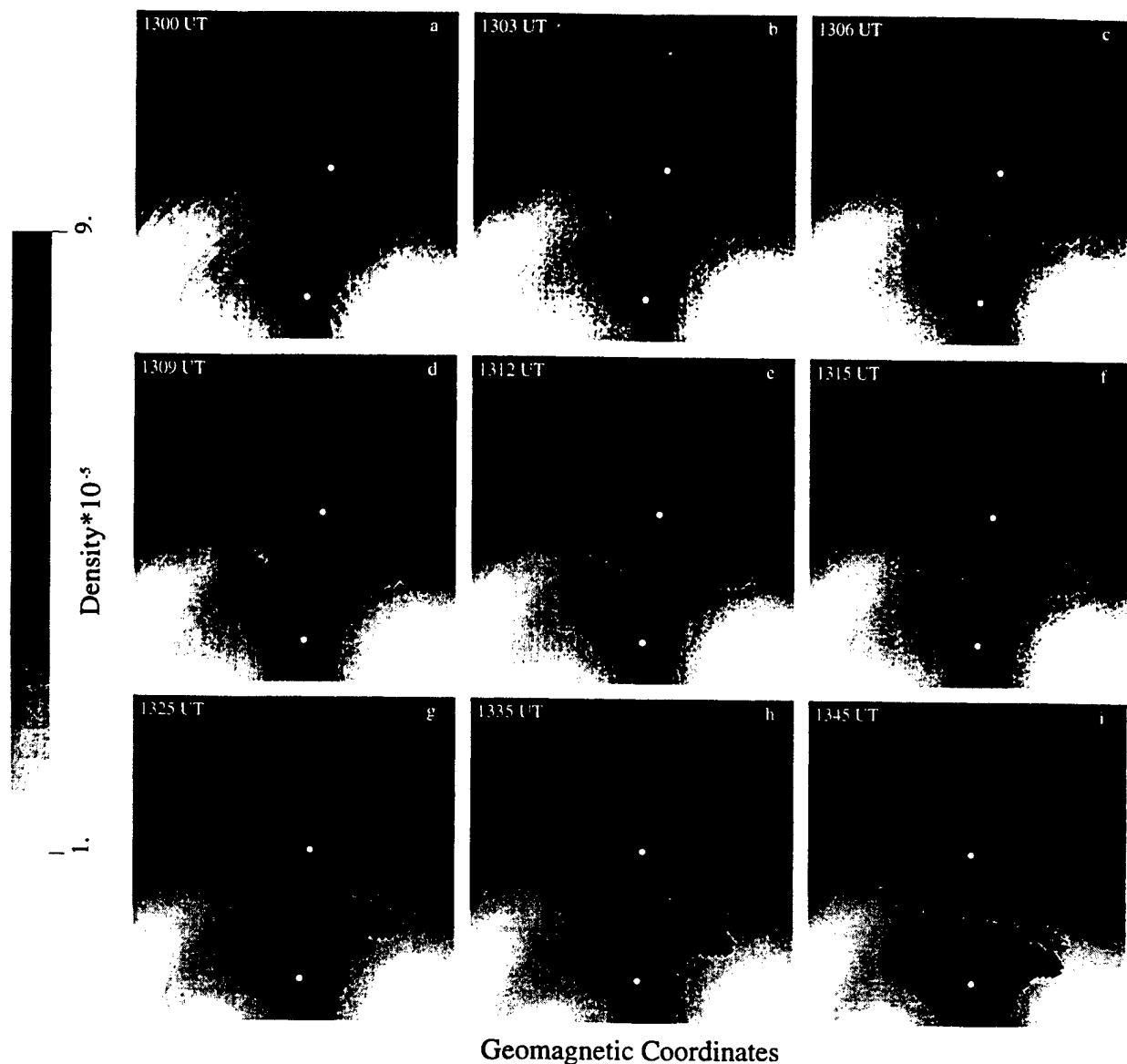


Figure 9. Same as Figure 3 but after eliminating the dependence of the ion temperature on the magnetospheric electric field (section 3.4).

3.4. Assessment of the Temperature Effect on Patch Formation

The fourth case study was performed to quantify the importance of the O^+ recombination rate in producing channels of low density. The results of this study are presented in Figure 9. In this series of simulations, we returned to the Heelis/traveling vortices scenario except we turned off the dependence of T_i on the magnetospheric electric field and hence turned off any enhanced O^+ loss

rates. The goal in this investigation was to determine quantitatively how much plasma depletion is attributed to erosion by enhancements of the O^+ loss rate and what percentage of the plasma depletion is carried from earlier local times by the vortex flow. Evidently, an eastward flow is needed in order to transport the less dense morning side plasma into the afternoon region. A flow of this type exists at the common region between the vortices.

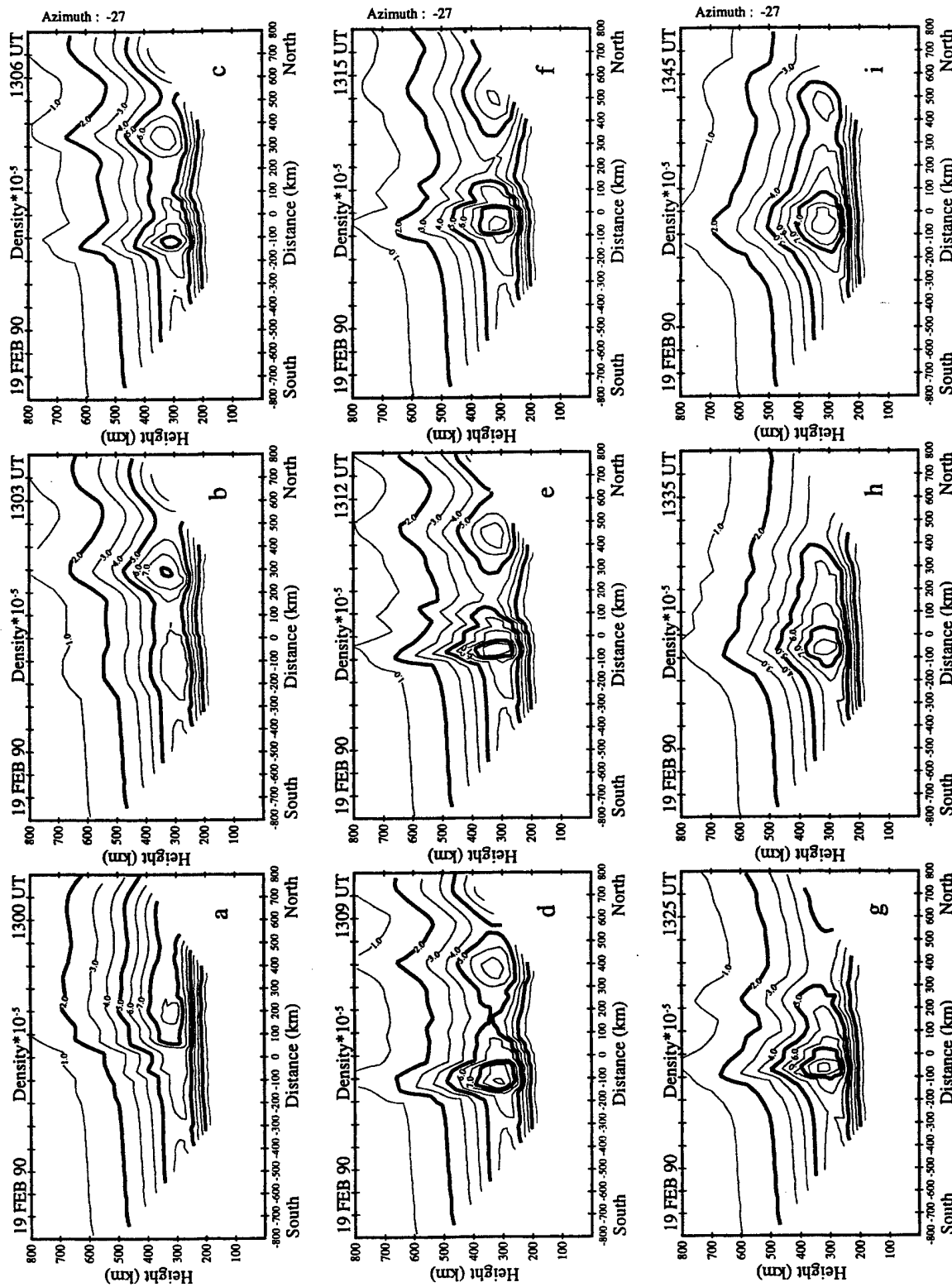


Figure 10. Same as Figure 4 but after eliminating the Ti dependence on the magnetospheric electric field.

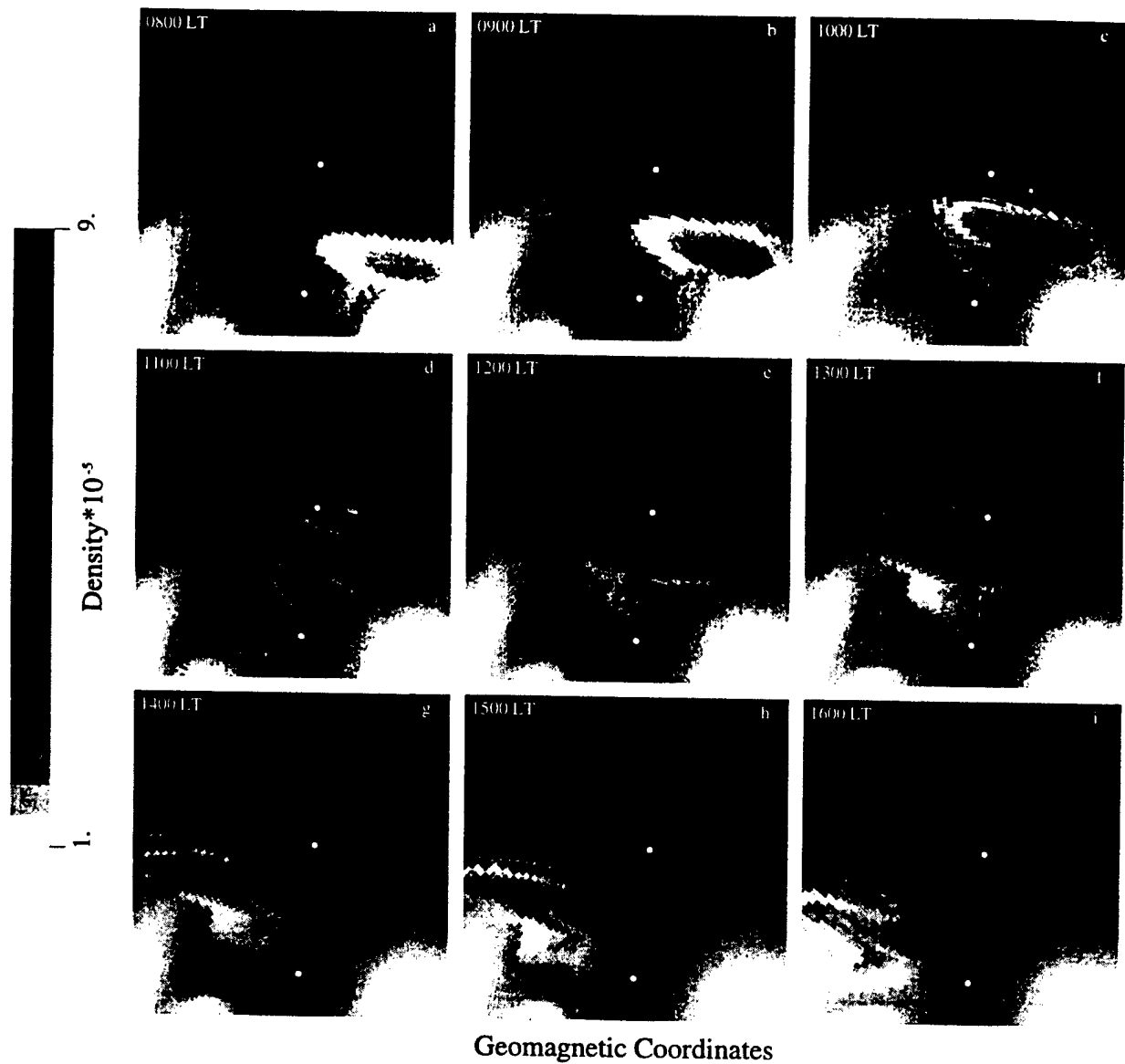


Figure 11. Same as Figure 3, but for nine different initial locations of the traveling vortices.

A comparison of Figures 9 and 5 indicates some resemblance between both figures. The structuring is also initiated with a rotation of the TOI toward a dawn-dusk alignment. Plasma from the early morning side also intrudes equatorward of the northern patch. However, there are also some prominent differences. We did not find a full separation between the N_e structure and the auroral oval, even 15 min into the simulation. There is a channel containing plasma density equal to $4 \times 10^5 \text{ cm}^{-3}$ in the afternoon side of the structure. The southern N_e

structure is absent, because at this latitude the southern vortex can only bring more dense plasma from the afternoon sector. Figure 10f indicates that the deepest depletion achieved in this simulation is $4 \times 10^5 \text{ cm}^{-3}$, while the minimum density value during the full-blown simulation was 10^5 cm^{-3} in Figure 5. Considering that the original density was $9 \times 10^5 \text{ cm}^{-3}$, then 62% of the depletion is due to convection of low-density plasma and 38% is due to erosion by the temperature-dependent loss rate.

4. Traveling Vortices at Different Local Times

In the previous section, we were concerned with the formation of patches under different patterns of global convection. In this section, we search for the preferred local time at which the vortices are more likely to generate polar cap patches.

Traveling vortices have been observed at a large variety of different local times [Friis-Christensen et al., 1988; Heikkila et al., 1989] using radar and magnetometer data. They have also been predicted on theoretical grounds [Newell and Sibeck, 1993]. They postulated an association between the presence of twin vortices and changes in the high-latitude convection patterns due to pressure pulses in the magnetosphere. In order for the vortices to produce patches, evidently, they have to develop near the TOI and have a lifetime long enough to erode a sector of the TOI. We have carried out eight additional simulations placing the vortices at different local times. The local times that were used varied from 0800 to 1600 LT. The results of this study are compiled in Figure 11. This figure compares $N_m F_2$ values obtained 15 min along the simulations (at 1315 UT) for the eight new cases and the simulation described in section 3.2. The number on the upper left corner indicates the local times at which the vortices were located at the beginning of the simulation. Only the vortices located at 1000 LT, 1100 LT and 1200 LT (Figures 11c, 11d and 11e) produce distinct patches. Vortices at 0800 LT and 0900 LT (Figures 11a and 11b) only distort the TOI and create isolated regions of low density ($2 \times 10^5 \text{ cm}^{-3}$) plasma. When these structures circulate within the polar cap, they will consist of plasma equally dense to the polar cap plasma. When the vortices were located at 1300 LT (Figure 11f), we obtained dawn-dusk elongated density traces. No detachment from the auroral oval densities was observed. The last three modeling efforts in this subsection were performed using vortices located at 1400 LT, 1500 LT and 1600 LT (Figures 11g-11i). These figures depict the formation of some kind of structuring in the afternoon cell. These structures are connected to the auroral oval and will not penetrate into the polar cap. In fact, we followed all these case simulations for another 30 min and found the structures continuously elongating in the dawn-dusk direction. These structures could certainly appear as isolated structures to digisondes or to low-orbiting satellites, but an all-sky camera properly located could possibly indicate the connection of these structures to the auroral plasma.

5. Discussion and Conclusions

Several researchers have indicated that the TOI is present at longitudes near Sondrestrom when this high-latitude station is near noon [Foster and Doupinik, 1984; Kelly and Vickrey, 1984]. Our simulation during undisturbed conditions has also demonstrated that the TOI is a prominent feature at Sondrestrom when we select a typical B_z south convection pattern. The mechanism described here requires the existence of an elongated TOI as the basic ingredient to form a patch. It also needs a large plasma jet occurring near and across the TOI. The large plasma velocity will create a region of enhanced T_e , consequently increase the O^+ recombination rate and then erode the local plasma. We found also that low-density plasma can be brought in by the vortex flow from earlier local times. This patch formation mechanism will create, in this way, sections of depleted and enhanced densities across the TOI.

The elevation scans conducted across our simulated volume demonstrated that the TOI or other structures in the polar cap could be wrongly interpreted as isolated entities (say patches). In reality, they may be connected to the auroral/subauroral plasma. We conclude that it is necessary to conduct antenna azimuthal scans or to use an all-sky camera to properly identify a polar cap patch.

Sojka et al. [1993, 1994] have used a scheme of continuous changes of the B_y component of the IMF to redirect the TOI toward the dawn or dusk sides of the polar cap. In this study, we have employed the appearance of vortices in the polar cap and their subsequent motion across the polar cap to produce polar cap patches. No repetitive changes in any of the components of the IMF were required. The proposed mechanism only needs the existence of vortices moving with the background plasma. Moreover, it was found that the convecting vortices scenario was the most favorable situation to form disconnected plasma structures inside the polar cap.

The modeled densities of Figures 6 and 8 indicated a good qualitative agreement with the data measured by the Sondrestrom ISR. The discrepancies between measured and modeled densities can be understood in terms of the initial inputs that were used in the simulations and a few of the limitations of the GTIM model. The much smaller density, seen in the depleted density region of Figure 2c, can be attributed to a much smaller density in the morning cell from where the vortices grab the low-density plasma. In fact, the Sondrestrom ISR detected values near $2 \times 10^5 \text{ cm}^{-3}$ at 1100 UT (2 hours before the

measurements reported here) that if unchanged could explain this discrepancy. The radar also measured densities above 10^5 cm^{-3} at 200 km altitude; no similar feature was reported in the simulations because of the lack of molecular ions in our simulations. The GTIM model is at the present time essentially a one-ion (O^+) model. Simulations were performed with and without particle precipitation in the auroral oval, and essentially no differences were seen in the F region. The effects of particle precipitation associated with the vortex located more equatorward where convergent electric fields existed were not included and neither were the effects of soft precipitation that can occur in the cusp/cleft and polar cap. These issues will be topics for future work.

We found that 62% of the density depletion was due to plasma being carried from earlier local times. This fact argues in favor of the ability of smaller potentials associated with the vortices to also create regions of depleted density. However, the vortex potential cannot be too small, otherwise the vortex velocity will also be small, and the time to transport low-density plasma from the morning cell will be considerably longer.

From this study we found the following:

1. Polar cap patches can be generated by traveling vortices independent of the convection pattern being used. We have used a Heelis-type and a Heppner-Maynard-type convection pattern for B_y positive and for B_y negative, respectively. An essential condition for forming well-separated patches was to allow the vortices to travel with the background global convection.

2. Enhanced recombination of O^+ contributes to the creation of a channel of low density. Equally important is the transport of low-density plasma from earlier local times. For the size and potential of the vortices that we used 38% of the depletion was attributed to the O^+ recombination loss and 62% to transport.

3. There is a preferential local time at which the vortices can generate patches. We found that this local time sector is restricted to between 1000 LT and 1200 LT.

4. The simulation presented here qualitatively agrees with the data collected at Sondrestrom on February 19, 1990 [Valladares et al., 1994b]; both exhibit the same salient features.

5. Our modeling described here postulates that the polar cap patches will intrinsically have the shape of the vortices. Circular vortices will reproduce more circular patches. Elliptical vortices, as presented here, will generate the elongated cigar-shaped patches that have been found in the polar cap [Fukui et al., 1994].

Acknowledgments. We would like to thank Ed Weber and Santimay Basu for useful discussions. The work at Boston College was partially supported by Phillips Laboratory contracts F19628-90-K-0007 and F19628-88-K-0008 and by NSF grant ATM-9404088. We thank the Danish Commission for Scientific Research in Greenland for permission to conduct ground experiments at Sondrestrom under continuing project A16-91.

References

- Anderson, D.N., Daily variation of the ionospheric F2 equatorial anomaly in the American and Asian sectors, cooperative thesis, 24 pp. 1-144, Natl. Cent. Atmos. Res., Boulder, Colo., 1971.
- Anderson, D.N., A theoretical study of the ionospheric F region equatorial anomaly, I, theory, *Planet. Space Sci.*, 21, 409, 1973.
- Anderson, D.N., J. Buchau, and R.A. Heelis, Origin of density enhancements in the winter polar cap, *Radio Sci.*, 23, 513, 1988.
- Anderson, D.N., D.T. Decker and C.E. Valladares, Modeling boundary blobs using time varying convection, *Geophys. Res. Lett.*, in press, 1996.
- Basu, Su., S. Basu, E. MacKenzie, and H.E. Whitney, Morphology of phase and intensity scintillations in the auroral oval and polar cap, *Radio Sci.*, 20, 347, 1985.
- Basu, S., Su. Basu, C.E. Valladares, E.J. Weber, J. Buchau, G.J. Bishop, and B.W. Reinisch, Coordinated observations of high latitude ionospheric turbulence, *Physics of Space Plasma* (1988), SPI Conf. Proc. Reprint Ser., 8, 137, 1989.
- Buchau, J., B.W. Reinisch, E.J. Weber, and J.G. Moore, Structure and dynamics of the winter polar cap F region, *Radio Sci.*, 18, 995, 1983.
- Buchau, J., E.J. Weber, D.N. Anderson, H.C. Carlson Jr., J.G. Moore, B.W. Reinisch, and R.C. Livingston, Ionospheric structures in the polar cap: their origin and relation to 250-Mhz scintillation, *Radio Sci.*, 20, 325, 1985.
- Carlson, H.C., V.B. Wickwar, E.J. Weber, J. Buchau, J.G. Moore, and W. Whiting, Plasma characteristics of polar cap F layer arcs, *Geophys. Res. Lett.*, 11, 895, 1984.
- Cowley, S.W.H., M.P. Freeman, M. Lockwood, and M.F. Smith, The ionospheric signature of flux transfer events, in *CLUSTER - Dayside Polar Cusp, Eur. Space Agency Spec. Publ. ESA SP-330*, 105-112, 1991.
- Crain, D.J., J.J. Sojka, R.W. Schunk, P.H. Doherty and J.A. Klobuchar, A first-principle derivation of the high-latitude total electron content distribution, *Radio Sci.*, 28, 49, 1993.
- Decker, D.T., C.E. Valladares, R. Sheehan, Su. Basu, D.N. Anderson, and R.A. Heelis, Modeling daytime F layer patches over Sondrestrom, *Radio Sci.*, 29, 249, 1994.
- de la Beaujardiere, O., J.D. Craven, V.B. Wickwar, G. Candal, J.M. Holt, L.A. Frank, L.H. Brace, D.S. Evans, and J.D. Winningham, Universal time dependence of nighttime F region densities at high latitudes, *J. Geophys. Res.*, 90, 4319, 1985.

- Foster, J.C., and J.R. Doupinik, Plasma convection in the vicinity of the dayside cleft, *J. Geophys. Res.*, **89**, 9107, 1984.
- Friis-Christensen, E., M.A. McHenry, C.R. Clauer, and S. Vennerstrom, Ionospheric traveling convection vortices observed near the polar cleft: A triggered response to sudden changes in the solar wind, *Geophys. Res. Lett.*, **15**, 253, 1988.
- Fukui, K., J. Buchau, and C.E. Valladares, Convection of polar cap patches observed at Qaanaaq, Greenland during the winter of 1989-1990, *Radio Sci.*, **29**, 231, 1994.
- Goertz, C.K., E. Nielsen, A. Korth, K.-H. Glassmeier, C. Haldoupis, P. Hoeg, and D. Hayward, Observations of a possible ground signature of flux transfer events, *J. Geophys. Res.*, **90**, 4069, 1985.
- Hedin, A.E., MSIS-86 thermospheric model, *J. Geophys. Res.*, **92**, 4649, 1987.
- Hedin, A.E., et al., Revised global model of thermosphere winds using satellite and ground-based observations, *J. Geophys. Res.*, **96**, 7657, 1991.
- Heikkila, W.J., T.S. Jorgensen, L.J. Lanzerotti, and C.G. MacLennan, A transient auroral event on the dayside, *J. Geophys. Res.*, **94**, 15291, 1989.
- Kelly, J.D., and J.F. Vickrey, *F* region ionospheric structure associated with antisunward flow near the dayside cusp, *Geophys. Res. Lett.*, **11**, 907, 1984.
- Lockwood, M., and H.C. Carlson, Production of polar cap density patches by transient magnetopause reconnection, *Geophys. Res. Lett.*, **19**, 1731, 1992.
- Ma, Z.-W., J.G. Hawkins, and L.-C. Lee, A simulation study of impulsive penetration of solar wind irregularities into the magnetosphere at the dayside magnetopause, *J. Geophys. Res.*, **96**, 15751, 1991.
- Newell, P.T., and D.G. Sibeck, B_y fluctuations in the magnetosheath and azimuthal flow velocity transients in the dayside ionosphere, *Geophys. Res. Lett.*, **20**, 1719, 1993.
- Rodger, A.S., M. Pinnock, J.R. Dudeney, K.B. Baker, and R.A. Greenwald, A new mechanism for polar patch formation, *J. Geophys. Res.*, **99**, 6425, 1994.
- Schunk, R.W., and J.J. Sojka, A theoretical study of the lifetime and transport of large ionospheric density structures, *J. Geophys. Res.*, **92**, 12343, 1987.
- Schunk, R.W., W.J. Raitt, and P.M. Banks, Effect of electric fields on the daytime high-latitude *E* and *F* regions, *J. Geophys. Res.*, **80**, 3121, 1975.
- Sojka, J.J., and R.W. Schunk, A theoretical study of the production and decay of localized electron density enhancements in the polar ionosphere, *J. Geophys. Res.*, **91**, 3245, 1986.
- Sojka, J.J., and R.W. Schunk, A model study of how electric field structures affect the polar cap *F* region, *J. Geophys. Res.*, **93**, 884, 1988.
- Sojka, J.J., M.D. Bowline, R.W. Schunk, D.T. Decker, C.E. Valladares, R. Sheehan, D.N. Anderson, and R.A. Heelis, Modeling polar cap *F* region patches using time-varying convection, *Geophys. Res. Lett.*, **20**, 1783, 1993.
- Sojka, J.J., M.D. Bowline, and R.W. Schunk, Patches in the polar ionosphere: UT and seasonal dependence, *J. Geophys. Res.*, **99**, 14959, 1994.
- Tsunoda, R.T., High-latitude *F* region irregularities: a review and synthesis, *Rev. Geophys.*, **26**, 719, 1988.
- Valladares, C.E., H.C. Carlson Jr., and K. Fukui, Interplanetary magnetic field dependency of stable sun-aligned polar cap arcs, *J. Geophys. Res.*, **99**, 6247, 1994a.
- Valladares, C.E., Su. Basu, J. Buchau, and E. Friis-Christensen, Experimental evidence for the formation and entry of patches into the polar cap, *Radio Sci.*, **29**, 167, 1994b.
- Weber, E.J., J. Buchau, J.G. Moore, J.R. Sharber, R.C. Livingston, J.D. Winningham, and B.W. Reinisch, *F* layer ionization patches in the polar cap, *J. Geophys. Res.*, **89**, 1683, 1984.
- Weber, E.J., J.A. Klobuchar, J. Buchau, H.C. Carlson, Jr., R.C. Livingston O. de la Beaujardiere, M. McCready, J.G. Moore, and G.J. Bishop, Polar cap *F* layer patches: structure and dynamics, *J. Geophys. Res.*, **91**, 121, 1986.

D.N. Anderson, Phillips Laboratory, Geophysics Directorate (GPIM), 29 Randolph Rd., Hanscom AFB, MA 01730-3010. (e-mail: danderson@plh.af.mil)

D.T. Decker, R. Sheehan, and C.E. Valladares, Institute for Scientific Research, Boston College, 885 Centre St., Newton, MA 02159. (e-mail: decker@plh.af.mil; sheehan@plh.af.mil; cesar@dlws7.bc.edu)

(Received August 8, 1995; revised February 8, 1996; accepted February 14, 1996.)

Collisional degradation of the proton-H atom fluxes in the atmosphere: A comparison of theoretical techniques

Dwight T. Decker,¹ Boris V. Kozelov,² B. Basu,³ J. R. Jasperse,³ and V. E. Ivanov²

Abstract. Three methods for calculating the transport of energetic protons and hydrogen atoms within the Earth's atmosphere are compared. The methods are (1) a Monte Carlo (MC) simulation, (2) a discrete energy loss solution to the linear transport equations, and (3) a continuous slowing-down approximation (CSDA). In the calculations performed, all three models use the same cross sections, three-component (N_2 , O_2 , O) neutral atmosphere, and incident isotropic Maxwellian proton fluxes of various characteristic energies (1–20 keV). To ensure that all three methods include the same physical processes, the effects of magnetic mirroring and the lateral spreading of particles are “turned off” in the MC simulations as these processes are not included in the present linear transport or CSDA models. A variety of quantities are calculated and compared including energy deposition rates, eV/ion pair, hemispherically averaged differential fluxes of protons and H atoms, energy integrated differential fluxes, and total proton and H atom fluxes. The agreement between all three models is excellent except at the lowest altitudes. Apart from these altitudes, the differences that do exist are small compared to the errors that generally result from poorly known inputs and compared to the typical errors quoted for geophysical observations. The altitudes where the results do differ significantly are where the proton and H atom fluxes are severely attenuated and are below the altitudes where the bulk of the energy deposition and ionization takes place. The success of these comparisons suggests that our ability to model actual observations is presently limited by uncertainties in cross sections and the lack of suitable observations rather than our ability to solve the equations that describe the known physics of proton-H atom transport.

1. Introduction

It is well established that an essentially permanent feature of the Earth's high-latitude atmosphere is the presence of auroral particle fluxes. It is also well known that these precipitating fluxes from the magnetosphere consist of mostly electrons and protons with a small admixture of other ions. Early ground-based optical observations [Romick and Elvey, 1958; Galperin, 1959] indicated that electron and proton aurora could have separate latitudinal distributions. Later satellite observations of the precipitating particles established that statistically the electron and protons precipitate within

two ovals that are not colocated [Sharber, 1981; Hardy et al., 1989]. Further, an examination of the Hardy statistical models [Hardy et al., 1987, 1991] reveals that in the afternoon and evening sectors the ions at the lower auroral latitudes can carry a significant portion of the incoming energy flux. Thus, in order to study the dissipation of auroral energy within the Earth's atmosphere, it is necessary to study not just the transport and collisional degradation of energetic electrons but also those of protons.

The transport of energetic protons within matter is a problem that has been studied for a variety of physical situations. In the case of transport of auroral protons within the atmosphere there are several features that add to the difficulty of the problem. Some of those features are (1) auroral proton energies can be less than the energy of the maximum of the ionization cross section, (2) there is a large gradient of the atmospheric density with respect to altitude, and (3) the Earth's magnetic field is present. The first feature requires detailed knowledge of cross sections since simple estimations (Born approximation) of cross sections are not valid. Further, at auroral energies the charge chang-

¹Institute for Scientific Research, Boston College, Newton, Massachusetts.

²Polar Geophysical Institute, Apatity, Russia.

³Phillips Laboratory, Hanscom Air Force Base, Massachusetts.

ing processes have to be included and this introduces energetic hydrogen (H) atoms into the problem. The effect of the large gradient in the atmosphere is to create a strong altitude dependence in the mean free path of the protons and H atoms. Hence the behavior of the particle flux is highly dependent on altitude. The presence of the Earth's magnetic field acts to cause the protons to follow field lines into the ionosphere. However, the H atoms are not constrained by the magnetic field. This coupled with the altitude-dependent mean-free path results in a lateral spreading of the p-H flux at high altitudes but essentially no spreading at low altitudes. Finally, a feature that can be a useful simplification in any modeling is that all the collision processes involving protons and H atoms are strongly peaked in the forward direction. However, at very low energies ($E < 1$ keV) energy loss due to elastic collisions does become significant.

There have been several treatments of p-H transport that have appeared in the literature. They can be generally categorized as range theoretic, continuous slowing down, linear transport theoretic, and Monte Carlo. The range theoretic method is based on laboratory measurements of range energy relations for protons in air or its theoretical approximations and has been used in the works of *Eather and Burrows* [1966], *Eather* [1967, 1970], *Isaev and Pudovkin* [1972], *Henriksen* [1979], and *Rees* [1982]. The continuous slowing-down approximation (CSDA) uses more detailed information about scattering processes and was used for the auroral proton problem by *Edgar et al.* [1973, 1975]. Work on analytic estimations of lateral spreading of p-H flux [*Johnstone*, 1972; *Iglesias and Vondrak*, 1974] also can be classified as using the CSDA.

In more recent years, linear transport (LT) theory has been used to solve for the auroral proton and H atom fluxes. In the work of *Jasperse and Basu* [1982] the coupled transport equations based on the Boltzmann equation were solved analytically, and in a follow-up paper [*Basu et al.*, 1987], theoretically calculated electron density profiles due to incident protons were found in good agreement with Chatanika radar data. This in turn was followed by the development of a fully numerical code for solving the linear transport equations [*Basu et al.*, 1990].

The Monte Carlo (MC) method has been applied to the auroral proton problem by *Davidson* [1965], *Ponomarev* [1976], *Galperin et al.* [1976], and *Kozelov and Ivanov* [1992]. Most recently, *Kozelov* [1993] has implemented the method using a full three species neutral atmosphere and the influence of the Earth's magnetic field. While computationally intensive the Monte Carlo method does have the advantage of including processes, such as beam spreading or mirroring, that are difficult to treat in the other approaches.

Assessing the validity of any approach usually involves either "back of the envelope" estimates of neglected processes, a posteriori calculations of those processes, comparisons to observations, or comparisons to alternative approaches. The difficulty in comparing approaches is that when comparing to results of other

authors there are often differences in cross sections, boundary conditions, and geophysical conditions that confuse the issue of comparing methods. MC and CSDA models with the same input parameters were compared by *Porter and Green* [1975], but the comparison was only for homogeneous molecular nitrogen, and the initial proton flux was taken as isotropic and monoenergetic with initial energy 1 keV. More extensive comparisons for a N_2 atmosphere were made by *Kozelov and Ivanov* [1992]. They considered initial energies from 1 keV to 1 MeV. For initial energies less than 10 keV, differences were found near the high-altitude boundary and at lowest altitudes of penetration.

The purpose of this paper is to compare three methods for calculating the transport and collisional degradation of energetic protons and H atoms in the Earth's ionosphere using identical cross sections, boundary conditions, and geophysical conditions. We will show that for several quantities the differences between the three methods are reasonably small compared to the model uncertainties that arise from uncertainties in the required inputs (cross sections, neutral densities, and boundary conditions) and the uncertainties in the available observations (particle fluxes, optical emissions, and ion densities). The three methods considered are the CSDA, LT, and MC. In section 2 we briefly describe the three models used. A more detailed discussion of the relationship between the CSDA and LT models is given in an appendix. After a discussion in section 3 concerning the physical processes and input parameters included in all three models, we present in section 4 the comparison of the various results from the models. The paper concludes with a discussion and summary in section 5.

2. Description of Theoretical Models

2.1. Continuous Slowing-Down Approximation

The continuous slowing-down approximation (CSDA) describes the degradation of the energetic particle's energy in terms of loss functions. For a monoenergetic monodirectional p-H flux the equation for energy loss is given by

$$\mu \frac{dE}{dz} = - \sum_{\alpha} n_{\alpha}(z) \times \frac{[L_{\alpha,P}(E)\Phi_P(z, E, \mu) + L_{\alpha,H}(E)\Phi_H(z, E, \mu)]}{\Phi_P(z, E, \mu) + \Phi_H(z, E, \mu)} \quad (1)$$

where Φ values are the energetic particle fluxes, z is the altitude, μ is cosine of the pitch angle, and $n_{\alpha}(z)$ are the densities for neutral specie α . $L_{\alpha,P}(E)$ and $L_{\alpha,H}(E)$ are the loss functions for the protons and H atoms due to collisions with neutral gases and are given by

$$L_{\alpha,P}(E) = \sum_j W_{\alpha,P}^j(E) \sigma_{\alpha,P}^j(E) \quad (2)$$

$$L_{\alpha,H}(E) = \sum_j W_{\alpha,H}^j(E) \sigma_{\alpha,H}^j(E) \quad (3)$$

where $\sigma_{\alpha,p}^j(E)$ is the cross section for a type j collision between a proton and a neutral species α and $W_{\alpha,p}^j(E)$ is the corresponding energy loss. Similarly, $\sigma_{\alpha,H}^j(E)$ and $W_{\alpha,H}^j(E)$ are the cross sections and the energy loss for collisions involving H atoms.

Usually, the loss function is defined for a charge state equilibrium flux [Porter and Green, 1975]. Here, in an implementation developed by one of us (B.V.K.), the loss function is defined using the nonequilibrium flux that describes the modification of the flux charge state composition. The nonequilibrium flux is calculated using the following equations:

$$\mu \frac{d\Phi_P(z, E, \mu)}{dz} = \Phi_H(z, E, \mu) \sum_{\alpha} n_{\alpha}(z) \sigma_{\alpha}^{01}(E) - \Phi_P(z, E, \mu) \sum_{\alpha} n_{\alpha}(z) \sigma_{\alpha}^{10}(E) \quad (4)$$

$$\frac{d\Phi_H(z, E, \mu)}{dz} = - \frac{d\Phi_P(z, E, \mu)}{dz} \quad (5)$$

where σ^{10} and σ^{01} are the total cross sections for charge exchange and stripping respectively. The calculational procedure consists of solving (1), (4), and (5) on a altitude, energy and pitch angle grid with the incoming flux at the high-altitude boundary being approximated by a set of monoenergetic monodirectional particle streams. A more detailed discussion of the CSDA can be found in the appendix.

2.2. Linear Transport Model

The fundamental feature of the linear transport (LT) model is the use of transport theoretic methods to solve two coupled Boltzmann equations for the proton and H atom differential fluxes. In solving these equations, we assume steady state conditions, no electric fields, a uniform geomagnetic field (no magnetic mirroring), and azimuthal symmetry about the geomagnetic field line. The collisional processes included are the various types of collisions between the energetic precipitating particles and the neutral constituents of the ionosphere. The protons and H atoms are coupled to each other by charge-changing collisions with neutrals (charge exchange and stripping). The two transport equations, discussions of the various collision processes, and the numerical methods for solving the equations can be found in the work of Basu et al. [1993] and will not be given here. A discussion of the relationship between the linear transport theory and the CSDA can be found in the appendix.

2.3. Monte Carlo Model

The Monte Carlo (MC) model uses a "collision-by-collision" algorithm which is based on simulating the individual trajectories of a large number of protons and H atoms. The "history" of each particle is represented as a series of collisions that are separated by segments of free streaming within a magnetic field. The selection of the path length between collisions and the collisional parameters is made by mapping into a random number ξ generated uniformly in the range 0-1.

The altitude of the particle after the $(i+1)^{st}$ path length is determined from the formula

$$-\ln \xi = \int_{z_i}^{z_{i+1}} \frac{dz}{\mu} \sum_{\alpha} n_{\alpha}(z) \sigma_{\alpha,\beta}^{\text{tot}}(E_i), \quad (6)$$

where z_i is the altitude before the $(i+1)^{st}$ path length, $\sigma_{\alpha,\beta}^{\text{tot}}(E_i)$ is the total cross section of the particle in gas α , E_i is the particle's energy after the i^{th} collision, β is the charge state of the particle (p or H). The neutral species with which the $(i+1)^{st}$ collision occurred are determined by random sampling using the probabilities $n_{\alpha}(z)/\sum_{\alpha} n_{\alpha}(z)$, where α is N₂, O₂, or O. The type of collision is also selected by random sampling using probabilities $\sigma^j(E_i)/\sigma^{\text{tot}}(E_i)$, where j is the type of collision. When a collision occurs, the energy of the particle is decreased based on the type of collision used. In the case of charge exchange or stripping collisions the charge state of the particle is modified. To simulate an initial Maxwellian energy distribution at the high-altitude boundary, we divide the full energy range into 10-12 energy channels and place within each channel 8000 to 24,000 protons. The cosine of the initial pitch angle for each particle is determined from the expression $\mu = \cos \theta = \sqrt{\xi}$, where ξ is a random number generated uniformly in the range 0-1. During the simulation of a particle's trajectory its location is stored along with the various quantities needed for determining such quantities as the particle fluxes, energy deposition, and ionization rates. The results of the simulation are processed by statistical methods. If we have N realizations of a random variable x , then the average value is taken as $\bar{x} = (1/N) \sum_{i=1}^N x_i$. The statistical error Δx is estimated from expressions

$$\Delta x = C \sqrt{Dx}, \quad Dx \approx \frac{1}{N} \sum_{i=1}^N (x_i - \bar{x})^2,$$

where x is the random value, x_i is the i^{th} realization of the value, Dx is the dispersion. If $C \approx 1.4$, then the probability that the value $x \in [\bar{x} - \Delta x, \bar{x} + \Delta x]$ is equal to 0.7.

3. Inputs

In order to facilitate our comparison, we wanted to make the geophysical inputs, the microscopic parameters, and the physical processes included in the three models as identical as possible. Considering the physical processes, we find that all three models include the transport and degradation of protons and neutral hydrogen atoms as they collide with the neutral species of the ionosphere. On one hand, the CSDA and LT assume a uniform magnetic field (no mirroring) and a plane parallel geometry (no spreading), on the other hand the MC method can handle the effects of magnetic mirroring as well as lateral spreading of the energetic particles. For these comparisons, magnetic mirroring and lateral spreading were turned off in the MC calculations. Similarly, both CSDA and LT assume forward scattering,

while MC can include angular scattering. Again, we simplify the MC model and use the forward scattering approximation in all calculations for this paper.

By microscopic parameter we are referring to the various cross sections and energy losses that are needed by the models. The MC and CSDA use a more extensive set than is used by the LT model. While what cross sections are used can have serious impact when comparing to observations, the critical point here is to have all three models use the same set. We chose to use the simpler LT set as described by *Basu et al.* [1993]. The one exception is that for the average energy of the ejected electron in the stripping process we use the same expression as is used for the ionization process. This was done simply as a convenience for making the comparison between the three models.

Finally, let us turn to what we call the geophysical conditions, that is, the neutral atmosphere and the incoming particle flux. The neutral atmospheric densities (N_2 , O_2 , and O) and the neutral temperature as a function of altitude are obtained from the mass spectrometer/incoherent scatter (MSIS-86) neutral atmosphere model [Hedin, 1987]. The MSIS-86 parameters used were an $F10.7$ and a 81-day averaged $F10.7$ value of 150, a daily A_p of 20, a geographic latitude of 65° N, a longitude of 35° E, a local solar time of 24, and a date of December 16, 1993. All calculations have a boundary altitude at 700 km and an incident isotropic proton flux that has a Maxwellian energy distribution.

4. Results

Calculations were made using the models for a range of Maxwellian characteristic energies (1-20 keV) and an incident energy flux of $0.5 \text{ ergs cm}^{-2}\text{s}^{-1}$. The results in all cases were similar so we will present detailed comparisons for just one case: a characteristic energy of 8

keV and a minimum energy of 500 eV. In Figures 1a-1f, we show the hemispherically averaged differential flux for the protons and H atoms at several selected altitudes. In this and in the following figures, the CSDA results are given by the dotted curves, the LT by the dashed curves and the MC by either squares or error bars. The statistical error in the MC results is either indicated by the error bars or is smaller than the size of the square symbols used in the plots. At 550 km, 150 km below the boundary altitude, we see that the proton energy distributions from all three models are in excellent agreement. Likewise, the H atom plot shows excellent agreement, though the MC simulation is a bit "noisy" because of the lack of particles as the H atom flux builds up from a starting value of zero at the boundary. At 250 km (Figure 1b) the agreement remains excellent between all three models. While the shape of the spectra are little changed, the H atom flux has continued to increase at the expense of the proton flux. Descending further to 152 km (Figure 1c), we see that the low-energy part of the spectra have filled in as particles cascade down from higher energies. The MC shows a little more noise at the lowest energies, but the agreement remains fairly good between all models. Dropping to lower altitudes, the low-energy portion of the spectra continue to increase and with the three models still in reasonable agreement reach a maximum around 118 km (Figure 1d). Though we do see a clear separation between the CSDA and LT results at lower energies. At 110 km (Figure 1e), the magnitude of the spectra at all energies have decreased and the CSDA and LT continue to show a clear separation. Finally, just 4 km lower at 106 km (Figure 1f), the CSDA and LT are showing larger differences, and the error in the MC results have grown to the point that it is difficult to decide if it agrees more with the CSDA or the LT model.

Having considered the energy distribution of the par-

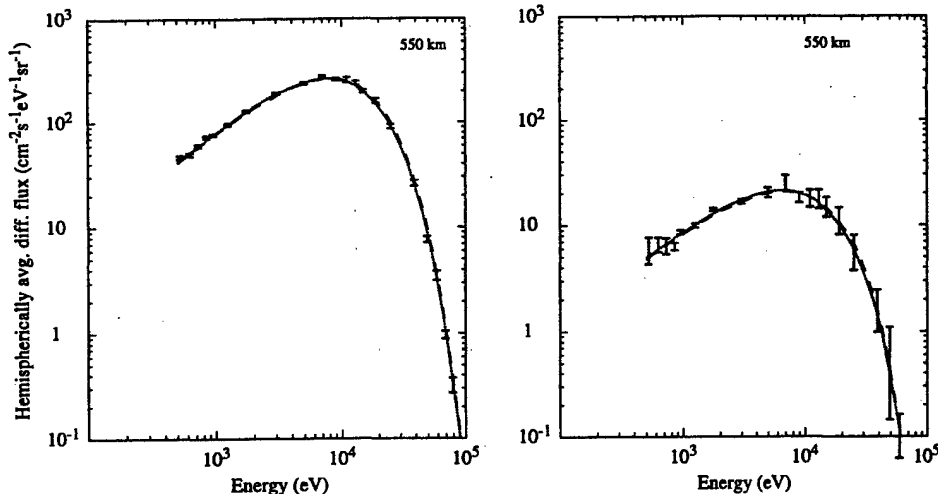


Figure 1a. Hemispherically averaged (left) proton and (right) hydrogen atom fluxes versus energy at an altitude of 550 km. The error bars are the Monte Carlo results, the long dashes are the linear transport results, and the dotted curves are the results from the continuous slowing-down approximation. The incident proton flux is a Maxwellian with a characteristic energy of 8 keV and a total incident energy flux of $0.5 \text{ ergs cm}^{-2}\text{s}^{-1}$.

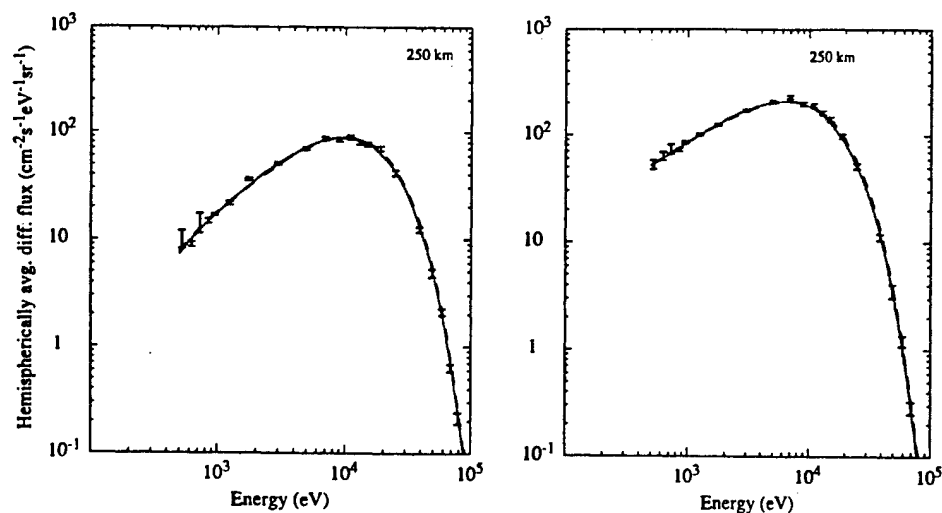


Figure 1b. Same as Figure 1a for an altitude of 250 km.

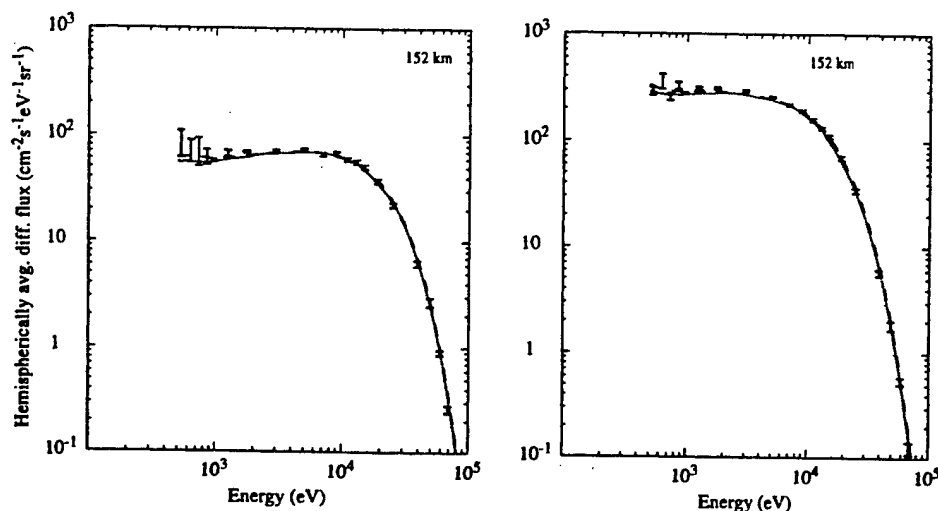


Figure 1c. Same as Figure 1a for an altitude of 152 km.

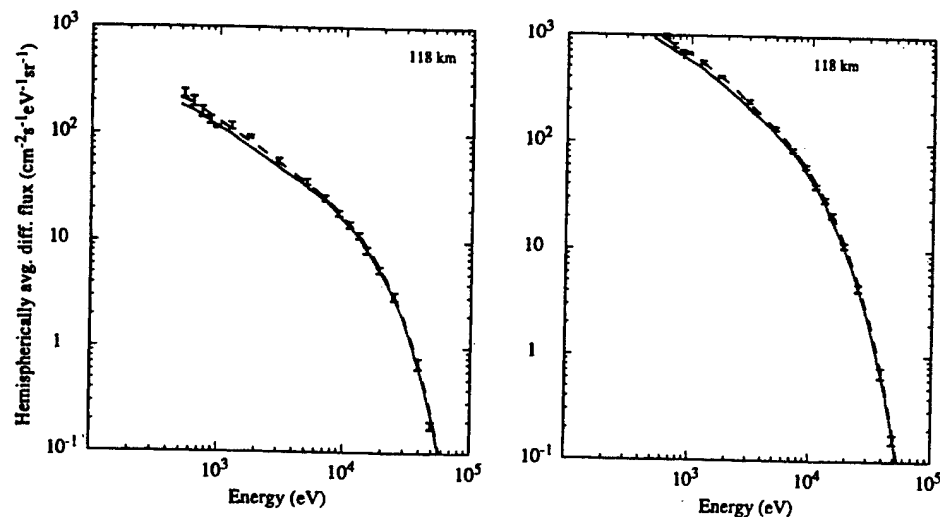


Figure 1d. Same as Figure 1a for an altitude of 118 km.

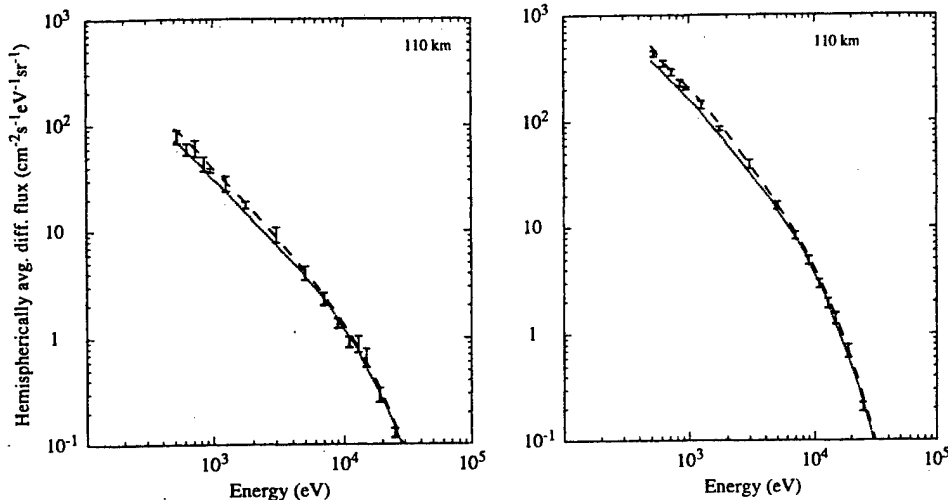


Figure 1e. Same as Figure 1a for an altitude of 110 km.

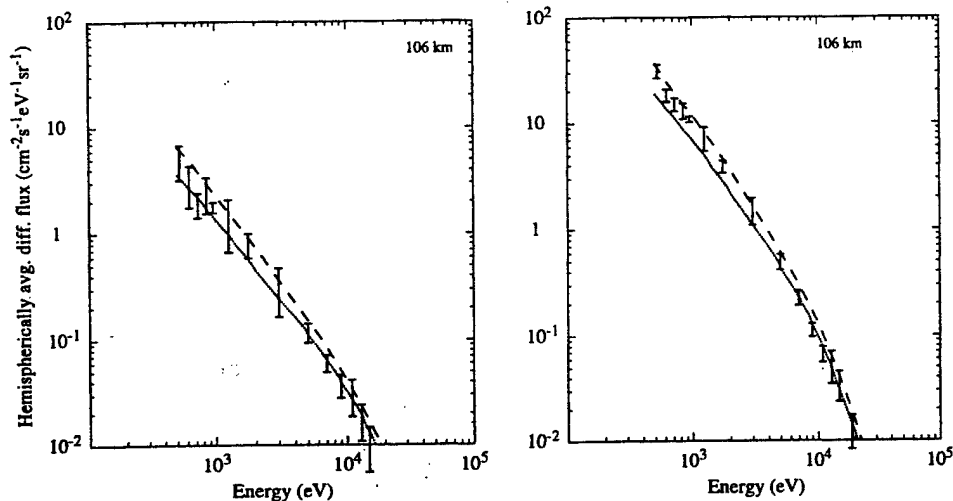


Figure 1f. Same as Figure 1a for an altitude of 106 km.

ticle fluxes averaged over pitch angle, let us now turn to plots (Figures 2a-2g) of the differential flux integrated over energy versus the cosine of the pitch angle. At 670 km (Figure 2a), we see an isotropic proton flux with all three models in excellent agreement and a much smaller H atom flux that has had only 30 km to build up from zero flux at the boundary. The H atom flux is largest near 90° pitch angle where the protons have undergone the greatest number of collisions. Figures 2b and 2c illustrate the buildup of the H atom flux at lower altitudes. At 550 km, we see the buildup is still largest at pitch angles near 90°, though by 250 km the pitch angle distributions for both protons and H atoms are isotropic. Through this range of altitudes the models have remained in excellent agreement. At 250 km the MC proton result is low compared to the CSDA and LT for the pitch angle nearest to 90° (cosine = -0.05). This difference is apparently from a slight numerical oscillation in the altitude dependence of the MC results for this particular pitch angle. Down at 152 km (Figure

2d), the fluxes remain isotropic and the models remain in good agreement except near 90° where significant fall off of the flux is observed. The CSDA shows the largest decrease followed by the LT and then the MC results. By 118 km (Figure 2e), the results at pitch angles closer to 90° are showing large decreases in the fluxes as well as some separation between the models. On the other hand, nearer to 180°, the fluxes are still large and all three models remain in good agreement. As was seen earlier, when there is a significant reduction in the flux, it is the CSDA which shows the greatest decrease. At any particular pitch angle, the LT and MC models remain in reasonable agreement until the flux has decreased about 3 orders of magnitude from what it was at higher altitudes. At 110 km (Figure 2f), some separation between models is occurring at all pitch angles and by 106 km (Figure 2g) both the CSDA and MC results are clearly falling below those of the LT model.

In Figures 3a and 3b, we show the energy integrated differential flux at one pitch angle (cosine = -0.95) as

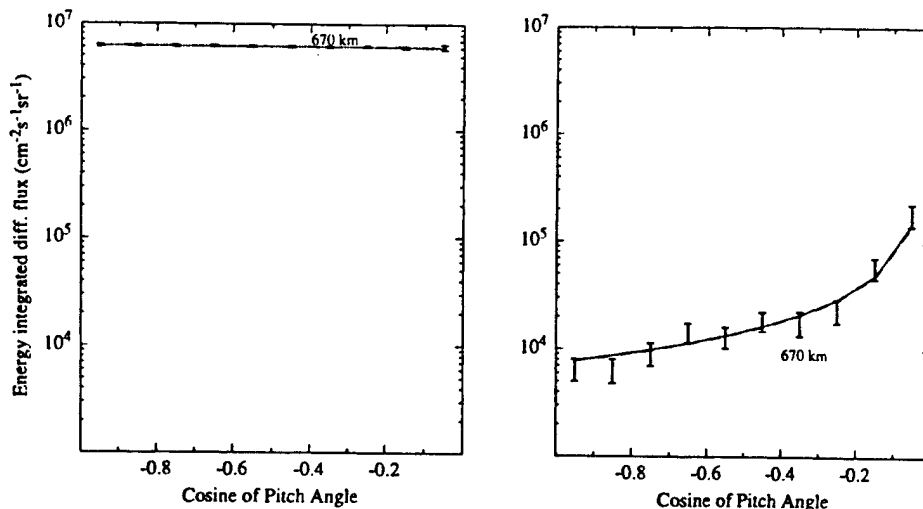


Figure 2a. The differential flux integrated over energy versus the cosine of the pitch angle for (left) protons and (right) hydrogen atoms at an altitude of 670 km. The error bars are the Monte Carlo results, the long dashes are the linear transport results, and the dotted curves are the results from the continuous slowing-down approximation. The incident proton flux is a Maxwellian with a characteristic energy of 8 keV and a total incident energy flux of 0.5 ergs cm⁻²s⁻¹.

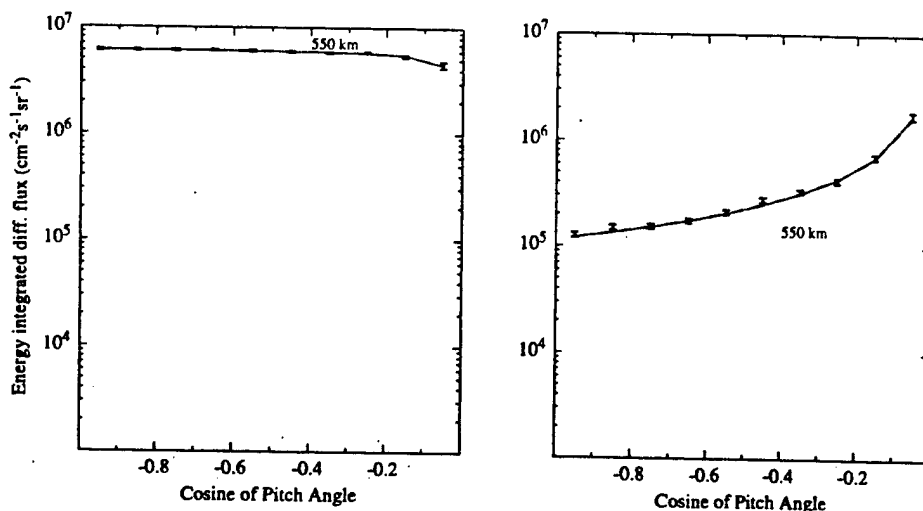


Figure 2b. Same as Figure 2a for an altitude of 550 km.

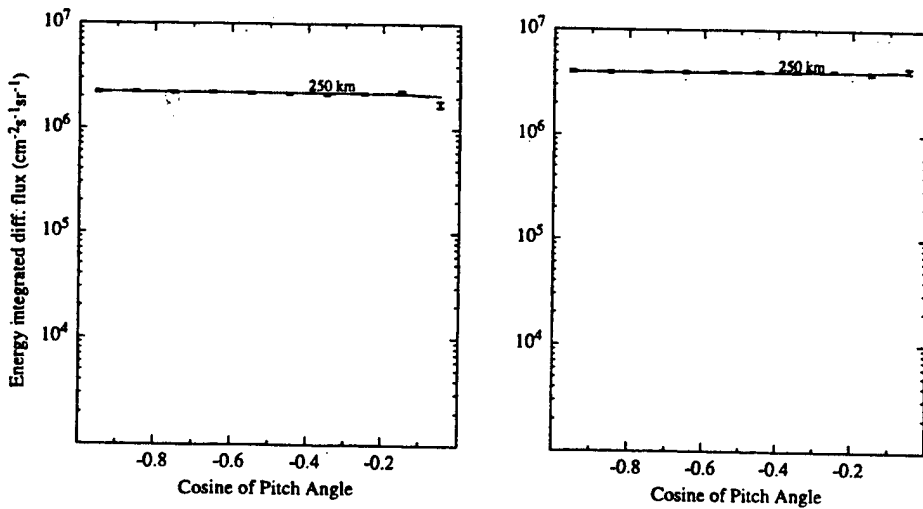


Figure 2c. Same as Figure 2a for an altitude of 250 km.

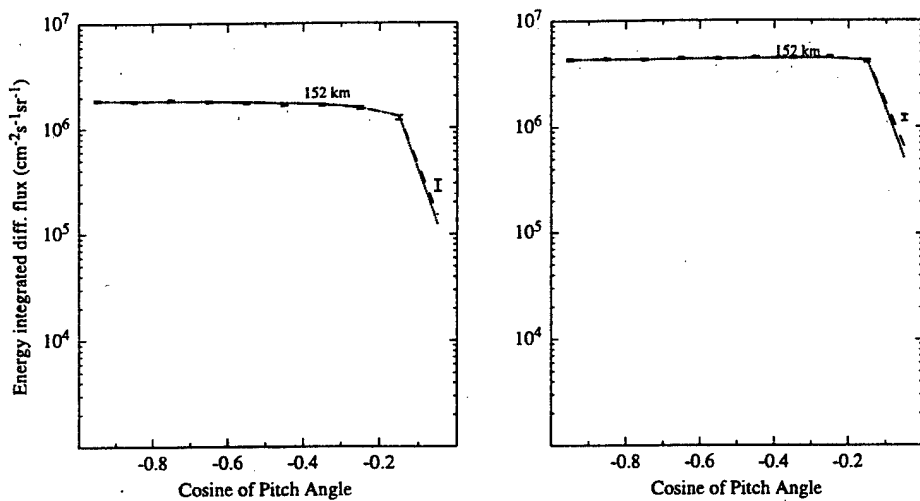


Figure 2d. Same as Figure 2a for an altitude of 152 km.

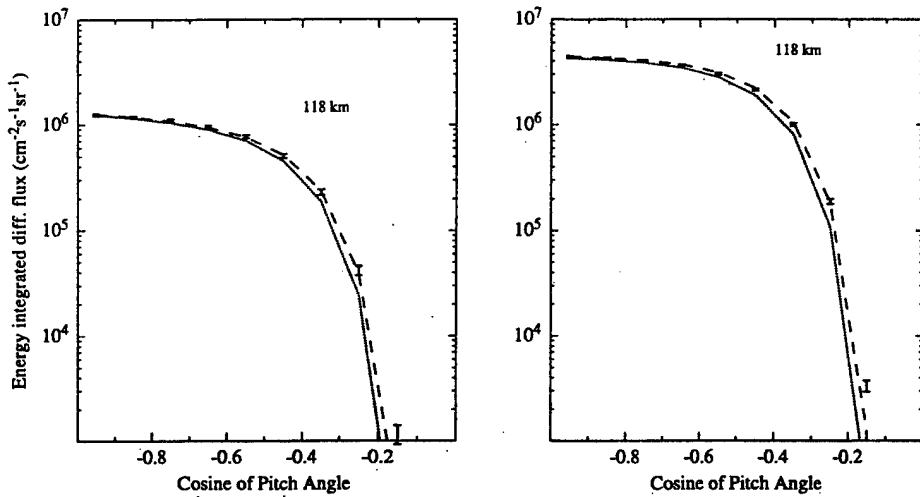


Figure 2e. Same as Figure 2a for an altitude of 118 km.

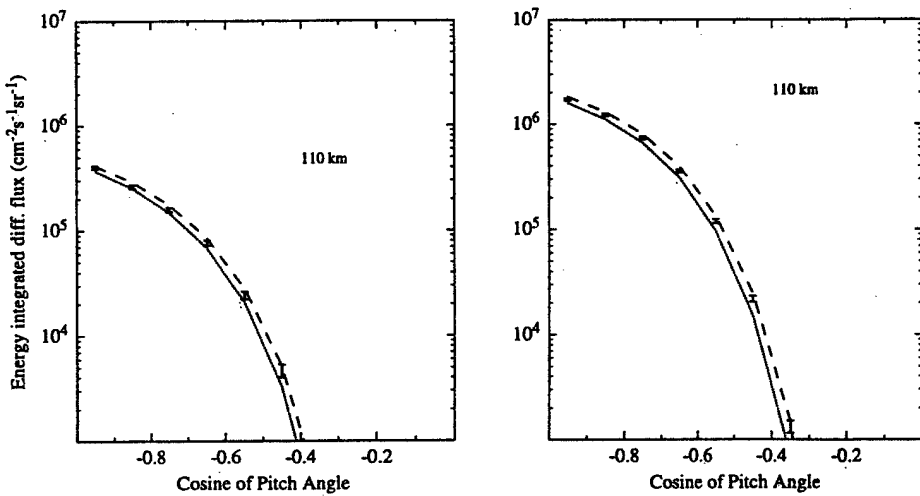


Figure 2f. Same as Figure 2a for an altitude of 110 km.

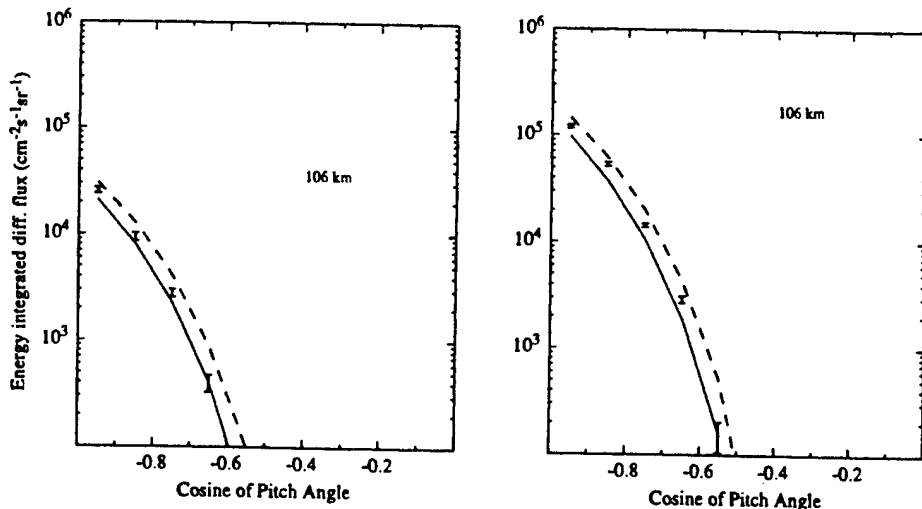


Figure 2g. Same as Figure 2a for an altitude of 106 km.

a function of altitude. As before, we see that all three models are in excellent agreement until they reach the lowest altitudes where the fluxes are severely attenuated. Similar plots for other pitch angles show the same trend with the altitude of severe flux attenuation moving higher as a pitch angle of 90° is approached. As seen above, at all pitch angles except one the LT model penetrates slightly deeper into the atmosphere than the CSDA and MC models. The one exception is the angle nearest 90° (cosine = -0.05) where the MC penetrates deeper than the CSDA and LT.

Given the excellent agreement between the differential fluxes, similar agreement is expected between vari-

ous integrals over the fluxes. In Figure 4 we show the hemispherically averaged total flux from all three models and again see excellent agreement. Figures 5a and 5b show the energy deposition rates where the LT and CSDA models agree to within 5% and both generally fall within the MC errors. Again at the lowest altitudes (below the peak of the deposition) we see that the LT model penetrates slightly deeper (less than 1 km) into the atmosphere than does the CSDA or MC model. Finally, in Figure 6, we show the eV/ion pair for various characteristic energies and see excellent agreement (within 1.5%) between all three models.

5. Discussion and Summary

We have shown that except at the lowest-altitudes three models for proton-H atom transport are in excellent agreement. The differences between the models are generally smaller than the errors that can arise from poorly known cross sections and/or the errors typi-

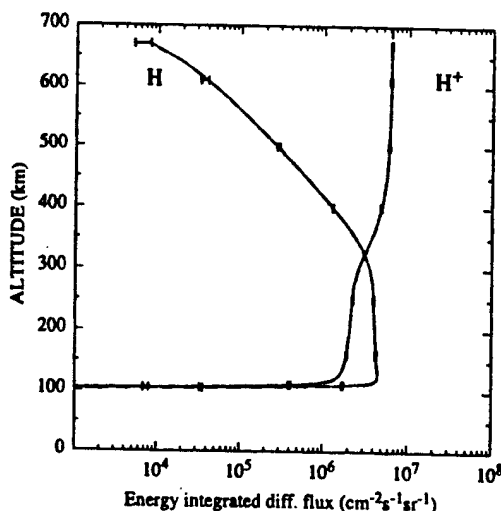


Figure 3a. The differential flux integrated over energy versus altitude for protons (H^+) and hydrogen atoms (H) at a pitch angle of 161.8° (cosine = -0.95). The error bars are the Monte Carlo results, the long dashes are the linear transport results, and the dotted curves are the results from the continuous slowing-down approximation. The incident proton flux is a Maxwellian with a characteristic energy of 8 keV and a total incident energy flux of $0.5 \text{ ergs cm}^{-2}\text{s}^{-1}$.

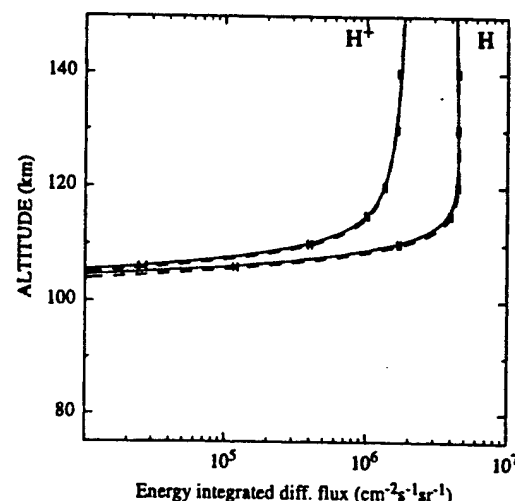


Figure 3b. Same as Figure 3a with expanded scale at lower altitudes.

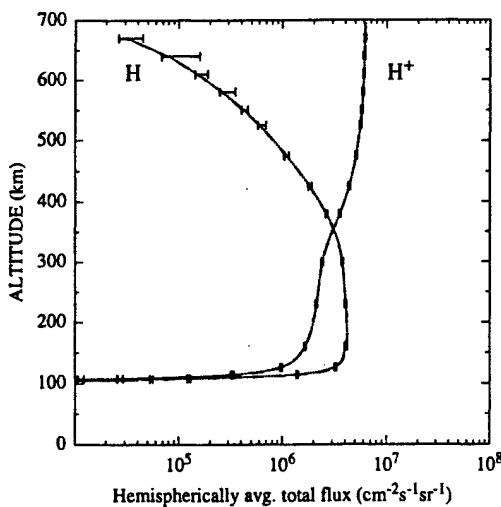


Figure 4. Hemispherically averaged total flux versus altitude for protons (H^+) and hydrogen atoms (H). The incident proton flux is a Maxwellian with a characteristic energy of 8 keV and a total incident energy flux of $0.5 \text{ ergs cm}^{-2}\text{s}^{-1}$.

cally quoted for geophysical observations. For example, the measured cross sections for proton/H atom collisions with N_2 and O_2 have quoted accuracies of typically $\pm 20 - 30\%$. For most collisions involving atomic oxygen, there are no measurements and one resorts to "estimates" based on other cross sections. One exception is for charge changing collisions for which measurements have been made with quoted accuracies of 25%, but at present there are still factors of 2 disagreement between some of these measurements. Such uncertainties can lead to errors of comparable magnitude in the

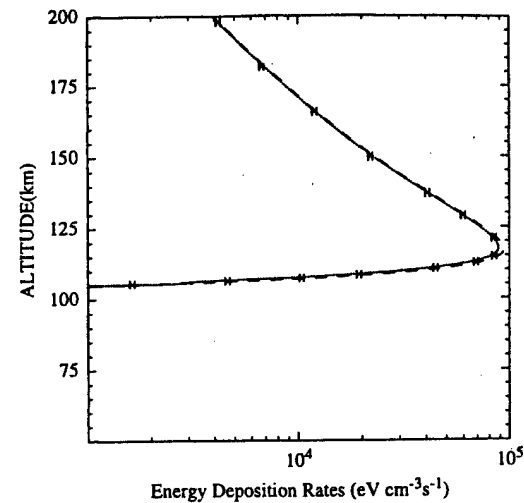


Figure 5b. Same as Figure 5a with expanded scale at lower altitudes.

model results [Decker et al., 1995]. Likewise, measurements of proton fluxes typically involve low count rates and instrumental errors in the 10 to 30% range. Optical measurements of proton auroras typically quote errors larger than 10%. Thus, for the purposes of comparing to observations all three models are effectively identical. Further, the quality of the agreement between models gives us some confidence that there are no major errors in the three computer codes.

The one exception to the otherwise excellent agreement between the models is at the lowest altitudes

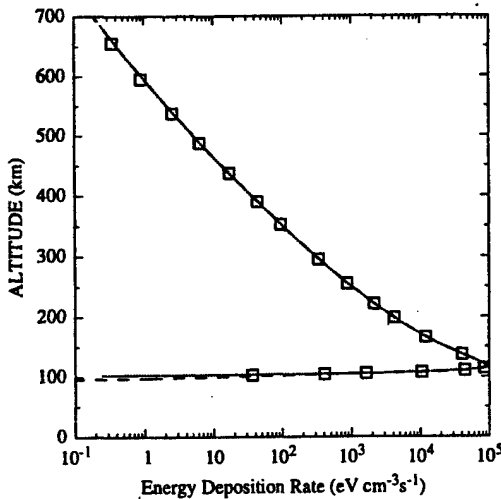


Figure 5a. Energy deposition rate versus altitude. The boxes are the Monte Carlo results, the long dashes are the linear transport results, and the dotted curves are the results from the continuous slowing-down approximation. The incident proton flux is a Maxwellian with a characteristic energy of 8 keV and a total incident energy flux of $0.5 \text{ ergs cm}^{-2}\text{s}^{-1}$.

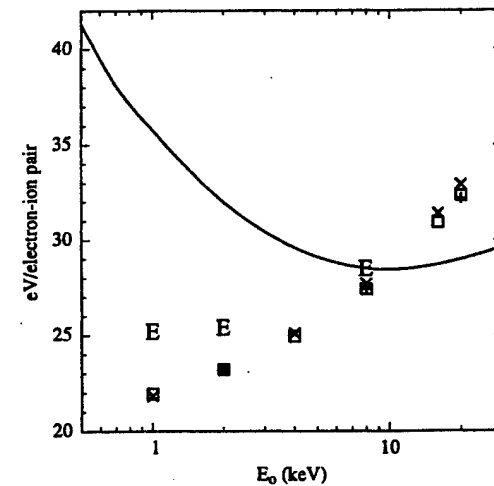


Figure 6. The quantity "eV per electron-ion pair" versus characteristic energy of incident protons given by Maxwellian distributions. The boxes are the Monte Carlo results, the pluses are the linear transport results, the crosses are the results from the continuous slowing down approximation, the "E" labels are results from Monte Carlo calculations that include momentum transfer in elastic collisions and have a minimum energy of 100 eV. The solid curve shows results from Monte Carlo calculations that used the original cross-section set of Kozelov and Ivanov.

(see Figures 1f, 2g, and 3b), where the proton and H atom fluxes are severely attenuated. While the differences between the models are apparent in all the altitude-dependent quantities examined, their fundamental source is the differences between the differential fluxes. In Figures 2a-2g it is evident that the altitudes at which these differences occur depend on the pitch angle of the flux. However, if we consider the fluxes not as a function of altitude but rather as a function of a pitch angle dependent collision or scattering depth such as

$$\tau_P(z, E, \mu) = - \sum_{\alpha} \sigma_{\alpha, P}(E) \int_z^{z_b} \frac{dz'}{\mu} n_{\alpha}(z'), \quad (7)$$

we find that the differences between models occur at around the same collision depth essentially independent of the particular pitch angle. It is the dependence of the collision depth on the cosine of the pitch angle that causes the differences between models to appear at different altitudes for different pitch angles. We thus find that the model differences arising at low altitudes occur at large collision depths where the collisional mean free paths are small compared to the scale heights of the neutral constituents and the altitude step sizes that are typically used in transport calculations. One consequence of this is that the algorithms designed to solve the transport problem often have difficulties at these altitudes and can be very sensitive to the details of their numerical implementation. For the LT model, we have found that it is particularly sensitive to the altitude grid used in this region. In our initial calculations of the energy integrated proton differential flux using a nonuniform grid of 77 altitudes, the LT results near a pitch angle of 180° and at 106 km were over a factor of 2 larger than the MC results. The calculations shown here (Figures 2g and 3b) used 353 altitudes, and the LT results are within 20% of the MC results. The general observed tendency was that when too few grid points were used the LT model penetrated deeper into the atmosphere than did the MC model, and as the grid resolution was improved the LT model approached the MC model. Fortunately, these differences have little effect on such issues as where energy is deposited in the atmosphere or where the bulk of the ionization takes place. Likewise, predictions of the typical observables: particle fluxes, ion densities, ion and neutral temperatures, and optical emissions are little affected by these differences. Thus, for most aeronomical purposes these differences deep in the atmosphere are of no consequence.

It is interesting that when the LT calculations were made with a grid of 77 altitudes, the particle and energy conservation was quite good. Over most altitudes, particle and energy conservation was better than 1%, and at the lowest altitudes both particles and energy were conserved to within a few percent. When the calculations were made with 353 altitudes, the conservation properties were little changed. For example, at some lower altitudes the particle conservation was a little better by a couple of percent and at others a little worse by a couple of percent. However, if we examine

the energy integrated differential flux near a pitch angle of 180°, and at 106 km a modest change in particle conservation is accompanied by over an 80% change in the flux. This can be understood by recalling that what is normally done when testing the particle and energy conservation is to first sum the total number of particles and total energy coming into the system at the top of the atmosphere. One then calculates at each altitude the total number of particles and total energy arriving at that altitude along with what has been lost from the system at all higher altitudes. In this way a check is made whether any particles or energy are lost or created as a result of the numerical methods being used. However, once the lowest altitudes have been reached and the fluxes are orders of magnitude below their original values most of the particles and energy have left the system. The number of particles that are left contribute very little to the total conservation, and thus there can be significant errors in the fluxes yet no strong indication of this in the conservation tests. This implies that checking the overall particle and energy conservation is a necessary but not a sufficient test of the accuracy of a particle transport model. On the other hand, one can test particle and energy conservation at a particular altitude relative to an altitude that is fairly close. In that case, it is possible to get some measure of the quality of the solution even when most of the particles have left the system. For example, if we test particle conservation at a particular altitude relative to the altitude one grid point higher, we find for the LT calculation using 77 altitudes that near a pitch angle 180° between 109 and 104 km the conservation degrades from 1% to 26%. Thus we do have some indication that with this particular altitude grid there are problems with the solution at the very low altitudes.

While the models have been brought into good agreement, we should note that differences can be seen between the models as they are used in different studies. This is perhaps most obvious when Monte Carlo runs are made that include mirroring and beam spreading. Kozelov [1993] has shown that these effects have an impact on the albedo, the charge fractions, and the energy deposition. Clearly, when these effects are important for a particular study, neither the CSDA nor the present LT model will be appropriate, and the MC model is needed. In such a case, if the MC is computationally too intensive for the particular study, one could resort to a table lookup of a set of precalculated MC results. Further differences can arise between the models due to differences in the collisional processes, cross sections, and energy losses that are used. To obtain the level of agreement presented in this paper, we had to take great care in making sure that all these factors were the same in all three models. In particular, we found that the eV/ion pair is very sensitive to any such differences. This is consistent with the discussions by Edgar et al. [1973] and Strickland et al. [1993] where it is pointed out that the shape of the eV/ion pair versus characteristic energy depends on the behavior of the cross sections and energy losses. For example, in Figure

6 we have included some additional calculations of the eV/ion pair. The symbol "E" labels MC calculations that used the cross section set used for this study but also included energy loss due to elastic collisions and extended the minimum energy down to 100 eV. Here we see how including another channel for energy loss (momentum transfer in elastic scattering) leaves less energy available for ionization and hence acts to increase the eV/ion pair. The solid curve gives the results of MC calculations of *Kozelov and Ivanov* [1994] using their standard cross section set. Here the dramatic difference comes in large part from larger low-energy excitation cross sections in the Kozelov and Ivanov cross-section set. Again, the effect is to raise the eV/ion pair at low energies as other collisional processes compete with ionization to degrade the energy of the protons and H atoms. The differences between cross-section sets arise because of the lack of necessary cross-section measurements and thus the need to make estimates and extrapolations in order to assemble a complete set. The focus of this paper has been on comparing three models and not the issue of what cross sections to use nor how well the models compare to observations. However, the success of the comparisons does suggest that our ability to model actual observations is presently limited by uncertainties in cross sections and the lack of suitable observations rather than our ability to solve the equations that describe the known physics of proton/H atom transport.

Appendix

The purpose of this appendix is to derive an implementation of the continuous slowing-down approximation (CSDA) from linear transport theory. We begin with the linear transport equations for protons (P) and hydrogen atoms (H) as given by *Basu et al.* [1990]

$$\begin{aligned} & \left[\mu \frac{\partial}{\partial z} + \sum_{\alpha} n_{\alpha}(z) \sigma_{\alpha,P}(E) \right] \Phi_P(z, E, \mu) \\ &= \sum_{\alpha} n_{\alpha}(z) \int dE' d\mu' \\ & \times \left[\sum_k \sigma_{\alpha,P}^k(E', \mu' \rightarrow E, \mu) \Phi_P(z, E', \mu') \right. \\ & \left. + \sigma_{\alpha}^{01}(E', \mu' \rightarrow E, \mu) \Phi_H(z, E', \mu') \right] \end{aligned} \quad (A1)$$

$$\begin{aligned} & \left[\mu \frac{\partial}{\partial z} + \sum_{\alpha} n_{\alpha}(z) \sigma_{\alpha,H}(E) \right] \Phi_H(z, E, \mu) \\ &= \sum_{\alpha} n_{\alpha}(z) \int dE' d\mu' \\ & \times \left[\sum_k \sigma_{\alpha,H}^k(E', \mu' \rightarrow E, \mu) \Phi_H(z, E', \mu') \right. \\ & \left. + \sigma_{\alpha}^{10}(E', \mu' \rightarrow E, \mu) \Phi_P(z, E', \mu') \right] \end{aligned} \quad (A2)$$

where $\Phi_{\beta}(z, E, \mu)$ is the differential flux of particles (in units of $\text{cm}^{-2}\text{s}^{-1}\text{eV}^{-1}\text{sr}^{-1}$) of type $\beta (= P, H)$ as a function of altitude (z), energy (E), and cosine of the angle between the particle velocity and the z axis (μ); the z axis is antiparallel (parallel) to the geomagnetic field line in the northern (southern) hemisphere; and n_{α} is the concentration of the neutral specie α . The cross sections for the various collisional processes are $\sigma_{\alpha,\beta}^j(E)$ (in units of cm^{-2}), where $j (= k, 10, 01)$ labels the type of collision. The index k refers only to excitation and ionization type collisions and 10 and 01 refer to charge exchange and stripping collisions, respectively. The total cross section summed over types of collisions is given by $\sigma_{\alpha,\beta}(E)$. For the differential cross sections, we make the forward scattering approximation to the angular dependence and assume

$$\begin{aligned} & \sigma_{\alpha,\beta}^j(E', \mu' \rightarrow E, \mu) \\ &= \sigma_{\alpha,\beta}^j(E') \delta(\mu' - \mu) \delta[E' - W_{\alpha,\beta}^j(E') - E] \end{aligned} \quad (A3)$$

where E' is the incident particle energy, E is the final energy, and $W_{\alpha,\beta}^j(E)$ is the energy loss associated with collision type j .

Our first step in developing a CSDA implementation is to break the calculation into two pieces. On the one hand, we calculate the relative charge state composition of the flux by neglecting energy loss and only considering the conversion of protons into H atoms and H atoms back into protons. This is done by setting $W_{\alpha,\beta}^j(E) = 0$ and using (A3) in performing the μ' and E' integrations to obtain

$$\begin{aligned} & \left[\mu \frac{\partial}{\partial z} + \sum_{\alpha} n_{\alpha}(z) \sigma_{\alpha}^{10}(E) \right] \Phi_P(z, E, \mu) \\ &= \sum_{\alpha} n_{\alpha}(z) \sigma_{\alpha}^{01}(E) \Phi_H(z, E, \mu) \end{aligned} \quad (A4)$$

$$\begin{aligned} & \left[\mu \frac{\partial}{\partial z} + \sum_{\alpha} n_{\alpha}(z) \sigma_{\alpha}^{01}(E) \right] \Phi_H(z, E, \mu) \\ &= \sum_{\alpha} n_{\alpha}(z) \sigma_{\alpha}^{10}(E) \Phi_P(z, E, \mu) \end{aligned} \quad (A5)$$

which are (in a slightly different form) (4) and (5) that are used in calculating the charge state composition of the flux. These equations are identical to (17) and (18) in the work of *Basu et al.* [1990] and were originally derived for use at high altitudes. While the particle fluxes that are predicted from these equations are reasonable only for high altitudes, it was found that the calculated flux fractions are accurate at all altitudes.

On the other hand, we also need a method to calculate the effects of energy degradation on the fluxes. This is done by assuming the flux fractions are known and calculating an "average" energy loss for protons and H atoms together. To develop the needed equation, we multiply (A1) and (A2) by E , integrate over μ and E , and add the resulting equations to obtain

$$\begin{aligned} \frac{\partial}{\partial z} \int dE d\mu \mu E \Phi_T(z, E, \mu) \\ = - \sum_{\alpha} n_{\alpha}(z) \int dE d\mu \left[L_{\alpha, P}(E) f_P(z, E, \mu) \right. \\ \left. + L_{\alpha, H}(E) f_H(z, E, \mu) \right] \Phi_T(z, E, \mu) \end{aligned} \quad (\text{A6})$$

where $\Phi_T = \Phi_P + \Phi_H$, $f_{\beta} = \Phi_{\beta}/\Phi_T$, and

$$L_{\alpha, \beta}(E) = \sum_j W_{\alpha, \beta}^j(E) \sigma_{\alpha, \beta}^j(E). \quad (\text{A7})$$

Note that these are the loss functions given in section 2 as (2) and (3). At this point, we make the continuous slowing-down approximation. That is, we assume that the energy of a particle is a continuous function of altitude, $E(z)$. This means that the stochastic nature of the collisional degradation of the protons and H atoms is neglected, and all particles starting with the same energy will lose the same amount of energy as they pass through the same range of altitudes. Thus, if we divide Φ_T into monoenergetic, monodirectional streams at the top of the atmosphere, they will maintain their independent identity as they penetrate down through the atmosphere. Thus the CSDA allows us to write Φ_T in the following form:

$$\Phi_T(z, E, \mu) = \sum_S I_S(z) \delta(E - E_S) \delta(\mu - \mu_S). \quad (\text{A8})$$

For each stream, denoted by S , we can use (A8) in evaluating (A6) giving

$$\begin{aligned} \frac{\partial}{\partial z} \left[\mu_S E_S I_S(z) \right] \\ = - \sum_{\alpha} n_{\alpha}(z) I_S(z) \left[L_{\alpha, P}(E_S) f_P(z, E_S, \mu_S) \right. \\ \left. + L_{\alpha, H}(E_S) f_H(z, E_S, \mu_S) \right] \end{aligned} \quad (\text{A9})$$

We next return to (A1) and (A2), integrate over μ and E , add the resulting equations, and obtain the statement of particle conservation that follows from the transport equations, namely,

$$\frac{\partial}{\partial z} \int dE d\mu \mu \Phi_T(z, E, \mu) = 0. \quad (\text{A10})$$

This gives for each stream,

$$\frac{\partial}{\partial z} \left[\mu_S I_S(z) \right] = 0. \quad (\text{A11})$$

Combining (A9) and (A11) gives

$$\begin{aligned} \frac{dE_S}{dz} = - \frac{1}{\mu_S} \sum_{\alpha} n_{\alpha}(z) \left[L_{\alpha, P}(E_S) f_P(z, E_S, \mu_S) \right. \\ \left. + L_{\alpha, H}(E_S) f_H(z, E_S, \mu_S) \right] \end{aligned} \quad (\text{A12})$$

which in section 2 is given as (1). This then gives us

an ordinary differential equation to solve for the energy (E) as a function of altitude (z).

In the implementation used in this paper, we begin with a flux of downgoing protons at some boundary altitude. As mentioned, the energy and pitch angle distribution of the protons is represented by a set of monoenergetic, monodirectional protons stream. The atmosphere is divided into a series of horizontal layers, and (A4), (A5), and (A12) are applied to each stream. The equations are integrated from altitude to altitude using an explicit Euler method with (A4) and (A5) being solved assuming the energy of the stream is unchanged within a layer and (A12) being solved assuming the flux fractions are unchanged within a layer. At each succeeding altitude, the flux fractions and stream energy are updated for use in integrating down to the next altitude. In this way, the energy degradation and changing composition of each stream are calculated as the protons and H atoms penetrate down from the top of the atmosphere.

Acknowledgments. The work by D.T.D. at Boston College was supported by Air Force contract F19628-93-K-0001. The work by B.B. and J.R.J. at the Phillips Laboratory was supported by the Air Force Office of Scientific Research (AFOSR). The work of B.V.K. and V.E.I. was supported by the Russian Foundation of Fundamental Investigations (RFI).

The Editor thanks R. E. Daniell and J. D. Winningham for their assistance in evaluating this paper.

References

- Basu, B., J.R. Jasperse, R.M. Robinson, R.R. Vondrak, and D.S. Evans, Linear transport theory of auroral proton precipitation. A comparison with observations, *J. Geophys. Res.*, **92**, 5920, 1987.
- Basu, B., J.R. Jasperse, and N.J. Grossbard, A numerical solution of the coupled proton-H atom transport equations for the proton aurora, *J. Geophys. Res.*, **95**, 19069, 1990.
- Basu, B., J.R. Jasperse, D.J. Strickland, and R.E. Daniell Jr., Transport-theoretic model for the electron-proton-hydrogen atom aurora, 1, Theory, *J. Geophys. Res.*, **98**, 21517, 1993.
- Davidson, G.T., Expected spatial distribution of low-energy proton precipitated in the auroral zones, *J. Geophys. Res.*, **70**, 1061, 1965.
- Decker, D. T., B. Basu, J. R. Jasperse, D. J. Strickland, J. R. Sharber, and J. D. Winningham, Upgoing electrons produced in an electron-proton-hydrogen atom aurora, *J. Geophys. Res.*, **100**, 21409, 1995.
- Eather, R.H., Auroral proton precipitation and hydrogen emissions, *Rev. Geophys.*, **5**, 207, 1967.
- Eather, R.H., Ionization produced by auroral proton precipitation, *Ann. Geophys.*, **26**, 609, 1970.
- Eather, R.H., and K.M. Burrows, Excitation and ionization by auroral protons, *Aust. J. Phys.*, **19**, 309, 1966.
- Edgar, B.C., W.T. Miles, and A.E.S. Green, Energy deposition of protons in molecular nitrogen and applications to proton auroral phenomena, *J. Geophys. Res.*, **78**, 6595, 1973.
- Edgar, B.C., H.S. Porter, and A.E.S. Green, Proton energy deposition in molecular and atomic oxygen and applications to the polar cap, *Planet. Space Sci.*, **23**, 787, 1975.

- Galperin, Y.I., Hydrogen emission and two types of auroral spectra, *Planet. Space Sci.*, **1**, 57, 1959.
- Galperin, Y.I., R.A. Kovrashkin, Y.N. Ponomarev, J. Crasnier, and J.A. Sadaud, Pitch angle distributions of auroral protons, *Ann. Geophys.*, **32**, 109, 1976.
- Hardy, D.A., M.S. Gussenhoven, R. Raistrick, and W.J. McNeil, Statistical and functional representations of the pattern of auroral energy flux, number flux, and conductivity, *J. Geophys. Res.*, **92**, 12275, 1987.
- Hardy, D.A., M.S. Gussenhoven and D. Brautigam, A statistical model of auroral ion precipitation, *J. Geophys. Res.*, **94**, 370, 1989.
- Hardy, D.A., W.J. McNeil, M.S. Gussenhoven, and D. Brautigam, A statistical model of auroral ion precipitation, 2, Functional representation of the average patterns, *J. Geophys. Res.*, **96**, 5539, 1991.
- Hedin, A.E., MSIS-86 thermospheric model, *J. Geophys. Res.*, **92**, 4649, 1987.
- Henriksen, K., Variations of proton energy and pitch angle spectra in the upper atmosphere, *J. Atmos. Terr. Phys.*, **41**, 633, 1979.
- Iglesias, G.E., and R.R. Vondrak, Atmospheric spreading of protons in auroral arcs, *J. Geophys. Res.*, **79**, 280, 1974.
- Isaev, S.I., and M.I. Pudovkin, *Aurora and the Processes in the Earth's Magnetosphere*, Nauka, Moscow, 1972.
- Jasperse, J.R., and B. Basu, Transport theoretic solutions for auroral proton and H atom fluxes and related quantities, *J. Geophys. Res.*, **81**, 811, 1982.
- Johnstone, A.D., The spreading of a proton beam by the atmosphere, *Planet. Space Sci.*, **20**, 292, 1972.
- Kozelov, B.V., Influence of the dipolar magnetic field on transport of proton-H atom fluxes in the atmosphere, *Ann. Geophys.*, **11**, 697, 1993.
- Kozelov, B.V., and V.E. Ivanov, Monte Carlo calculation of proton-hydrogen atom transport in N_2 , *Planet. Space Sci.*, **40**, 1503, 1992.
- Kozelov, B.V., and V.E. Ivanov, Effective energy loss per electron-ion pair in proton aurora, *Ann. Geophys.*, **12**, 1071, 1994.
- Ponomarev, Y.N., Intrusion of the monoenergetic monodirectional beams of protons into the polar high atmosphere, (in Russian), *Kosmi. Issled.*, **14**, 144, 1976.
- Porter, H.S., and A.E.S. Green, Comparison of Monte Carlo and continuous slowing-down approximation treatments of 1-keV proton energy deposition on N_2 , *J. Appl. Phys.*, **46**, 5030, 1975.
- Rees, M.H., On the interaction of auroral protons with the Earth's atmosphere, *Planet. Space Sci.*, **30**, 463, 1982.
- Romick, G.J., and C.T. Elvey, Variations in the intensity of the hydrogen emission line H_β during auroral activity, *J. Atmos. Terr. Phys.*, **12**, 283, 1958.
- Sharber, J.R. The continuous (diffuse) aurora and auroral-E ionization, in *Physics of Space Plasmas*, vol. 4, edited by T.S. Chang, B. Coppi and J.R. Jasperse, p. 115, Scientific, Cambridge, Mass., 1981.
- Strickland, D.J., R.E. Daniell Jr., J.R. Jasperse, and B. Basu, Transport-theoretic model for the electron proton-hydrogen atom aurora, 2, Model results, *J. Geophys. Res.*, **98**, 21533, 1993.
-
- B. Basu and J. R. Jasperse, Phillips Laboratory, 29 Randolph Rd., Hanscom Air Force Base, MA 01731-3010. (e-mail: basub@plh.af.mil)
- D. T. Decker, Institute for Scientific Research, Boston College, 885 Centre St., Newton, MA 02159. (e-mail: decker@plh.af.mil)
- V. E. Ivanov and B. V. Kozelov, Polar Geophysical Institute, 184200, Apatity, Murmansk Region, Russia. (e-mail: kozelov@pgi-ksc.murmansk.su)

(Received April 26, 1996; revised August 28, 1996; accepted August 29, 1996.)

Total electron content over the Pan-American Longitudes: March-April 1994

Patricia H. Doherty

Institute for Scientific Research, Boston College, Chestnut Hill, Massachusetts

David N. Anderson

Phillips Laboratory, Hanscom Air Force Base, Massachusetts

John A. Klobuchar¹

Total Electronic Concepts, Lincoln, Massachusetts

Abstract. An experimental campaign to measure diurnal changes in total electron content (TEC) over the wide latitude range from approximately 50°N to 40°S was carried out from March 28 through April 11, 1994, by monitoring the differential carrier phase from the U.S. Navy Navigation Satellite System using a chain of ground stations aligned along the approximate 70°W longitude meridian. This Pan-American campaign was conducted primarily to study the day-to-day variability of the equatorial anomaly region. The experimental plan included using the received values of TEC from the chain of stations to construct profiles of electron density versus latitude using tomographic reconstruction techniques and, then, to compare these reconstructions against a theoretical model of the low-latitude ionosphere. The diurnal changes in TEC along this latitude chain of stations showed a high degree of variability from day to day, especially during a magnetic storm which occurred near the beginning of the campaign. The equatorial anomaly in TEC showed large changes in character in the two hemispheres, as well as differences in magnitude from day to day. The latitudinal gradients of TEC, especially in the lower midlatitudes, also showed large differences between magnetic storm and quiet conditions. Comparisons of the TEC data with the theoretical model illustrate the sensitivity of the model calculations to changes in magnetic $E \times B$ drift and serves to validate the strong influence that these drifts have on the formation and the strength of the equatorial anomaly regions.

Introduction

The equatorial anomaly region is characterized by the highest values of peak electron density and total electron content in the worldwide ionosphere. These large values are primarily due to the daytime upward $E \times B$ drift at the magnetic equator which drives the ionization to higher altitudes. As the layer is lifted to higher altitudes, it diffuses down magnetic field lines that connect to the ionosphere north and south of the equator, causing crests at latitudes approximately +/- 15° from the magnetic equator [Hanson and Moffett, 1966, Anderson, 1973]. This phenomenon has been described as a fountain effect. A discussion on the origin of the terms related to the equatorial fountain effect is presented in the appendix. The day-to-day variability of the equatorial ionosphere can be very large, owing to changes in the strength of the $E \times B$ drift and from differences in the day-to-day strength of both the meridional and zonal component of neutral winds [Sterling *et al.*, 1969].

While many measurements of the equatorial and low-latitude ionosphere have been made by various techniques, beginning with bottomside ionosondes; then, by incoherent scatter radars at Jicamarca, Peru, and at Kwajalein Island; later, by topside sounders; and finally, by a dual-frequency, dispersive radar on the TOPEX/POSEIDON satellite, continuous measurements of the ionosphere over a wide latitude range, in a single longitude sector, have not been generally available. *Deshpande et al.* [1977] first showed the day-to-day variability of the low-latitude total electron content (TEC) and later, *Rastogi and Klobuchar* [1990] showed examples of the day-to-day variability in TEC over the Indian subcontinent. More recently, *Whalen* [1993, 1996] used multiple ionospheric sounders to illustrate the variability in latitudinal profiles of maximum F_2 region electron densities through $+/-30^\circ$ dip latitude. Model studies by *Klobuchar et al.* [1991] showed that different $E \times B$ drifts could significantly change the TEC and the electron density at the F_2 region peak over a wide range of latitudes, but little actual diurnal data over a wide range of latitudes have been available to check the validity of this model. This Pan-American campaign was designed to correct this deficiency.

In order to measure the day-to-day variability of the ionosphere over a wide range of latitudes, a chain of stations was set up along the approximate $70^\circ W$ longitude meridian to make measurements of TEC using the dual-frequency coherent signals from the U.S. Navy Navigation Satellite System (NNSS). Figure 1 illustrates the station chain. The sites were located at Hanscom Air Force Base, Massachusetts, on the islands of Bermuda and Puerto Rico, as well as at Merida, Venezuela; La Paz, Bolivia, and Tucuman, Argentina. The planned site at Tabatinga, Brazil, was not operated owing to logistical difficulties and resulted in a data gap over the geomagnetic equator. Also shown in Figure 1 are typical NNSS satellite passes, both a northbound and a southbound one, to illustrate that the station chain was nearly ideal for such measurements.

Ionospheric Measurements

The NNSS satellites transmit coherent radio beacons at 150 and 400 MHz. The space vehicles are placed in near-circular polar orbits at altitudes of approximately 1100 km [*Newton, 1967*]. *Evans and Holt* [1973] showed that these satellites are ideally suited to studies of latitudinal variations of ionospheric behavior by using NNSS measurements to observe the location of the midlatitude trough from Millstone Hill, Massachusetts. More recently, tomographic reconstruction studies have utilized NNSS satellite

measurements in an effort to construct profiles of electron density versus latitude [Kersley *et al.*, 1993; Pakula *et al.*, 1995]. In this study, there were six NNSS satellites transmitting on the operational navigation frequencies during the approximate 2-week period of the campaign, making it possible to record a high elevation pass from one of the NNSS satellites from the chain of stations approximately every 2 hours. To determine the measurement of TEC along the 70° meridian, the relative differential carrier phase recorded at all sites was combined, converted to equivalent vertical TEC, and changed into absolute TEC values using a visual, multistation version of the two-station method developed by Leitinger *et al.* [1975].

The campaign data are complemented with simultaneous measurements of TEC from dual-frequency Global Positioning System (GPS) and from vertical TEC measured with the TOPEX/POSEIDON satellite. GPS dual-frequency data recorded at Arequipa, Peru; Santiago, Chile, and the island of Bermuda were obtained from the International GPS Service for Geodynamics network that is managed by the Jet Propulsion Laboratory [International Association of Geodesy, 1995]. For this data set, absolute measurements of TEC were made by combining the differential phase and differential group delay measurements. The slant TEC values then were converted to equivalent vertical TEC at 400 km. In addition, coincident measurements from the TOPEX/POSEIDON satellite are also presented in this study. The TOPEX satellite mission is dedicated to the study of ocean topography. The onboard dual-frequency (5.2 and 13.6 GHz) altimeter provides near-global vertical TEC measurements over the ocean areas [Imel, 1994].

The measurements were made near solar minimum in late March and early April 1994. Geomagnetic activity levels were considered quiet in the first few days of the campaign. A major magnetic storm began on April 2, and the remainder of the period of observations had at least moderate geomagnetic activity. Data recorded during the campaign thus allowed the opportunity to study the latitudinal gradients of the ionosphere during both geomagnetically quiet and disturbed conditions. Figure 2 illustrates the planetary 3-hour K_p indices recorded during the campaign period.

Experimental Results

An example of equivalent vertical TEC from the full chain of six stations is shown in Figure 3. In this figure, the TEC is plotted from approximately 50°N to

40°S, a latitude span of 90° encompassing both sides of the equatorial region. At this longitude sector, the magnetic equator is located at approximately 11°S geographic latitude. Figure 3 shows a classic case of two clearly defined anomaly regions spaced approximately 10 to 15° away from the geomagnetic equator in both the northern and southern hemispheres. Note that the two stations from which the southern anomaly peak in equivalent vertical TEC is inferred give somewhat different TEC values, though they both show the peak at the same latitude. This difference in equivalent vertical TEC is due to errors in converting from the measured slant TEC to an equivalent vertical TEC when looking through gradients which are a function of elevation angle. This problem has been discussed by *Tsedilina et al. [1994]*.

To assess the accuracy of the TEC measurements made during the campaign, equivalent vertical TEC from GPS receivers located at Santiago, Chile; Arequipa, Peru, and the island of Bermuda, together with vertical TEC measurements made via the TOPEX/POSEIDON satellite, were compared with campaign data. Figure 4 illustrates two of these comparisons. The GPS measurements shown in this figure represent simultaneous measurements of equivalent vertical TEC at 400 km. Since GPS satellites are located at an altitude greater than 20,000 km and the NNSS satellites are at approximately 1100 km, simultaneous measurements from the two satellite systems are relatively short in local time. The TOPEX measurements in this illustration are restricted to times when the TOPEX ground track comes within 1 hour local time of the campaign measurements. The TOPEX satellite is located at approximately 1300 km and provides vertical measurements of TEC to that height. Figure 4 (left) illustrates close agreement between the NNSS and GPS measurements recorded on day 93 (April 3) at approximately 2320 UT. This plot also shows that the TOPEX and NNSS calculations compare favorably in the shape and geographic location of the southern anomaly peak. The differences occur in the slight shift in the anomaly region surrounding the southern anomaly peak and the magnitude at the peak. The TOPEX calculations illustrate a peak that is approximately 6 TEC units smaller than the NNSS measurements. This difference could represent an error in the slant to vertical conversion process used for the NNSS data. In Figure 4 (right), similar measurements of TEC are observed from all three observation types during an NNSS pass occurring near 1030 UT on day 95 (April 5).

The PANAM campaign provided the unique opportunity to observe the full diurnal development and decay of the equatorial anomaly. Figure 5 illustrates

measurements from a series of satellite passes for 4 consecutive days during the campaign. Note that the approximate local time of each pass is printed inside the left y axis and that each pass is offset by 15 TEC units for each hour of local time after noon to allow a visual separation between passes. In this figure, a classic response to the $E \times B$ drift is portrayed, where the anomaly begins to develop by late morning but does not peak until near 2000 hours local time. Not all six stations were operating for these days, but the general behavior of the equatorial anomaly and the differences in the shape of the anomaly among the 4 days can still be seen in Figure 5. Note that the magnitude, width, and symmetry of the latitudinal anomaly peaks in the southern and northern hemisphere exhibit large variation over this 4-day period. In particular, there is little evidence of the northern anomaly peak on day 94 (April 4) at local noon, while there is clear evidence of it on days 95 through 97. Also, the slope on the northern side of the anomaly peak at local noon differs greatly over the 4 days. Finally, the magnitudes of the southern anomaly peaks are much higher on days 94 and 96 than on days 95 and 97. The postmidnight and early morning passes, although not included in Figure 5, show no signs of anomaly features. They are descriptive of the downward motion of the vertical $E \times B$ drift, where the ionization is driven to lower heights to a region of greater loss. Although this data set is very informative, the data gaps near the magnetic equator seriously limit our ability to make precise determinations of the location and shape of the anomaly, particularly in the northern hemisphere. These data gaps are due to the lack of a station near the magnetic equator, together with intermittent power difficulties experienced at the La Paz, Bolivia, station.

The dramatic day-to-day variability illustrated in the campaign measurements is consistent with earlier research. In particular, Whalen [1993, 1996] reconstructed latitudinal profiles of the maximum F region electron density for 30 consecutive days in September 1958 by combining ionograms from a chain of ionosondes located in the western hemisphere equatorial region. His results illustrate apparent day-to-day differences in the symmetry and magnitude of the equatorial anomaly peaks. He also found asymmetry in the time of the enhancements, where the anomaly peak occurred earlier in the north than in the south for most days in the observation period.

The high degree of variation in the development of the equatorial anomaly illustrated in Figure 5 is primarily due to the large differences in the vertical electrodynamic lift at the equator. Drift variations have been shown to have a large impact on the latitudinal location and amplitude of the equatorial anomaly peaks

[Klobuchar *et al.*, 1991]. The symmetry of both the amplitude and position of the equatorial anomaly peaks between the northern and southern hemisphere is largely a neutral wind effect. The next section focuses on some of these relationships by comparing campaign data to a theoretical model of the low-latitude ionosphere.

Model Comparisons

The data recorded during the campaign provides a unique database for model validation. In this section, a comparison of TEC measurements with calculations from the Phillips Laboratory Global Theoretical Ionospheric Model (GTIM) [Anderson *et al.*, 1996], is presented. The *F* region portion of this model numerically solves the O^+ continuity equation to determine O^+ densities as a function of altitude, latitude, longitude, and local time. The model requires a variety of geophysical inputs that include a neutral atmosphere, neutral winds, ion and electron temperatures, and $E \times B$ drift velocities. The standard model inputs and calculations used in the low-latitude model are described by Preble *et al.* [1994] and Anderson *et al.* [1996]. The GTIM model is flexible in that the inputs can be modified to test the sensitivity of the ionosphere to any one or more of these parameters.

Figures 6a through 6d illustrate a comparison of the data with a sequence of model calculations. Figure 6a shows the equivalent vertical TEC measurements recorded on April 6. For clarity, the approximate local time is printed near the left y axis and each curve is offset by a factor of 40 TEC units. These data show a well-defined equatorial anomaly at local noon. It peaks near 1900 local time and begins to show signs of decay at 2300 hours. Figures 6b-6d represent model calculations for comparable geomagnetic, seasonal, and solar conditions. The results shown in Figure 6b are based on a climatological vertical $E \times B$ drift pattern for solar moderate conditions [Fejer, 1981]. Note that the local time development and the dip latitude positions of the peaks are realistic, while the magnitudes of the peaks are much smaller than those exhibited in the data measurements. Initial efforts to increase the magnitude of the equatorial anomaly peaks were made by increasing the $E \times B$ drift. The results of those efforts (not shown) illustrate larger peaks but with the anomaly pushed out to higher latitudes. The base run of the model shown in Figure 6b used a temperature model that was originally developed for the midlatitude region [Strobel and McElroy, 1970]. Figure 6c represents the model calculations that include a more appropriate low-latitude temperature model [Brace and Theis, 1981]. This modification produces sharper

anomaly peaks and more realistic slopes poleward of the anomaly peaks. The dip latitude positions of the anomaly peaks are accurately maintained, but the magnitude of the peaks are still much smaller than the data calculations. The $E \times B$ vertical drift velocities used in the model are based on drift measurements made at Jicamarca, Peru. In general, they are applied in the GTIM model with no altitude dependence. Work by *Pingree and Fejer [1987]* and *Su et al. [1995]* indicate that the altitude variations of the vertical drift velocities are important in the development of the equatorial anomaly. Figure 6d illustrates model results when a simple linear height variation in the vertical drift is incorporated into the calculations. This modification produces more accurate peak shapes in both hemispheres and realistic slopes to higher latitudes within $\pm 20^\circ$ dip latitude. The unrealistic change induced at latitudes greater than $\pm 20^\circ$ indicates that the drift gradient needs to be refined. Although the magnitudes of the anomaly peaks have been increased, they are still lower than the data measurements. To provide a more quantitative measure of the differences shown in Figure 6, plots of data versus model calculations at 1200, 1900, and 2300 hours local time are provided in Figure 7. In this figure, it is evident that the model calculations that include the linear height variation in the drift velocities best replicate the features shown in the data. This is most apparent at 1900 hours in the northern hemisphere and in the shape of anomaly in the modeled results at 1200 and 2300 hours.

The comparisons illustrated in Figures 6 and 7 illustrate the sensitivity of the equatorial anomaly to ion and electron temperatures and $E \times B$ drift velocities. Although the data clearly show asymmetries that are likely due to the neutral winds, it is beyond the scope of this paper to replicate this asymmetry with the model. Future modeling studies will include efforts to investigate neutral wind effects and to refine the $E \times B$ drift gradient applied in the model. In this study, GTIM has shown the capability to reproduce some of the major features of measured data in the low-latitude region, even under geomagnetically disturbed conditions.

Conclusions

The first attempt at measuring the day-to-day variability of TEC over a large geographic latitude range has been successful. The database collected illustrates the large day-to-day variability in the occurrence, location, and amplitude of the equatorial anomaly. A surprising feature uncovered by this study is that the TEC values are so low in the latitude range

greater than +/-40° and that the latitudinal gradients in TEC are steeper on the poleward edge of the southern anomaly peak than on the poleward edge of the northern anomaly peak. The multistation data measurement technique has been validated by simultaneous measurements of TEC from dual-frequency GPS and dual-frequency altimeter measurements from the TOPEX/POSEIDON satellite.

Model comparisons with observations have illustrated, for the first time, the sensitivity of the equatorial anomaly to changes in ion and electron temperatures and to vertical $E \times B$ drift velocities. In particular, the results show that the altitude variations of vertical drift velocities have a significant impact on the development of the equatorial anomaly. Additional modeling work is required to further test variations in drift gradients and to investigate neutral wind effects to determine how closely the model can fit the experimental data over a wide latitude range.

One of the prime purposes of the campaign was to develop an equatorial database to be used in ionospheric tomography reconstructions. The study demonstrates that the absence of a station near the geomagnetic equator significantly hampers the reconstruction of the equatorial ionosphere. Future tomographic campaign organizers, take note!

Appendix: Origin of the Term “equatorial fountain”

Many authors, including *Balan and Bailey* [1996], have shown that the equatorial fountain greatly increases both peak electron density and TEC throughout the low-latitude ionosphere; but who originated this very apt expression for the source of the largest ionization in the world? The term “fountain effect” was quoted by *Hanson and Moffett* [1966, p.5560], as “*Martyn* (1955) envisages a ‘fountain effect’ in which the ionization is lifted upward at low latitudes and then deposited at higher latitudes by diffusion along the field lines.” However, the term “fountain effect” is not found in the work by *Martyn* [1955].

Rush and Richmond [1973, p.1171] stated “*Duncan* (1960) has termed this the ‘fountain theory.’” However, the term “fountain theory” is not found in the work by *Duncan* [1960]. After an extensive search, it was discovered that *Wright* [1962] was the person who coined this term. *Wright* [1962, p.7], in his discussion of the mechanism producing the equatorial anomaly in *F* region ionization, stated “We propose the term ‘Equatorial Fountain’ as a concise term for these processes.” Thus the historical record is now set straight.

Acknowledgments. The authors would like to thank the many members of the Ionospheric Effects Division at Phillips Laboratory who participated in the campaign. Air Force Captain William A. Pakula deserves particular mention for his outstanding role as Operations Manager for the campaign. Additional appreciation is extended to Dwight T. Decker of Boston College for many useful discussions on ionospheric modeling and to Virginia Ewell and Jane Vladimer of the Electrical, Computer, and Systems Engineering Department at Boston University for their assistance in processing the TOPEX measurements used for PANAM data validation. Finally, we would like to thank Jay Spaulding at the U.S. Coast Guard Research and Development Center in Groton, Connecticut, for the loan of the GPS Ashtech receiver that was used in Merida, Venezuela.

References

- Anderson, D. N., A theoretical study of the ionospheric *F*-region equatorial anomaly, I, Theory, *Planet. Space Sci.*, 21, 409-419, 1973.
- Anderson, D. N., D. T. Decker, and C. E. Valladares, Global Theoretical Ionospheric Model (GTIM), in *STEP Hand Book*, edited by R. W. Schunk, pp. 133-152, Utah State Univ., Logan, 1996.
- Balan, N., and G. J. Bailey, Modeling studies of the equatorial plasma fountain and equatorial anomaly, *Adv. Space Res.*, 18(3), 107-116, 1996.
- Brace, L. H., and R. F. Theis, Global empirical models of ionospheric electron temperatures in the upper *F*-region and plasmasphere based on *in situ* measurements for the Atmospheric Explorer-C, ISIS-1 and ISIS-2 satellites, *J. Atmos. Terr. Phys.*, 43, 1317-1343, 1981.
- Deshpande, M. R., R. G. Rastogi, H. O. Vats, J. A. Klobuchar, and G. Sethia, Effect of the electrojet on the total electron content over the Indian subcontinent, *Nature*, 267, 599-600, 1977.
- Duncan, R. A., The equatorial *F*-region of the ionosphere, *J. Atmos. Terr. Phys.*, 18, 89-100, 1960.
- Evans, J. V., and J. M. Holt, The combined use of satellite differential doppler and ground-based measurements for ionospheric studies, *IEEE Trans. Antennas Propag.*, AP-21, 685-692, 1973.
- Fejer, B. G., The equatorial ionospheric electric fields, a review, *J. Atmos. Terr. Phys.*, 43, 377-386, 1981.
- Hanson, W. B., and R. J. Moffett, Ionization transport effects in the equatorial *F* region, *J. Geophys. Res.*, 71 (23), 5559-5572, 1966.
- International Association of Geodesy, *International GPS Service for Geodynamics*, Cent. Bur., Jet Propul. Lab., Pasadena, Calif., 1995.
- Imel, D. A., Evaluation of the TOPEX/POSEIDON dual-frequency ionosphere correction, *J. Geophys. Res.*, 99 (C12), 24,895-24,906, 1994.
- Kersley, L., J. A. T. Heaton, S. E. Pryse, and T. D. Raymund, Experimental ionospheric tomography with ionosonde input and EISCAT verification, *Ann. Geophys.*, 11, 1064-1074, 1993.
- Klobuchar, J. A., D. N. Anderson, and P. H. Doherty, Model studies of the latitudinal extent of the equatorial anomaly

- during equinoctial conditions, *Radio Sci.*, 26 (4), 1025-1047, 1991.
- Leitinger, R., G. Schmidt, and A. Tauriainen, An evaluation method combining the differential doppler measurements from two stations that enables the calculation of the electron content of the ionosphere, *J. Geophys.*, 41, 201-213, 1975.
- Martyn, D. F., Theory of height and ionization density changes at the maximum of a chapman-like region, taking account of ion production, decay, diffusion, and tidal drift, in *Proceedings of Cambridge Conference*, pp. 254-259, Phys. Soc., London, 1955.
- Newton, R. R., The Navy Navigation Satellite System, *Space Res.*, 7, 735-763, 1967.
- Pakula, W. A., P. F. Fougere, J. A. Klobuchar, H. J. Kuenzler, M. J. Buonsanto, J. M. Roth, J. C. Foster, and R. E. Sheehan, Tomographic reconstruction of the ionosphere over North America with comparisons to ground-based radar, *Radio Sci.*, 30 (1), 89-103, 1995.
- Pingree, J. E., and B. G. Fejer, On the height variation of the equatorial F-region vertical plasma drifts, *J. Geophys. Res.*, 92 (A5), 4763-4766, 1987.
- Preble, A. J., D. N. Anderson, B. G. Fejer, and P. H. Doherty, Comparison between calculated and observed F-region electron density profiles at Jicamarca, Peru, *Radio Sci.*, 29 (4), 857-866, 1994.
- Rastogi, R. G., and J. A. Klobuchar, Ionospheric electron content within the equatorial F_2 layer anomaly belt, *J. Geophys. Res.*, 95 (A11), 19,045-19,052, 1990.
- Rush, C. M., and A. D. Richmond, The relationship between the structure of the equatorial anomaly and the strength of the equatorial electrojet, *J. Atmos. Terr. Phys.*, 35, 1171-1180, 1973.
- Sterling, D. L., W. B. Hanson, R. J. Moffett, and R. G. Baxter, Influence of electrodynamic drifts and neutral air winds on some features of the F_2 region, *Radio Sci.*, 4, 1005-1023, 1969.
- Strobel, D. F., and M. B. McElroy, The F_2 -layer at mid-latitudes, *Planet. Space Sci.*, 18, 1181-1202, 1970.
- Su, Y. Z., K. I. Oyama, G. J. Bailey, T. Takahashi, and S. Watanabe, Comparison of satellite electron density and temperature measurements at low latitudes with a plasmasphere-ionosphere model, *J. Geophys. Res.*, 100 (A8), 14,591-14,604, 1995.
- Tsedilina, E. E., O. V. Weitsman, and H. Soicher, Time delay of transitionospheric radio signals in a horizontally inhomogeneous ionosphere, *Radio Sci.*, 29 (3), 625-630, 1994.
- Whalen, J. A., The equatorial F layer: +/- 30° DIPLAT profiles for a continuous 30 day period (abstract), *Eos Trans AGU*, 74 (43), Fall Meet. Suppl., 457, 1993.
- Whalen J. A., Mapping a bubble at dip equator and anomaly with oblique ionospheric soundings of range spread F", *J. Geophys. Res.*, 101 (A3), 5185-5193, 1993.
- Wright, J. W., Vertical cross sections of the ionosphere across the geomagnetic equator, *NBS Tech. Note* 138, U.S. Dept. of Commer., Washington, D. C., 1962.

D. N. Anderson, Phillips Laboratory/GPSM, 29 Randolph Road, Hanscom Air Force Base, MA 01731. (e-mail: danderson@plh.af.mil)

P. H. Doherty, Institute for Scientific Research, Boston College, St. Clement's Hall, Room 402, 140 Commonwealth Avenue, Chestnut Hill, MA 02167. (e-mail: doherty@plh.af.mil)

John A. Klobuchar, Total Electronic Concepts, 27 Conant Road, Lincoln, MA 01773. (e-mail: tecgps@aol.com)

(Received October 10, 1996; revised March 3, 1997; accepted March 19, 1997.)

¹Formerly at Phillips Laboratory, Hanscom Air Force Base, MA 01731.

Copyright 1997 by the American Geophysical Union.

Paper Number 97RS00840.
0048-6604/97/97RS-00840\$11.00

DOHERTY ET AL.: TOTAL ELECTRON CONTENT OVER AMERICAN SECTOR
 DOHERTY ET AL.: TOTAL ELECTRON CONTENT OVER AMERICAN SECTOR
 DOHERTY ET AL.: TOTAL ELECTRON CONTENT OVER AMERICAN SECTOR
 DOHERTY ET AL.: TOTAL ELECTRON CONTENT OVER AMERICAN SECTOR
 DOHERTY ET AL.: TOTAL ELECTRON CONTENT OVER AMERICAN SECTOR
 DOHERTY ET AL.: TOTAL ELECTRON CONTENT OVER AMERICAN SECTOR
 DOHERTY ET AL.: TOTAL ELECTRON CONTENT OVER AMERICAN SECTOR
 DOHERTY ET AL.: TOTAL ELECTRON CONTENT OVER AMERICAN SECTOR
 DOHERTY ET AL.: TOTAL ELECTRON CONTENT OVER AMERICAN SECTOR
 DOHERTY ET AL.: TOTAL ELECTRON CONTENT OVER AMERICAN SECTOR
 DOHERTY ET AL.: TOTAL ELECTRON CONTENT OVER AMERICAN SECTOR
 DOHERTY ET AL.: TOTAL ELECTRON CONTENT OVER AMERICAN SECTOR
 DOHERTY ET AL.: TOTAL ELECTRON CONTENT OVER AMERICAN SECTOR
 DOHERTY ET AL.: TOTAL ELECTRON CONTENT OVER AMERICAN SECTOR
 DOHERTY ET AL.: TOTAL ELECTRON CONTENT OVER AMERICAN SECTOR
 DOHERTY ET AL.: TOTAL ELECTRON CONTENT OVER AMERICAN SECTOR
 DOHERTY ET AL.: TOTAL ELECTRON CONTENT OVER AMERICAN SECTOR
 DOHERTY ET AL.: TOTAL ELECTRON CONTENT OVER AMERICAN SECTOR
 DOHERTY ET AL.: TOTAL ELECTRON CONTENT OVER AMERICAN SECTOR
 DOHERTY ET AL.: TOTAL ELECTRON CONTENT OVER AMERICAN SECTOR
 DOHERTY ET AL.: TOTAL ELECTRON CONTENT OVER AMERICAN SECTOR
 DOHERTY ET AL.: TOTAL ELECTRON CONTENT OVER AMERICAN SECTOR
 DOHERTY ET AL.: TOTAL ELECTRON CONTENT OVER AMERICAN SECTOR

Figure 1. Map of stations along the $\sim 70^\circ$ W longitude meridian used in the campaign.

Figure 2. Planetary 3-hour K_p indices recorded during the campaign period.

Figure 3. Equivalent vertical total electron content (TEC) from the full chain of six stations at approximately 1600 UT on April 6, 1994.

Figure 4. Comparison of TEC measurements from the U.S. Navy Navigation Satellite System (NNSS), TOPEX, and Global Positioning System (GPS) satellite systems at approximately 2320 hours UT on April 3, 1994 (left) and on April 5 at approximately 1030UT (right).

Figure 5. Diurnal development of the equatorial anomaly from 1200 to 2400 hours local time for April 4-7, 1994.

Figure 6. (a) Equivalent vertical TEC measurements of April 6, 1994. (b) Model calculations based on climatological $E \times B$ drift and original temperature model (see text). (c) Model calculations with a more appropriate low-latitude temperature model. (d) Model calculations with a more appropriate low-latitude temperature model and an $E \times B$ drift height gradient.

Figure 7. Comparison of data versus model calculations at 1200, 1900, and 2300 hours local time.

Figure 1. Map of stations along the $\approx 70^\circ$ W longitude meridian used in the campaign.

Figure 2. Planetary 3-hour K_p indices recorded during the campaign period.

Figure 3. Equivalent vertical total electron content (TEC) from the full chain of six stations at approximately 1600 UT on April 6, 1994.

Figure 4. Comparison of TEC measurements from the U.S. Navy Navigation Satellite System (NNSS), TOPEX, and Global Positioning System (GPS) satellite systems at approximately 2320 hours UT on April 3, 1994 (left) and on April 5 at approximately 1030UT (right).

Figure 5. Diurnal development of the equatorial anomaly from 1200 to 2400 hours local time for April 4-7, 1994.

Figure 6. (a) Equivalent vertical TEC measurements of April 6, 1994. (b) Model calculations based on climatological $E \times B$ drift and original temperature model (see text). (c) Model calculations with a more appropriate low-latitude temperature model. (d) Model calculations with a more appropriate low-latitude temperature model and an $E \times B$ drift height gradient.

Figure 7. Comparison of data versus model calculations at 1200, 1900, and 2300 hours local time.

Figure 1. Map of stations along the $\approx 70^\circ$ W longitude meridian used in the campaign.

Figure 2. Planetary 3-hour K_p indices recorded during the campaign period.

Figure 3. Equivalent vertical total electron content (TEC) from the full chain of six stations at approximately 1600 UT on April 6, 1994.

Figure 4. Comparison of TEC measurements from the U.S. Navy Navigation Satellite System (NNSS), TOPEX, and Global Positioning System (GPS) satellite systems at approximately 2320 hours UT on April 3, 1994 (left) and on April 5 at approximately 1030UT (right).

Figure 5. Diurnal development of the equatorial anomaly from 1200 to 2400 hours local time for April 4-7, 1994.

Figure 6. (a) Equivalent vertical TEC measurements of April 6, 1994. (b) Model calculations based on climatological $E \times B$ drift and original temperature model (see text). (c) Model calculations with a more appropriate low-latitude temperature model. (d) Model calculations with a more appropriate low-latitude temperature model and an $E \times B$ drift height gradient.

Figure 7. Comparison of data versus model calculations at 1200, 1900, and 2300 hours local time.

